

# Hybrid solutions for cutter suction dredgers

A feasibility study on the application of electrical  
energy storage

M.J.W. van Leeuwen

**Delft University of Technology**

Faculty of Mechanical, Maritime and Materials Engineering  
Master of Science Thesis

Report number SDPO.17.012.m





# Hybrid solutions for cutter suction dredgers

A feasibility study on the application of electrical  
energy storage

by

M.J.W. van Leeuwen

to obtain the degree of Master of Science  
at the Delft University of Technology,  
to be defended publicly on Thursday June 29, 2017 at 13:30.

Report number:	SDPO.17.012.m	
Student number:	1394347	
Project duration:	October 1, 2016 – July 1, 2017	
Thesis committee:	Ir. K. Visser, Rear-Admiral (ME) ret., Ir. P. de Vos, Dr.ir. P.R. Wellens, Ir. P.G.E. Vos, Ir. B.T.W. Mestemaker,	TU Delft TU Delft, supervisor TU Delft Royal IHC, supervisor Royal IHC

An electronic version of this thesis is available at <http://repository.tudelft.nl/>.

(This page is intentionally left blank)

# Abstract

Cutter suction dredgers are a type of hydraulic dredgers often used in areas with hard soil where other types of dredging vessels would be ineffective. As a result of the wide range of type of soil that is being cut a lot of variation is seen in the power demand on the cutter suction dredger's diesel-electric power generation system. Consequently, the load on the main diesel engines rapidly changes. To smoothen power demand the addition of an energy storage system to the power generation system is investigated to reduce the load variation experienced by the main engines. Reduction of the load variation is also relevant for the application of dual fuel engines in cutter suction dredgers. For dual fuel engines exceeding of the loading limit poses a significant risk of the main engines switching from combustion of (liquefied) natural gas to combustion of diesel fuel to prevent misfiring or engine knocking. Better control of the engine load is expected to allow continuous combustion of liquefied natural gas during dredging operation.

From the analysis of the power demand measured during dredging operation it is concluded that energy storage systems capable of delivering high power and have relatively low energy storage capability are best suited for this application. Based on the required characteristics flywheel energy storage and supercapacitor energy storage are selected as suitable energy storage systems. For both energy storage systems a simulation model is created based on available literature.

A benchmark simulation model of the driveline of a cutter suction dredger, including the power generation system and electrical network, is created and validated using measurement data. The power and energy storage capacity of the energy storage system are determined by exceeding of the loading capacity of the main engines defined by the engine manufacturer during several months of continuous dredging operation. Separate cases are investigated where a supercapacitor energy storage system and a flywheel energy storage system are added. Simulation results are compared to the results of the benchmark model. Furthermore, simulations are conducted where the main diesel engines are replaced by dual fuel engines running on liquefied natural gas with a methane number of 80.

Results show that both energy storage systems are capable of increasing the percentage of load variation within the engine limit on the original driveline from 91% to at least 99%. For dual fuel engines it is found that without an energy storage system 75% of the load variation is within the engine's loading limit, meaning switching to diesel fuel is inevitable during dredging operation. The addition of an energy storage system increases the percentage of load variation within the engine's loading limit to at least 98%. While the engine limit is still rarely exceeded, further analysis showed that the air excess ratio stays between the knock limit and misfire limit, meaning no switching to diesel fuel is required. As a result, continuous dredging operation using LNG as fuel is possible resulting in a reduction in fuel cost up to roughly 30%.

During this research it is found that the effect of transient loads on engine wear could not be quantified. Further research into this subject is needed before conclusions can be made with regard to this subject. Also, no reduction in fuel consumption is seen as a result of the reduction of transient loading.

# Contents

<b>Preface</b>	<b>XIII</b>
<b>1 Introduction</b>	<b>1</b>
1.1 General background . . . . .	1
1.2 Problem definition . . . . .	2
1.3 Research objective . . . . .	3
1.4 Thesis outline . . . . .	3
<b>2 Cutter suction dredger</b>	<b>5</b>
2.1 General description . . . . .	5
2.2 Dredging operation . . . . .	6
2.3 Driveline configuration . . . . .	7
2.4 Driveline components . . . . .	8
2.4.1 Electric motors . . . . .	9
2.4.2 Generators . . . . .	10
2.4.3 Diesel engines . . . . .	10
2.4.4 Cutter . . . . .	11
2.5 Typical cutter load . . . . .	11
<b>3 Hybrid systems and alternate configurations</b>	<b>12</b>
3.1 Definitions . . . . .	12
3.2 Applications . . . . .	13
3.2.1 Peak shaving . . . . .	13
3.2.2 Spinning reserve . . . . .	13
3.3 Energy storage configuration . . . . .	14
3.4 Dual fuel engines . . . . .	14
3.4.1 Transient response behavior . . . . .	14
3.4.2 Loading capability . . . . .	15
3.4.3 Loading limit . . . . .	16
3.4.4 Gas fuel quality . . . . .	17
3.5 Alternate engine configuration . . . . .	17
<b>4 Energy storage systems</b>	<b>19</b>
4.1 Energy storage sizing . . . . .	19
4.1.1 Load analysis . . . . .	20
4.1.2 Air excess ratio . . . . .	20
4.1.3 Power requirements . . . . .	24
4.1.4 Energy requirements . . . . .	25
4.2 Energy storage system selection . . . . .	26
4.3 Supercapacitors . . . . .	27
4.3.1 Power and energy . . . . .	28
4.3.2 Losses and constraints . . . . .	29
4.4 Flywheel energy storage . . . . .	30
4.4.1 Power and energy . . . . .	30
4.4.2 Losses and constraints . . . . .	31

4.5	Cycle life . . . . .	31
4.6	Power management . . . . .	32
4.7	Performance evaluation criteria . . . . .	33
4.7.1	Transient loads . . . . .	33
4.7.2	Fuel consumption . . . . .	34
4.7.3	ESS cycle life . . . . .	34
4.7.4	Cost analysis . . . . .	34
4.7.5	Size and weight . . . . .	35
4.7.6	Fuel specifications . . . . .	35
4.7.7	Network voltage and frequency . . . . .	36
<b>5</b>	<b>Modeling</b>	<b>37</b>
5.1	Modeling principles . . . . .	37
5.1.1	Per unit representation . . . . .	37
5.1.2	DQ-reference frame . . . . .	38
5.2	Energy storage system models . . . . .	38
5.2.1	Supercapacitor model . . . . .	38
5.2.2	Flywheel model . . . . .	42
5.2.3	Network connection . . . . .	46
5.2.4	Power management . . . . .	47
5.3	Driveline component models . . . . .	47
5.3.1	Main diesel engines . . . . .	47
5.3.2	Dual fuel engines . . . . .	48
5.3.3	Induction motors . . . . .	50
5.3.4	Frequency drives . . . . .	55
5.3.5	Synchronous generators . . . . .	56
5.3.6	Other electric components . . . . .	63
5.4	AC network . . . . .	63
5.4.1	Network interface . . . . .	65
5.5	Cutter head . . . . .	66
5.6	Benchmark model . . . . .	67
5.6.1	Model verification . . . . .	69
<b>6</b>	<b>Simulations</b>	<b>72</b>
6.1	Simulation 1 - Diesel engines . . . . .	72
6.1.1	Load . . . . .	72
6.1.2	Maximum load increase . . . . .	73
6.1.3	Power and energy requirements . . . . .	73
6.1.4	ESS size and weight . . . . .	73
6.1.5	Results . . . . .	73
6.2	Simulation 2 - Dual fuel engines . . . . .	80
6.2.1	Load . . . . .	80
6.2.2	Maximum load increase . . . . .	80
6.2.3	Power and energy requirements . . . . .	80
6.2.4	ESS size and weight . . . . .	80
6.2.5	Results . . . . .	80
<b>7</b>	<b>Conclusions and recommendations</b>	<b>86</b>
7.1	Conclusions . . . . .	86
7.1.1	Diesel engines . . . . .	86
7.1.2	Dual fuel engines . . . . .	87
7.1.3	Final conclusion . . . . .	89
7.2	Discussion and Recommendations . . . . .	89
7.2.1	Discussion . . . . .	89
7.2.2	Recommendations . . . . .	90
	<b>Bibliography</b>	<b>92</b>

---

<b>A</b>	<b>Direct-quadrature-zero (<math>dq0</math>) transformation</b>	<b>96</b>
<b>B</b>	<b>Kron reduction</b>	<b>99</b>
<b>C</b>	<b>Energy storage sizing Matlab script</b>	<b>101</b>
<b>D</b>	<b>Simulink models</b>	<b>104</b>
D.1	Power threshold model . . . . .	104
D.2	Supercapacitor model . . . . .	105
D.2.1	Power management and voltage drop . . . . .	107
D.3	Flywheel model . . . . .	109
D.3.1	Power management . . . . .	110
<b>E</b>	<b>Cutter inertia calculation</b>	<b>112</b>
<b>F</b>	<b>Simulation results</b>	<b>114</b>
F.1	Simulation 1-2 . . . . .	115
F.1.1	Load input . . . . .	115
F.1.2	Results . . . . .	115
F.2	Simulation 3-4 . . . . .	116
F.2.1	Load input . . . . .	116
F.2.2	Results . . . . .	116
F.3	Simulation 5-6 . . . . .	117
F.3.1	Load input . . . . .	117
F.3.2	Results . . . . .	117
F.4	Simulation 7-8 . . . . .	118
F.4.1	Load input . . . . .	118
F.4.2	Results . . . . .	118
F.5	Simulation 9-10 . . . . .	119
F.5.1	Load input . . . . .	119
F.5.2	Results . . . . .	119
F.6	Data overview . . . . .	120

# List of Figures

1.1	Typical power demand on the power generation system during cutter suction dredger operation	2
2.1	Side view (top picture) and top view (bottom picture) of a CSD[60]	5
2.2	Cutter ladder and major components.[3] 1.) Electric motors 2.) Gearbox 3.) Thrust bearing 4.) Cutter shaft 5.) Radial bearings 6.) Lifting wire hinges 7.) Cutter head 8.) Main hinge	6
2.3	CSD dredging operation [60]	6
2.4	Cutter suction dredger energy flow diagram[33]	7
2.5	Cutter suction dredger single line diagram	8
2.6	Example of power demand and variation during dredging operation	11
3.1	Peak shaving	13
3.2	Cutter suction dredger energy flow diagram including energy storage system	14
3.3	Injecting additional fuel at constant air flow at low loads[27]	15
3.4	Injecting additional fuel at constant air flow at high loads[27]	15
3.5	Left: Maximum loading capability in gas mode. Right: Normal loading capability in gas mode[63]	16
3.6	Cumulative distribution function of load variation	16
3.7	Output limitations due to methane number and charge air receiver temperature[63]	17
3.8	75% - 95% MCR with two engines	18
3.9	75% - 95% MCR with four engines	18
4.1	Total power demand during twenty-four hours of dredging operation	19
4.2	Power demand of the different components in the CSD driveline during nine days of dredging operation	20
4.3	Load fluctuation of the different components in the CSD driveline over time	20
4.4	Knock and misfire range	21
4.5	Diesel engine maximum ramp-up[38]	22
4.6	Maximum ramp-down[38]	22
4.7	Load variation of power shown in Figure 4.1	22
4.8	Cumulative distribution of load variation	23
4.9	Allowed load steps in diesel mode and gas mode[63]	24
4.10	Simulation of $P_{ESS}$ at an arbitrary maximum diesel engine ramp-up	25
4.11	Simulation of $P_{ESS}$ with an added arbitrary maximum diesel engine ramp-down	26
4.12	Ragone plot[7]	27
4.13	Ragone plot with loading limits	27
4.14	Schematic of a conventional capacitor[21]	28
4.15	Supercapacitor ESS configuration	28
4.16	Supercapacitor voltage at constant current (dis)charging[40]	29
4.17	Supercapacitor efficiencies	29
4.18	Schematic of flywheel components[4]	30
4.19	Flywheel ESS configuration	31
4.20	Flywheel efficiencies	31
4.21	Series of events after a step load increase of a turbocharged diesel engine[48]	33
4.22	Major cost components in an energy storage system[53]	34

5.1	R-C equivalent circuit of a supercapacitor. . . . .	39
5.2	Supercapacitor voltage drop. . . . .	39
5.3	Supercapacitor state-of-charge of a full charge/discharge cycle . . . . .	41
5.4	Supercapacitor charge/discharge power at constant current . . . . .	41
5.5	Supercapacitor voltage when (dis)charging at constant current . . . . .	42
5.6	Flywheel self-discharge as a function of state-of-charge . . . . .	44
5.7	Flywheel state-of-charge of a full charge/discharge cycle . . . . .	45
5.8	Flywheel discharging and charging at constant power . . . . .	45
5.9	Flywheel self-discharge over time . . . . .	45
5.10	Specific fuel consumption at 500 rpm as function of engine load . . . . .	48
5.11	Specific fuel consumption at 750 rpm as function of engine load . . . . .	49
5.12	Specific pilot fuel consumption at 750 rpm as function of engine load . . . . .	49
5.13	Normalized SFC of the diesel and dual fuel engines . . . . .	50
5.14	Induction motor equivalent circuit[35] . . . . .	52
5.15	Measured torque-slip characteristic . . . . .	54
5.16	Simulated torque-slip characteristic . . . . .	54
5.17	Current at $M_{nom}$ and $\frac{1}{2}M_{nom}$ . . . . .	54
5.18	Modeled frequency drive interconnection with motor and network[62] . . . . .	55
5.19	PI controller used to control the speed of the induction motors . . . . .	56
5.20	Schematic diagram of a three-phase synchronous machine[35] . . . . .	57
5.21	Stator and rotor circuits of a synchronous machine[35] . . . . .	57
5.22	d-axis equivalent circuit[35] . . . . .	59
5.23	q-axis equivalent circuit[35] . . . . .	59
5.24	Torque produced by the original 4100 kVA generator . . . . .	61
5.25	Torque produced by a 8200kVA generator at double load . . . . .	61
5.26	Schematic representation of the electric grid . . . . .	64
5.27	Network interface of all sources and consumers . . . . .	65
5.28	Overview of the cutter shaft model components . . . . .	66
5.29	System diagram of the benchmark model including energy storage . . . . .	67
5.30	Top view of the CSD driveline benchmark Simulink model . . . . .	68
5.31	Simulated and measured combined generator current, showing a similar trend with an offset . . . . .	69
5.32	Fitted simulated and measured diesel engine powers . . . . .	70
5.33	Verification of simulated and measured combined main diesel engine power . . . . .	71
6.1	Input for Simulation 1. Data of May 5th, 2016, 19:00 - 19:30 . . . . .	73
6.2	Simulation 1.1 - Load variation on the diesel engines and the maximum load increase . . . . .	74
6.3	Simulation 1.1 - Cumulative distribution function of load variation and maximum allowed change . . . . .	74
6.4	Simulation 1.1 - Load on a single diesel engine and 85% MCR line . . . . .	75
6.5	Simulation 1.2 - Active power demand, generator active power, and ESS active power . . . . .	75
6.6	Simulation 1.2 - Load variation on the diesel engines and the maximum load increase . . . . .	76
6.7	Simulation 1.2 - Flywheel ESS stored energy and flywheel rotational speed . . . . .	76
6.8	Simulation 1.2 - Close-up of Figure 6.5 . . . . .	76
6.9	Simulation 1.3 - Close-up of ESS power from Figure 6.6 . . . . .	77
6.10	Simulation 1.3 - Active power demand, generator active power, and ESS active power . . . . .	77
6.11	Simulation 1.3 - Load variation on the diesel engines and the maximum load increase . . . . .	78
6.12	Simulation 1.3 - Supercapacitor ESS stored energy and voltage . . . . .	78
6.13	Simulation 1.3 - Supercapacitor (dis)charge current . . . . .	78
6.14	Simulation 1.4 - Load on a single diesel engine and 85% MCR line . . . . .	79
6.15	Simulation 2.1 - Load variation on the dual fuel engines and the maximum load change . . . . .	81
6.16	Simulation 2.1 - Cumulative distribution function of load variation and maximum allowed change . . . . .	81
6.17	Simulation 2.2 - Active power demand, generator active power, and ESS active power . . . . .	82
6.18	Simulation 2.2 - Load variation on the dual fuel engines and the maximum load change . . . . .	82
6.19	Simulation 2.2 - Flywheel ESS stored energy and flywheel rotational speed . . . . .	83
6.20	Simulation 2.2 - Close-up of Figure 6.17 . . . . .	83
6.21	Simulation 2.2 - Close-up of ESS power from Figure 6.17 . . . . .	83
6.22	Simulation 2.3 - Active power demand, generator active power, and ESS active power . . . . .	84
6.23	Simulation 2.3 - Load variation on the dual fuel engine and maximum load change . . . . .	84

6.24	Simulation 2.3 - Supercapacitor ESS stored energy and voltage . . . . .	85
6.25	Simulation 2.3 - Supercapacitor (dis)charge current . . . . .	85
7.1	Part of load variation from Simulation 4.3 where exceeding of the loading limit occurred . . .	88
7.2	Air excess ratio, knock limit and misfire limit for Simulation 4.3 . . . . .	88
A.1	Transformation from three-phase to two-phase coordinates . . . . .	96
A.2	Transformation from $\alpha\beta$ to $dq0$ coordinates . . . . .	97
B.1	Example network[34] . . . . .	99
B.2	Primitive network of Figure B.1[34] . . . . .	99
B.3	New currents[34] . . . . .	100
D.1	Power threshold submodel . . . . .	104
D.2	Supercapacitor Simulink model . . . . .	105
D.3	Supercapacitor inputs subsystem . . . . .	106
D.4	Supercapacitor subsystem $R_{ESR}$ losses . . . . .	106
D.5	Supercapacitor subsystem stored energy . . . . .	106
D.6	Flywheel Simulink model . . . . .	109
D.7	Flywheel inputs subsystem . . . . .	110
E.1	Cutter mass-spring system . . . . .	112
E.2	Element inertia part one . . . . .	112
E.3	Element inertia part two . . . . .	113
F.1	Input for Simulations 1 and 2 - Data from May 5th 2016, 19:00 - 19:30 . . . . .	115
F.2	Input for Simulations 3 and 4 - Data from May 1st 2016, 00:00 - 00:30 . . . . .	116
F.3	Input for Simulations 5 and 6 - Data from May 22nd 2016, 22:00 - 22:30 . . . . .	117
F.4	Input for Simulations 7 and 8 - Data from May 2nd 2016, 06:00 - 06:30 . . . . .	118
F.5	Input for Simulations 9 and 10 - Data from May 11th 2016, 18:00 - 18:30 . . . . .	119
F.6	Data from dredging operation, May 1st - May 9th . . . . .	120
F.7	Data from dredging operation, May 10th - May 19th . . . . .	120
F.8	Data from dredging operation, May 20th - May 30th . . . . .	120

# List of Tables

2.1	Cutter suction dredger specifications . . . . .	7
2.2	Voltage and frequency variations of AC power supplies[5] . . . . .	9
2.3	Submerged dredge pump motor specifications . . . . .	9
2.4	Cutter motor specifications . . . . .	9
2.5	Inboard dredge pump motor specifications . . . . .	10
2.6	Main generator specifications . . . . .	10
2.7	MAN 9L 48/60CR diesel engine specifications[38] . . . . .	10
4.1	Energy storage requirements from January 2016 data . . . . .	26
4.2	Average number of ESS cycles for January 2016 data . . . . .	32
4.3	Power management system inputs . . . . .	33
4.4	Values to determine energy storage module cost . . . . .	35
4.5	ESS dimensions and weight[2][22] . . . . .	35
4.6	Fuel prices . . . . .	35
5.1	Base values used to convert SI unit to per unit quantity . . . . .	37
5.2	Maxwell BCAP3000 P270 K04 Supercapacitor specifications[40] . . . . .	40
5.3	CCM EMAFER RxV-II Flywheel module specifications[22] . . . . .	44
5.4	Specific fuel consumption diesel engine[38] . . . . .	47
5.5	Wärtsilä 12V34DF specifications [63] . . . . .	48
5.6	Specific fuel consumption dual fuel engines[63] . . . . .	49
5.7	Measured dredge pump motor parameters . . . . .	52
5.8	Motor parameters used in simulations . . . . .	53
5.9	Generator parameters used in simulations . . . . .	61
5.10	Diesel engine power Normalized Root Mean Square Error . . . . .	70
6.1	Energy storage sizing for diesel engine simulations . . . . .	73
6.2	Energy storage system volume and weight . . . . .	73
6.3	Energy storage sizing for diesel engine simulations . . . . .	80
6.4	Energy storage system volume and weight . . . . .	80
7.1	Diesel engine simulation cost analysis . . . . .	87
7.2	Dual fuel engine simulation cost analysis . . . . .	88
F.1	Simulation 1 results . . . . .	115
F.2	Simulation 2 results . . . . .	115
F.3	Simulation 3 results . . . . .	116
F.4	Simulation 4 results . . . . .	116
F.5	Simulation 5 results . . . . .	117
F.6	Simulation 6 results . . . . .	117
F.7	Simulation 7 results . . . . .	118
F.8	Simulation 8 results . . . . .	118
F.9	Simulation 9 results . . . . .	119
F.10	Simulation 10 results . . . . .	119

# Nomenclature

$A$	Surface area of electrodes	$[m^2]$
$B$	Admittance matrix	$[\Omega^{-1}]$
$C$	Capacitance	$[F]$
$D$	Engine bore	$[m]$
$D$	Distance between electrodes	$[m]$
$e$	Voltage	$[V]$
$E_{fw}$	Flywheel stored energy	$[J]$
$E_{fw,eff}$	Effective flywheel stored energy	$[J]$
$E_{sc}$	Supercapacitor stored energy	$[J]$
$E_{sc,eff}$	Effective supercapacitor stored energy	$[J]$
$E_{sc,max}$	Maximum supercapacitor stored energy	$[J]$
$E_{sc,min}$	Minimum supercapacitor stored energy	$[J]$
$f_{base}$	Base frequency	$[Hz]$
$f_{nom}$	Nominal frequency	$[Hz]$
$i$	Number of cylinders	$[-]$
$i_d$	Direct axis current	$[pu]$
$i_q$	Quadrature axis current	$[pu]$
$\vec{i}$	Current vector	$[A]$
$I_{base}$	Base current	$[A]$
$I_{cont}$	Maximum continuous current	$[A]$
$I_d$	Discharge current	$[A]$
$I_L$	Leakage current	$[A]$
$I_{nom}$	Nominal current	$[A]$
$I_{peak}$	Peak current	$[A]$
$I_{cs}$	Crankshaft inertia	$[kg \cdot m^2]$
$I_{fw}$	(Engine) flywheel moment of inertia	$[kg \cdot m^2]$
$J$	Flywheel moment of inertia	$[kg \cdot m^2]$
$J_{de}$	Engine shaft moment of inertia	$[kg \cdot m^2]$
$J_g$	Generator shaft moment of inertia	$[kg \cdot m^2]$
$J_l$	Load moment of inertia	$[kg \cdot m^2]$
$J_m$	Motor moment of inertia	$[kg \cdot m^2]$
$k$	Number of strokes	$[-]$
$L_{base}$	Base inductance	$[H]$
$L_m$	Magnetizing inductance	$[pu]$
$L_{ss}$	Stator self-inductance	$[pu]$
$L_{rr}$	Rotor self-inductance	$[pu]$
$M$	Torque	$[Nm]$
$M_{em}$	Electric machine torque	$[Nm]$
$M_{nom}$	Nominal torque	$[Nm]$
$n_{nom}$	Nominal speed	$[rpm]$
$n_{max}$	Maximum speed	$[rpm]$
$p$	Number of poles	$[-]$
$\vec{p}$	Current vector	$[A]$
$P_d$	Discharge power	$[W]$
$P_{DE}$	Diesel engine power	$[W]$

$P_{ESS}$	ESS power	[W]
$P_{load}$	Power demand	[W]
$P_{loss}$	Power loss	[W]
$P_{max}$	Maximum power	[W]
$P_{nom}$	Nominal power	[W]
$P_{total}$	Total installed power	[W]
$P_{sd}$	Self-discharge power	[W]
$Q$	Reactive power	[VAr]
$R$	Resistance	[ $\Omega$ ]
$R_a$	Armature resistance	[pu]
$R_{ESR}$	Equivalent series resistance	[ $\Omega$ ]
$R_r$	Rotor resistance	[pu]
$R_s$	Stator resistance	[pu]
$s$	Slip	[-]
$S_{base}$	Base apparent power	[VA]
$S_{nom}$	Nominal apparent power	[VA]
$S$	Engine stroke	[m]
$t$	Time	[s]
$T'_{do}$	Transient direct axis open circuit time constant	[pu]
$T''_{do}$	Subtransient direct axis open circuit time constant	[pu]
$T'_{dq}$	Transient quadrature axis open circuit time constant	[pu]
$T''_{dq}$	Subtransient quadrature axis open circuit time constant	[pu]
$u_d$	Direct axis voltage	[pu]
$u_q$	Quadrature axis voltage	[pu]
$\bar{u}$	Voltage vector	[V]
$U_0$	Supercapacitor initial voltage	[V]
$U_{base}$	Base voltage	[V]
$U_{ia}$	Average ideal rectifier voltage	[V]
$U_{line}$	Line voltage	[V]
$U_{min}$	Minimum voltage	[V]
$U_{nom}$	Nominal voltage	[V]
$U_r$	Rated voltage	[V]
$X$	Reactance	[ $\Omega$ ]
$X_d$	Direct axis synchronous reactance	[pu]
$X'_d$	Direct axis transient reactance	[pu]
$X''_d$	Direct axis subtransient reactance	[pu]
$X_l$	Leakage reactance	[ $\Omega$ ]
$X_m$	Magnetizing reactance	[ $\Omega$ ]
$X_q$	Quadrature axis synchronous reactance	[pu]
$X'_q$	Quadrature axis transient reactance	[pu]
$X''_q$	Quadrature axis subtransient reactance	[pu]
$X_r$	Rotor reactance	[pu]
$X_s$	Stator reactance	[pu]
$Z$	Impedance	[ $\Omega$ ]
$Z_{base}$	Base impedance	[ $\Omega$ ]
$\alpha$	Angular acceleration	[rad/s <sup>2</sup> ]
$\delta$	Rotor angle	[ $^\circ$ ]
$\epsilon_0$	Dielectric constant	[-]
$\epsilon_r$	Dielectric constant	[-]
$\eta_{cyc}^{FW}$	Flywheel round trip efficiency	[-]
$\eta_{cyc}^{SC}$	Supercapacitor round trip efficiency	[-]
$\kappa$	Energy loss coefficient	[-]
$\lambda$	Rate of decay coefficient	[-]
$\lambda$	Air excess ratio	[-]
$\tau_{base}$	Base torque	[Nm]
$\psi$	Magnetic flux	[Wb]

$\Psi_{base}$	Base magnetic flux	[Wb]
$\vec{\Psi}$	Magnetic flux vector	[Wb]
$\omega$	Flywheel rotational speed	[rad/s]
$\omega_0$	Initial rotational speed	[rad/s]
$\omega_{e,base}$	Base electric angular speed	[rad/s]
$\omega_m$	Mechanical speed	[rad/s]
$\omega_{max}$	Flywheel maximum rotational speed	[rad/s]
$\omega_{min}$	Flywheel minimum rotational speed	[rad/s]
$\omega_r$	Rotor electric angular speed	[rad/s]
$\omega_s$	Stator electric angular speed	[rad/s]
$\omega_{shaft}$	Shaft angular speed	[rad/s]
$\cos \phi$	Power factor	[-]

# Abbreviations

AC	Alternating current
AFR	Air to fuel ratio
BMEP	Brake mean effective pressure
CSD	Cutter suction dredger
DC	Direct current
DOD	Depth of discharge
ESR	Equivalent series resistance
ESS	Energy storage system
LNG	Liquefied natural gas
LHV	Lower heating value
MCR	Maximum continuous rating
MDO	Marine diesel oil
MN	Methane number
NRMSE	Normalized Root Mean Square Error
PEC	Power electronic converter
PF	Power factor
PI	Proportional-integral
PID	Proportional-integral-derivative
PMS	Power management system
SFC	Specific fuel consumption
SOC	State of charge
TDC	Top dead centre
THD	Total harmonic distortion
TPF	Total power factor

# Preface

This thesis concludes my studies at the Delft University of Technology and is submitted in partial fulfillment of the requirements for the degree of Master of Science in Mechanical Engineering, specializing in Mechanical Systems and Integration. This research has been conducted at the R&D department of IHC Systems B.V. in Sliedrecht.

First of all, I would like to thank Peter de Vos for his supervision and guidance, not only during this last year, but during my entire master's. Secondly, I would like to thank Klaas Visser for his valuable contributions during our progress meetings.

Also, I would like to thank all the people at the IHC Systems R&D department, who provided me with a nice working environment. In particular, I would like to express my gratitude to Pieter Vos and Jacco Osnabrugge for their daily supervision and valuable contributions. From IHC MTI, I would like to thank Benny Mestemaker for taking time to help me during this project.

And of course, last but not least, I would like to thank my family, friends and girlfriend for their support, especially during the last stages of this project.

Menno van Leeuwen  
*Delft, June 2017*

# Chapter 1

## Introduction

### 1.1 General background

Cutter suction dredgers are a type of hydraulic dredgers used to excavate soil ranging from sand to hard rock. The cutter suction dredger is equipped with a cutting head at the inlet of its suction tube. The cutting head is used to loosen material which is then transported through its suction pipe. Cutter suction dredgers are often used to excavate hard soils where other types of dredging vessels would be ineffective. This research is conducted at IHC Systems, which is part of Royal IHC. Royal IHC designs and builds vessels and equipment for dredging and offshore purposes. Amongst these vessels are various cutter suction dredgers.

A growing concern regarding environmental impact has led to stricter emission regulations. One of the solutions to comply with new regulations is to use liquefied natural gas (LNG) as fuel.[16] Various dredging vessels powered by dual fuel engines are already planned to be built capable of using LNG as fuel.[50][51] Besides the first LNG-fueled trailing suction hopper dredgers '*Minerva*' and '*Scheldt River*', Royal IHC will also be building the '*Spartacus*', which will be the first LNG-fueled and largest cutter suction dredger ever built.[52]

Also, there have been considerable developments in the marine industry concerning hybrid power generation systems in the last decade.[39][64] The term hybrid as used in this research refers to the description that is often used in the automotive industry, where these hybrid systems have been more common for several years. According to this definition, a hybrid power generation system is comprised of more than one energy source, like a combination of a prime mover using combustible fuel and a battery energy storage system. This type of hybrid power generation system has been applied to various vessels that have an operational profile that contains a lot of changing power requirements. Hybrid power generation systems have proven to result in increased efficiency and lower emissions on various offshore vessels with a number of different operational modes, like platform supply vessels during dynamic positioning, but also on vessels like harbor tugs.[8][23] Especially these kinds of vessels, that have an operational profile that contains a wide spread in load demand can benefit from hybrid power generations systems. Hybrid solutions in power generation systems can also provide more flexibility in the ship design and can smoothen power demand from the main engines, which can be necessary for alternative fueling options like LNG. Although the operational profile of a cutter suction dredger suggests it is a good candidate for a hybrid power generation system, so far no hybrid cutter suction dredgers exist. Research has been conducted where the application of battery energy storage to the cutter suction dredger's driveline is investigated to reduce emissions.[18] While it is concluded that the addition of a battery energy storage system is not cost-effective in this application, the relevance of further research into cutter suction dredgers fueled by LNG is emphasized.

## 1.2 Problem definition

The total combined diesel power that is available on a cutter suction dredger is often far greater than the power that is required during dredging operations. Large fluctuations in power demand occur during dredging operation caused by, for instance, changes in the type of soil that is being cut. Figure 1.1 shows an example of the measured active power demand on the power generation system of a cutter suction dredger during dredging operation, where the rapid change in load demand can be seen.

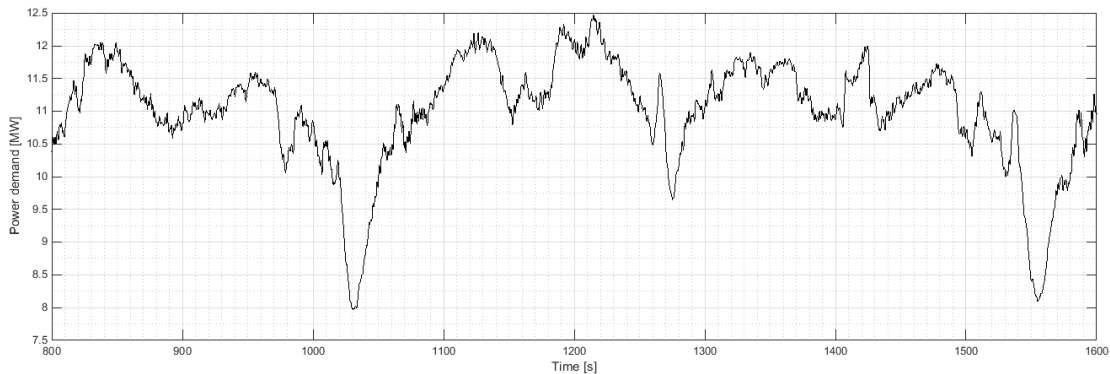


Figure 1.1: Typical power demand on the power generation system during cutter suction dredger operation

In general, the necessary power is supplied by generators which are driven by diesel engines. The total amount of power that is installed on the cutter suction dredger is determined by the maximum load conditions. These maximum load conditions, however, only make up a small portion of the total operational profile. Therefore, the average load on the generators, and consequently on the diesel engines, is often much lower than the optimal load. For the type of marine diesel engines that are found in the cutter suction dredger that is being considered in this research the optimal load is around 85% of the engine's maximum continuous rating. It is at this point that the specific fuel consumption of the engine is at its lowest.[54] Besides the increased fuel consumption that is associated with the running of diesel engines at low loads there is also an increase in engine wear, as pointed out by engine manufacturers.[58]

The control of the load increase is essential for turbocharged engine, as the turbocharger needs time to accelerate before it is able to deliver the required amount of air. Similarly, sufficient time is needed to achieve even temperature distribution in engine components. For dual fuel engines running on LNG these harsh loading conditions present another problem. More specific loading requirements apply to these engines to be able to continue running on LNG. When the loading limit is exceeded the engine will switch from the combustion of natural gas to the combustion of diesel fuel to prevent knocking or misfiring of the dual fuel engine. Therefore, control of the load variation to smoothen power demand is even more critical for dual fuel engines.

## 1.3 Research objective

The main objective of this research is to investigate hybrid solutions that are suitable as an alternative for the existing power generation system on a cutter suction dredger. The proposed power generation system should be capable of providing a solution for the problem definition stated in Section 1.2. The main objective can be summarized by the following research question:

*Is it beneficial to add an energy storage system to the power generation system of a cutter suction dredger to reduce the load fluctuations on the main engines in order to smoothen power demand on the power generation system?*

In order to answer the research question stated in this section the load on the cutter suction dredger driveline will first be analyzed. This is done by using data obtained during several months of dredging operation. Based on this analysis a decision can be made on the type of energy storage system deemed best suitable for this application with the use of available literature.

To determine the performance of different hybrid power generation systems a dynamic simulation model will be created for each configuration. For the simulation models clear boundaries need to be defined to be able to determine which details have to be modeled. Once the model boundaries are defined, the original cutter suction dredger driveline is modeled to provide a benchmark that is used to determine the performance of the proposed hybrid driveline configurations. To be able to evaluate the performance criteria need to be defined to evaluate each configuration. Based on the evaluation the research question will be answered for each of the proposed hybrid configurations.

## 1.4 Thesis outline

The second chapter of this thesis further elaborates on the cutter suction dredger. The driveline configuration is described and the major components are identified. The ship's electric network is also described in this chapter, which forms the bases for the simulation model. Furthermore, the dredging process is described and an initial analysis of the load on the main diesel engines is given.

Chapter 3 contains a theoretical description of the hybrid systems and alternate driveline configurations that are considered. The term hybrid as used in this research is further explained. Typical applications of hybrid systems are described followed by the placement of energy storage systems in the CSD driveline. At the end of this chapter, a description of dual fuel engines is given.

At the beginning of Chapter 4 the methodology used for the determination of the energy storage system size is described. A detailed load analysis is done followed by the ESS power and energy requirements that results from this analysis. Based on the stated requirements a selection is made on what type of ESS is best suited for this application. Next, a theoretical description is given on supercapacitor ESS, flywheel ESS, and considerations concerning these systems. At the end of the chapter the criteria used to evaluate the performance of the proposed configurations are described.

In Chapter 5 the details of the simulation models are described and how they are implemented into the total model. Model verification and/or validation is given for each component where it is considered necessary. At the end of the chapter a topview is given of the complete benchmark cutter driveline model, including the electrical network and power-generation system. The validation of the benchmark model validation is included at the end of Chapter 5.

The simulation results are described in Chapter 6. In this chapter a detailed description is given for the first set of simulations that has been performed. A summary of the total set of simulations is provided in Appendix F.6. The observations made during simulations are described in this chapter and are used to formulate the conclusions and recommendations in Chapter 7.

Chapter 7 includes the conclusions that are drawn based on the conducted simulations. The rest of this chapter consists of a discussion regarding the total research and recommendations for future research.

## Chapter 2

# Cutter suction dredger

In this chapter the cutter suction dredger and the working principle of the cutter suction dredger is described. An energy flow diagram is provided to indicate the flow of energy in the cutter suction dredger's driveline. Also, a single line diagram is given to give a simplified overview of the electric power system. Furthermore, an overview and description is given of the major driveline components.

### 2.1 General description

The cutter suction dredger (CSD) is a stationary operating self-propelling type of dredging vessel mainly used for the excavation of waterways and harbors. The CSD is equipped with a cutter head that excavates both hard and soft types of soil before it is sucked up by dredge pumps. Excavated material is typically transported hydraulically via pipelines connected to the back of the vessel. In some cases, however, the dredger can have on-board loading facilities. The CSD can easily be distinguished from other suction dredgers by its spud poles, which provide the CSD with high dredging accuracy.[60] With CSD operating depths of up to 50 meters are currently being reached. Figure 2.1 shows the side view and top view of a relatively small CSD, indicating the major components.

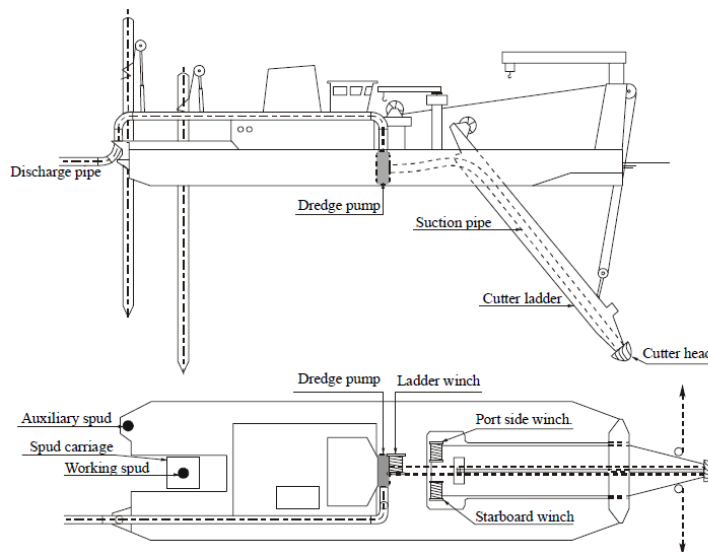


Figure 2.1: Side view (top picture) and top view (bottom picture) of a CSD[60]

The CSD is equipped with a cutter ladder at the front of the vessel, which can be lowered to the desired depth by the ladder winches. A suction pipe runs through the cutter ladder and is used to transport loosened material. The loosened material is transported through the suction pipe to the discharge by dredge pumps. A rotating cutter head is located in front of the suction pipe entrance and is used to cut soil. At the rear of the vessel two spud poles are located, which are used to maintain position during dredging operation. Figure 2.2 shows a detailed figure of the cutter ladder and its major components.

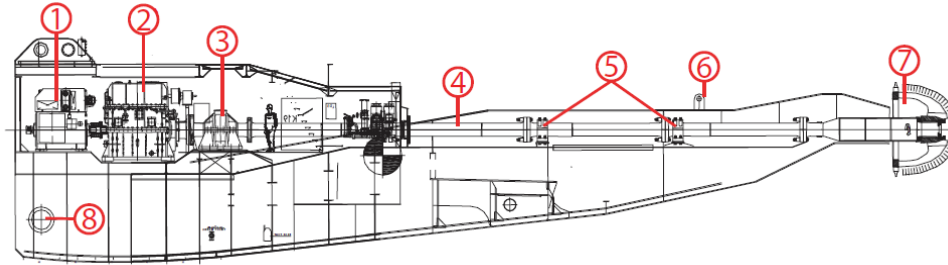


Figure 2.2: Cutter ladder and major components.[3] 1.) Electric motors 2.) Gearbox 3.) Thrust bearing 4.) Cutter shaft 5.) Radial bearings 6.) Lifting wire hinges 7.) Cutter head 8.) Main hinge

## 2.2 Dredging operation

Figure 2.3 shows a top view of the CSD and indicates how dredging operation takes place. On both sides of the CSD an anchor is lowered to the bottom by anchor booms. The anchor lines are connected to the winches and are used to rotate the CSD from one side to the other.

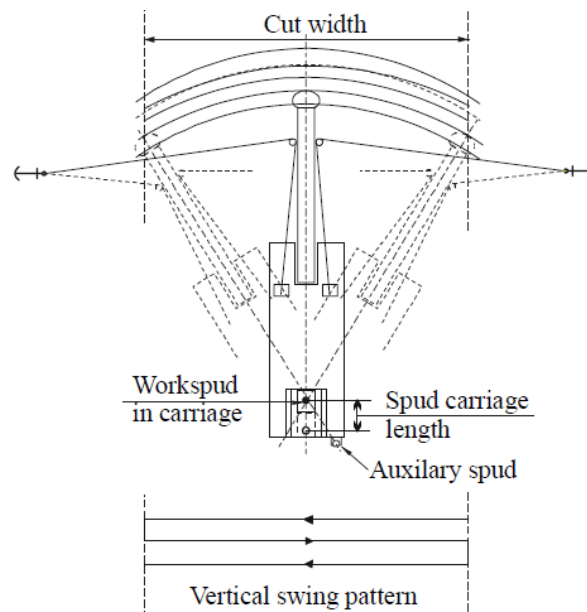


Figure 2.3: CSD dredging operation [60]

At the rear of the vessel a spud pole is put in the ground around which the CSD rotates. The spud pole system consists of a fixed spud pole and a moving spud pole on a carriage system powered by a hydraulic cylinder and makes sure the CSD stays in its current location. The cutter head is lowered to the bottom making arc shaped cuts in the soil, as indicated by the lines at the top of Figure 2.3. After each cut the spud pole carriage system is moved back, propelling the CSD forward so that a new cut can be made by alternating pulling of the left and right side winches. When the spud pole carriage system reached the limit of the hydraulic cylinder the fixed spud pole is lowered. Next, the moving spud pole is lifted from the ground and the carriage system is moved back to its starting position, after which the process is repeated.

## 2.3 Driveline configuration

The main power generation system of the CSD considered in this thesis is a diesel-electric power generation system consisting of two main diesel engines, each driving two 4500 *kVA* generators. Table 2.1 gives an overview of the total installed power and the power division between the larger driveline components. Besides the main power generation system there is an auxiliary and emergency generator installed, but since the focus of this research is on the effect of the load variation caused by the dredging process on the main engines these will not be further discussed.

Table 2.1: Cutter suction dredger specifications

<b>Total installed power</b>	23545 <i>kW</i>
<b>Main diesel engines</b>	2 x 10800 <i>kW</i>
<b>Main generators</b>	4 x 690 V, 4500 <i>kVA</i>
<b>Dredge pump power</b>	10600 <i>kW</i>
<b>Cutter system power</b>	3500 <i>kW</i>
<b>Propulsion power</b>	3180 <i>kW</i>
<b>Winch power</b>	1500 <i>kW</i>
<b>400V Board net</b>	1500 <i>kW</i>

The energy flow diagram in Figure 2.4 shows the chain of energy conversion from the energy source to the energy users and provides a good overview of the flow of energy in the total cutter suction dredger's driveline.

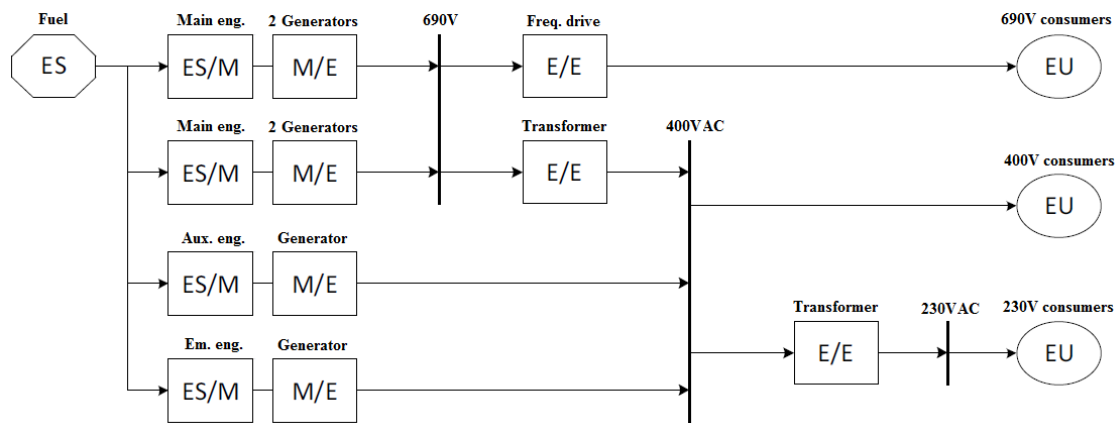


Figure 2.4: Cutter suction dredger energy flow diagram[33]

The abbreviations in Figure 2.4 denote the following:

- **ES** - Energy source in the form of fossil fuel.
- **ES/M** - Energy source to mechanical conversion by combustion of fuel in internal combustion engines.
- **M/E** - Mechanical to electrical conversion by electric generators driven by the internal combustion engines.
- **E/E** - Electrical to electrical conversion by converters to change the voltage.
- **EU** - Use of energy by the dredge pumps, cutter motors, et cetera.

## 2.4 Driveline components

The main driveline components are described in this section. The specifications given here for each of the components will be used for the simulation models in Chapter 5. The following components are considered:

- **Dredge pumps**, two inboard dredge pumps, one submerged dredge pump
- **Cutter motors**, two electric motors connected to a single gearbox
- **Side winches**, one electric motor located on each side of the cutter ladder
- **Spud pole system**
- **Power generation system**, consisting of two main diesel engines and four generators
- **Cutter system**, used here to describe all cutter ladder components excluding the submerged dredge pump and cutter motors

Note that the propulsion system is not considered, since it is not operational during dredging operation. To give a more detailed overview of the CSD driveline and its components the single line diagram is displayed in Figure 2.5.

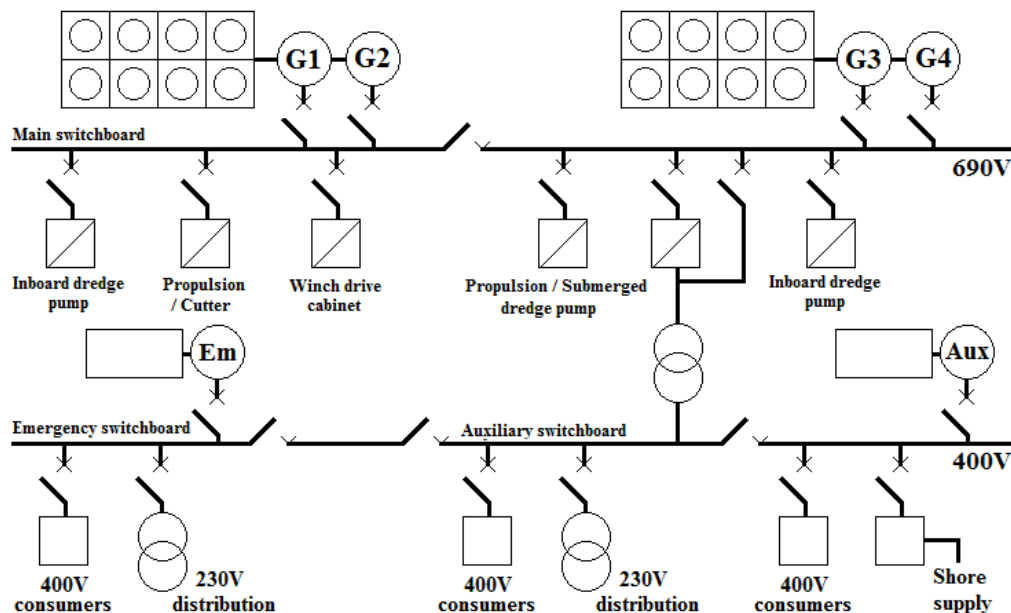


Figure 2.5: Cutter suction dredger single line diagram

## Class requirements

As with all seagoing vessels, cutter suction dredgers are subject to compliance with a number of regulations. The class requirements for the vessel considered here are defined by Bureau Veritas. In particular, the regulations concerning the quality of the power supply have to be considered for this research. The quality of the power supply is expressed in a maximum allowed variation in voltage and frequency under which all electrical components are capable of operating satisfactorily.[5] The allowed maximum voltage and electric frequency variations of AC power supplies are specified in Table 2.2.

Table 2.2: Voltage and frequency variations of AC power supplies[5]

Parameter	Variations	
	Continuous	Transient
Voltage	+6% – 10%	±20% (recovery time: 1.5 s)
Frequency	±5%	±10% (recovery time: 5 s)

### 2.4.1 Electric motors

The electric dredge pump motors and cutter motors as found in the CSD driveline are squirrel cage type induction motors. A more detailed description on induction motors can be found in Section 5.3.3. The electric motors found in the cutter driveline are of the same as the electric motor used for the submerged dredge pump. The difference between the two motors is the electric frequency and voltage at which they are operated, which results in a difference in power output. The specifications of the 2200 kW electric motors used in the dredge pumps are shown in table 2.3.

Table 2.3: Submerged dredge pump motor specifications

<b>Nominal power</b> $P_{nom}$	2200 kW
<b>Nominal voltage</b> $U_{nom}$	660 V
<b>Nominal speed</b> $n_{nom}$	1400 rpm
<b>Nominal frequency</b> $f_{nom}$	46.91 Hz
<b>Nominal current</b> $I_{nom}$	2345 A
<b>Nominal torque</b> $M_{nom}$	15006 Nm
<b>Power factor</b> $\cos\phi$	0.9
<b>Number of poles</b> $p$	4
<b>Efficiency</b> $\eta$	0.962

The cutter motors are operated at an electrical frequency of 40 Hz and a voltage of 566 V resulting in a power output of 1750 kW instead of 2200 kW. Table 2.4 shows the specifications of the cutter motors.

Table 2.4: Cutter motor specifications

<b>Nominal power</b> $P_{nom}$	1750 kW
<b>Nominal voltage</b> $U_{nom}$	566 V
<b>Nominal speed</b> $n_{nom}$	1200 rpm
<b>Nominal frequency</b> $f_{nom}$	40 Hz
<b>Nominal current</b> $I_{nom}$	2033 A
<b>Nominal torque</b> $M_{nom}$	13926 Nm
<b>Power factor</b> $\cos\phi$	0.91
<b>Number of poles</b> $p$	4
<b>Efficiency</b> $\eta$	0.965

There are two 4200 *kW* inboard dredge pumps. The specifications for the inboard dredge pumps is shown in Table 2.5.

Table 2.5: Inboard dredge pump motor specifications

<b>Nominal power</b> $P_{nom}$	4200 <i>kW</i>
<b>Nominal voltage</b> $U_{nom}$	660 <i>V</i>
<b>Nominal speed</b> $n_{nom}$	1650 <i>rpm</i>
<b>Nominal frequency</b> $f_{nom}$	55.23 <i>Hz</i>
<b>Nominal current</b> $I_{nom}$	4212 <i>A</i>
<b>Power factor</b> $\cos\phi$	0.90
<b>Number of poles</b> $p$	4
<b>Efficiency</b> $\eta$	0.968

## 2.4.2 Generators

The power generation system consists of four synchronous generators. A more detailed description on the synchronous generators can be found in Section 5.3.5. As can be seen in Figure 2.5 two generators are driven by a single diesel engine. For each diesel engine there is a gearbox between the engine shaft and the two generators to get the desired rotational speed of the generator shafts. The specifications of the main generators can be found in Table 2.6. Besides the main generators there is an auxiliary generator and an emergency generator installed on the CSD. These generators are not considered in this thesis.

Table 2.6: Main generator specifications

<b>Apparent power</b> $S_{nom}$	4500 <i>kVA</i>
<b>Nominal power</b> $P_{nom}$	4230 <i>kW</i>
<b>Nominal voltage</b> $U_{nom}$	690 <i>V</i>
<b>Synchronous speed</b> $n_{nom}$	500 <i>rpm</i>
<b>Nominal frequency</b> $f_{nom}$	50 <i>Hz</i>
<b>Nominal current</b> $I_{nom}$	3765 <i>A</i>
<b>Number of poles</b> $p$	12
<b>Power factor</b> $\cos\phi$	0.94
<b>Efficiency</b> $\eta$	0.9475 - 0.975

## 2.4.3 Diesel engines

The CSD driveline main power generation is driven by two medium speed four-stroke MAN L9 48/60CR diesel engines rated at 10800 *kW* each. Since the CSD is fully diesel-electric, including propulsion, the main diesel engines will be running at a constant speed. Specifications for the diesel engines are shown in Table 2.7:

Table 2.7: MAN 9L 48/60CR diesel engine specifications[38]

<b>Nominal power</b> $P_{nom}$	10.8 <i>MW</i>
<b>Nominal speed</b> $n_{nom}$	500 <i>rpm</i>
<b>Strokes per cycle</b> $k$	4
<b>Number of cylinders</b> $i$	9
<b>Engine bore</b> $D$	0.48 <i>m</i>
<b>Engine stroke</b> $S$	0.6 <i>m</i>
<b>Moment of inertia crankshaft</b> $I_{cs}$	3565 <i>kg · m<sup>2</sup></i>
<b>Moment of inertia flywheel</b> $I_{fw}$	3102 <i>kg · m<sup>2</sup></i>

### 2.4.4 Cutter

The cutter as referred to here consists of the cutter head, the cutter shaft and the gearbox connecting the cutter shaft to the electric motor shafts. The gearbox has a gear ratio of around 1:40, which results in a cutter head rotational speed of 30 rpm.

## 2.5 Typical cutter load

Figure 2.6 shows an example of a typical load that is seen on the CSD power generation system during dredging operation and is shown here to give an initial impression of the load on the CSD driveline. The bottom figure shows the variation of the load. It can be seen that a change of over  $500 \text{ kW/s}$  occurs regularly. The total power demand is around  $10 \text{ MW}$  and a maximum of  $12 \text{ MW}$  is reached during the hour of dredging operation shown in the figure. This means that the load on the main diesel engines is roughly 50% of the engine's maximum continuous rating (MCR). A more detailed analysis of the cutter load is given in Section 4.1.1.

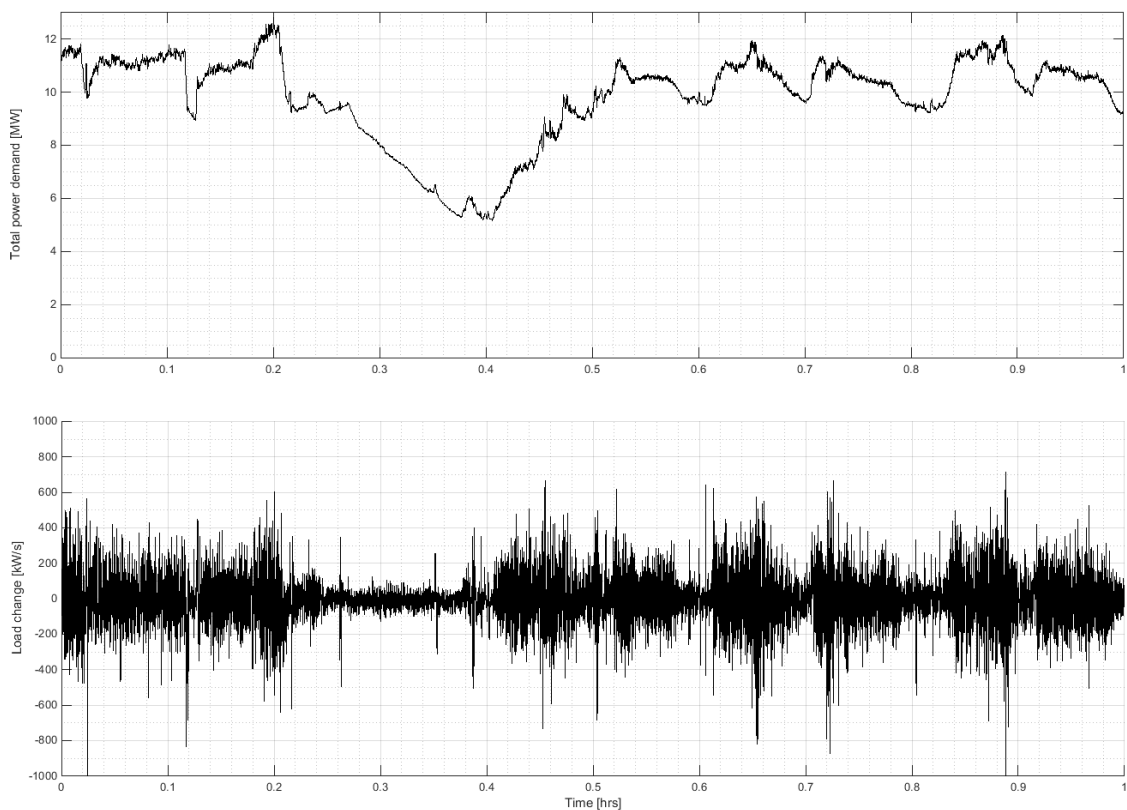


Figure 2.6: Example of power demand and variation during dredging operation

## Chapter 3

# Hybrid systems and alternate configurations

### 3.1 Definitions

#### Hybrid systems

When referring to a hybrid propulsion system two different definitions are often used. The first definition describes a propulsion system comprised of a combination of a mechanical and electrical drive or a combination of two different prime movers.[33] Mechanical energy is delivered by a prime mover like a diesel engine or gas turbine, which converts chemical energy into mechanical energy. Additionally, there is one or more electric motor that can provide propulsion power as well. The energy required by the electric motor is often supplied by the ship's electric power plant. Similarly, a propulsion system comprised of a combination of a diesel engine and gas turbine is also considered a hybrid system with this definition.

The second definition describes a power generation system where a prime mover is combined with an energy storage device. Typically, the goal of this configuration is to have the energy storage device deliver energy when power demand becomes higher and take up energy when power demand becomes lower, i.e. peak shaving and dip filling. As stated in Chapter 1, the latter description is commonly used in the automotive industry and will also be used in this thesis to define a hybrid power generation system.

#### Diesel and dual fuel engines

Due to the lack of an established nomenclature confusion may arise concerning the term *diesel engine* and *dual fuel engine*. Both of the mentioned engines are reciprocating internal combustion engines operating on the Diesel cycle. This means that only air is compressed and fuel is injected into the combustion chamber near top dead center (TDC). When the air-fuel mixture reaches a certain temperature and pressure, spontaneous combustion occurs.[17] While both engine types considered here have the same principle of operation, a distinction is made in the type of fuel that is combusted. Therefore, the term diesel engine is used to refer to engines that use solely liquid diesel oil as fuel. The term dual fuel engine refers to an engine with the same principle of operation but uses natural gas as primary fuel. For the combustion of natural gas still a small amount of liquid diesel fuel is injected as pilot fuel.[30]

## 3.2 Applications

Hybrid systems are often used to reduce fuel consumption and reduce maintenance of the prime mover due to fewer running hours. Hybrid systems can, however, also be used provide an increased level of redundancy, improving the availability and reliability of the system.[46] The application of hybrid systems can therefore be divided into two types, *peak shaving* and *spinning reserve*. Both concepts are described in this section.

### 3.2.1 Peak shaving

Peak shaving is a form of load leveling used to deal with significant fluctuations in power demand over relatively short time intervals. The load on the primary source of power generation is reduced by having a secondary source, the energy storage system, provide additional power when necessary. Figure 3.1 shows a representation of peak shaving. The blue line in the figure indicates the power demand over time. The red line indicates the power that is delivered by the primary power generation system. The difference between the total power required and the power delivered by the primary power generation system is supplied by the energy storage system. Furthermore, when the power demand is suddenly lowered the energy storage system is used to take up the excess energy.

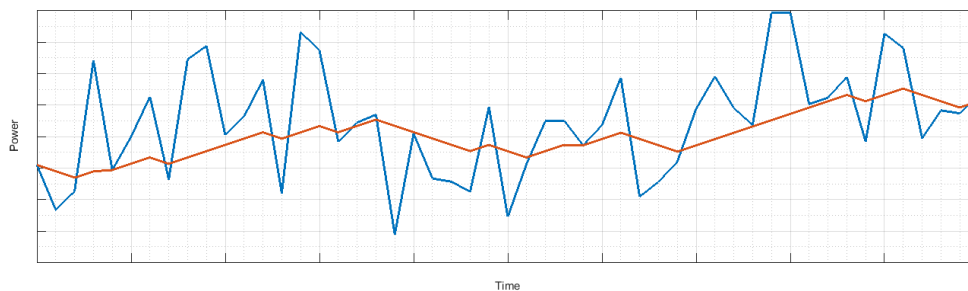


Figure 3.1: Peak shaving

### 3.2.2 Spinning reserve

In some operations a certain amount of redundancy is required to ensure safety or efficiency. These can be applications where the required power can be delivered by having only part of the total power generation system running, but regulations require a larger power reserve. This situation is applicable to dynamic positioning operations, for instance.[49] The power reserve, which can be additional operational generators, is referred to as the spinning reserve. The energy storage in hybrid propulsion systems can be used to ensure the additional amount of available power, eliminating the need to have more generators running. Secondly, in many cases the power from an energy storage system can be made available almost instantaneously. This is unlike internal combustion engines, which require a significant amount of time to start up.

In this thesis a hybrid power-generation system is proposed to reduce the load variation on the main diesel generators by applying peak shaving as described here. The concept of spinning reserve is not applicable here and will not be further discussed.

### 3.3 Energy storage configuration

Figure 3.2 shows the addition of an energy storage system to the energy flow diagram displayed in Figure 2.4. In this configuration the energy storage system is connected to the DC bus of an electric motor's frequency drive through a bidirectional DC/DC converter, which allows for charging and discharging of the ESS.

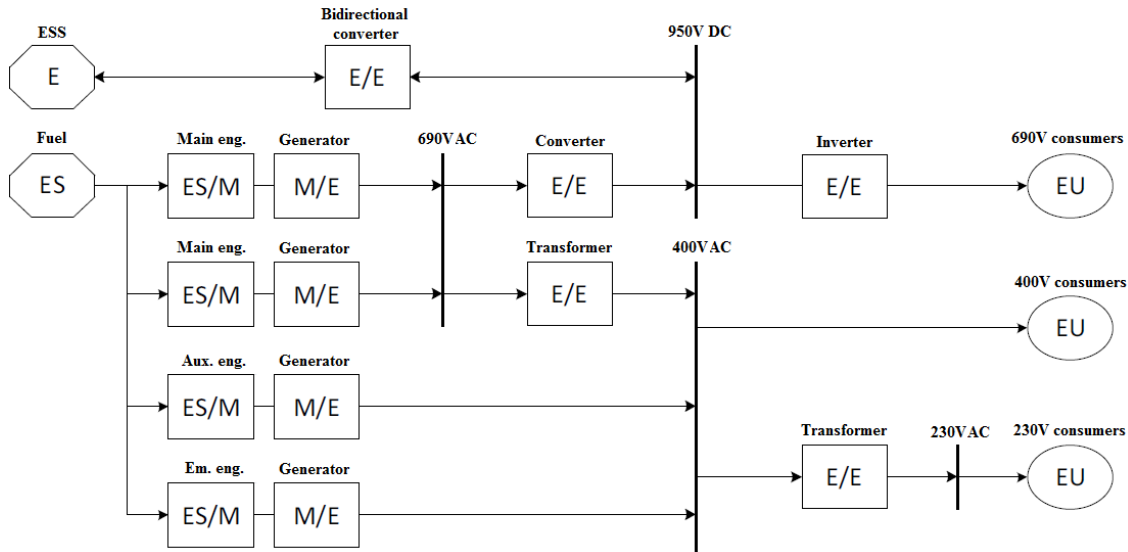


Figure 3.2: Cutter suction dredger energy flow diagram including energy storage system

The placement of the energy storage system follows from the ESS topology proposed in [55], where it is used to maintain stability during sudden load changes.

### 3.4 Dual fuel engines

Due to emission regulations and the trend towards utilizing renewable fuels a rising interest can be seen in the application of gas engines where commonly diesel engines are used. Dual fuel engines have the capability of running on either diesel or gas. Engines running on gas are, however, less suitable for applications with a demand for fast transient response behavior.[16][27] The operating range and limitations of dual fuel engines are discussed in this section.

#### 3.4.1 Transient response behavior

In principle, the same combustion process takes place in a gas engine as in a diesel engine running on diesel fuel. The power is increased by injecting additional fuel while the amount of combustion air that is being delivered remains the same. Consequently, the engine is temporarily running on a rich gas-air mixture until the turbocharger is able to deliver the required amount of air.[27] The combustion of diesel has a wide range of operation. The load acceptance for gas is subject to more specific limitations. Figure 3.3 shows the injection of fuel at constant air flow.

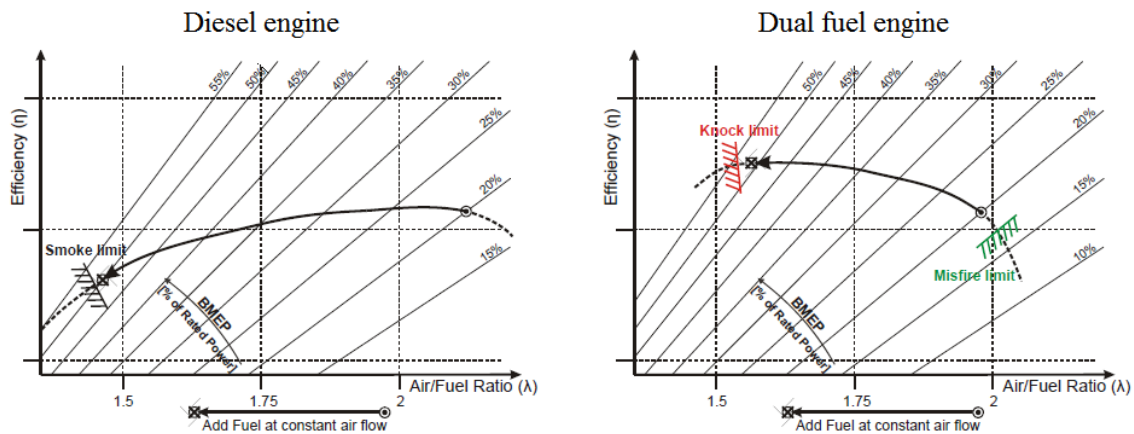


Figure 3.3: Injecting additional fuel at constant air flow at low loads[27]

The left figure shows the wide range of operation for the combustion of diesel, restricted by air to fuel ratios too rich for normal combustion, called the smoke limit. Similarly, there is a limit for mixtures too lean for diesel engines which results in misfires. If there is not enough air in the combustion chamber parts of the mixture can auto-ignite before reaching the flame front. This is referred to as knocking. If there is too much air, flame propagation can be hindered which results in misfiring.[16] A detailed explanation of knock and misfire is given in Section 4.1.2. The right figure shows the limitations for the combustion of gas, also restricted by the knock limit for low air to fuel ratios and by the misfire limit for high air to fuel ratios. As can be seen in the figure the operating range is narrower than for the combustion of diesel. The operating range becomes even narrower at higher loads, as can be seen in Figure 3.4. As a result the allowed load step becomes smaller at higher loads. The quality of the gas affects the loading capability of engines running on gas. Gas with a low methane number shows lower resistance to knocking, for instance.[42]. Note that in both Figure 3.3 and Figure 3.3 the efficiency is indicated for diesel engines and dual fuel engines on gas without numerical values, and do not necessarily indicate the correct values.

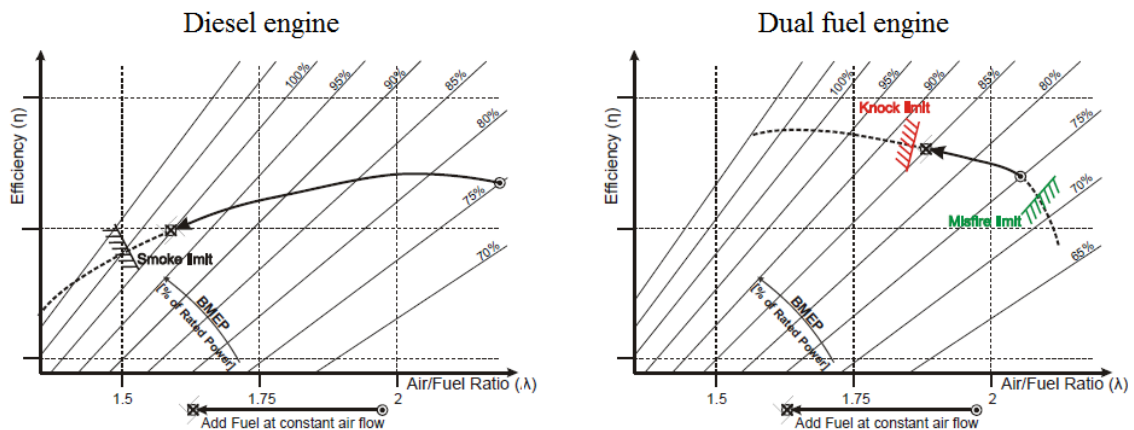


Figure 3.4: Injecting additional fuel at constant air flow at high loads[27]

### 3.4.2 Loading capability

Both the allowed instant load steps and ramped load increase is lower for dual fuel engines than it is for diesel engines. The combination of these limits are displayed in Figure 3.5 for the dual fuel engines that are being considered. The different lines in the figure indicate the maximum allowed increase in load for a corresponding initial load level. A distinction is made between normal loading and the maximum allowed

capability in gas mode.[63]

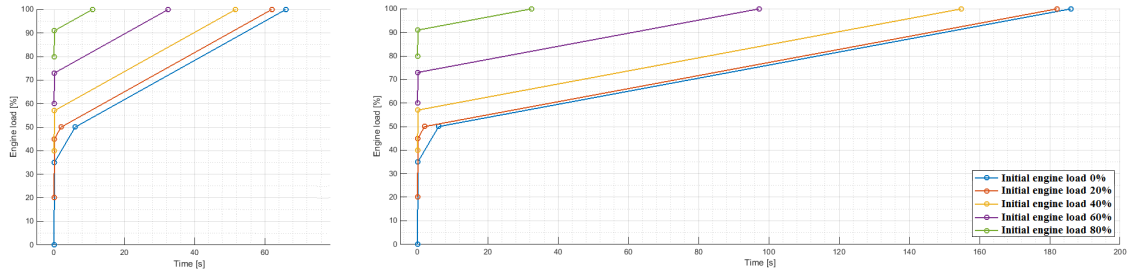


Figure 3.5: Left: Maximum loading capability in gas mode. Right: Normal loading capability in gas mode[63]

Above the maximum loading capability, displayed on the left in Figure 3.5, the engine automatically switches to diesel-mode. Switches to gas-mode can only be made when the load on the engine is below 80% of the MCR. After each load step a recovery time of about 10 seconds is required before another load step is allowed. Switching back to gas mode is possible if the conditions mentioned above are met and takes about two minutes to complete. Reducing the load in gas mode is also restricted. The allowed load step down should be taken as follows: 100-75-45-0%, where the required recovery time between each step has to be taken into account.[63]

### 3.4.3 Loading limit

Figure 3.6 shows the cumulative distribution function of the load steps from data from dredging operation in January 2016. The blue line in the figure indicates the maximum load capacity in gas mode. Above this limit the engine will switch to diesel mode to prevent engine knock.[63] Figure 3.6 shows a cumulative distribution function of the load variation as shown in Figure 2.6 over a longer period of time. The dashed lines in the figure indicate the engine limits of the dual fuel engines. From the figure, it can be concluded that 88% of the load variation is below the maximum loading limit. This means that switching to diesel mode during dredging operation is inevitable.

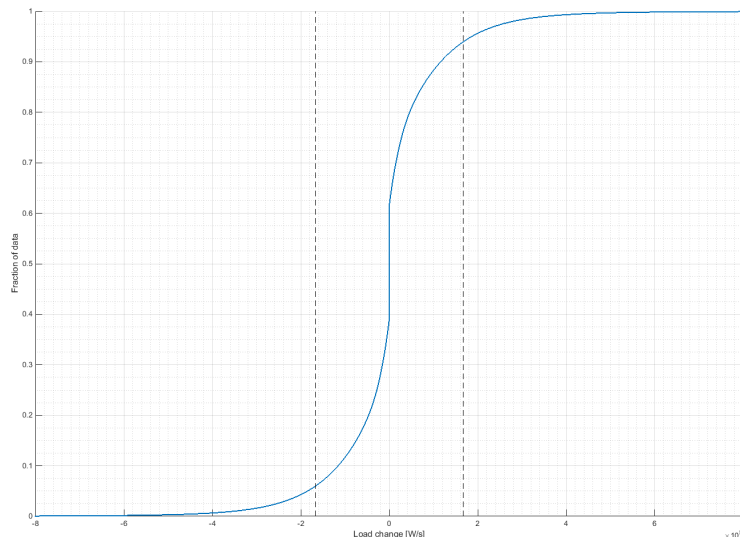


Figure 3.6: Cumulative distribution function of load variation

### 3.4.4 Gas fuel quality

The quality of gas fuel is of importance for engine operation. The gas quality is commonly expressed by the methane number (MN) and can vary significantly due to different gas compositions. Although methane is the main component in LNG certain amounts of ethane, propane, and butane can be present. The MN is comparable to the octane number for liquid fuels, which is typically used with gasoline fuels for passenger cars. Similar to the octane number, the MN represents the resistance to knock of a gas.[28] Figure 3.7 shows the limitation in engine output resulting from a different MN and charge air receiver temperature. For Western Europe engines are designed to run on a minimum MN of 80.[28][63]

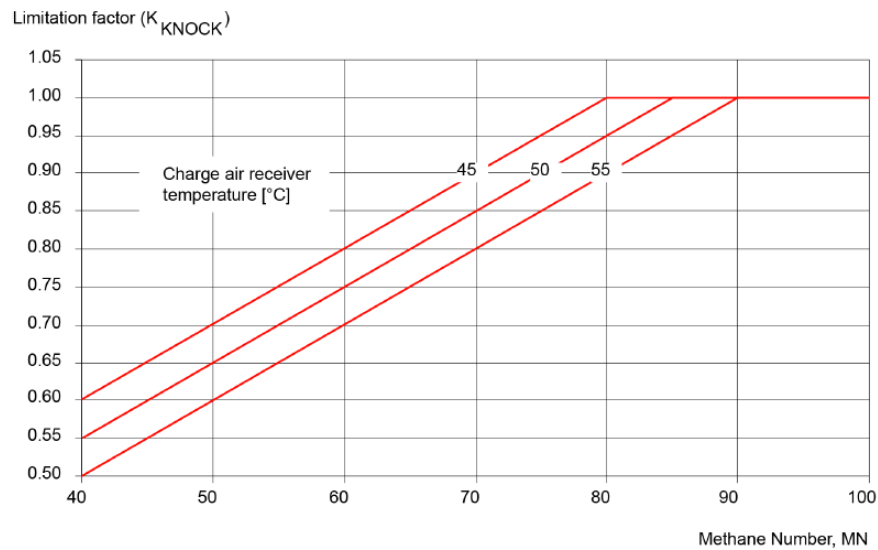


Figure 3.7: Output limitations due to methane number and charge air receiver temperature[63]

## 3.5 Alternate engine configuration

When considering the loads as displayed in Figure 1.1 and Figure 2.6 it becomes clear that the amount of power required during dredging operation is a lot smaller than the total amount of power the diesel engines are able to deliver. As a result, both engines are running at relatively low ratings which is unfavorable for fuel consumption. Besides the hybrid configuration and dual fuel engines, an alternate engine configuration is therefore proposed as well for comparison. Figure 3.8 and Figure 3.9 show the engine rating ranges at which fuel efficiency is highest for a configuration with two and four engines, respectively. Having several smaller engines would allow for switching off one of the engines or the examples of power demand given above. The average rating of the remaining engines is consequently increased, increasing fuel efficiency. Furthermore, the running hours on the engines is reduced which lowers maintenance cost. Although this is not necessarily related to the research objective, the alternate engine configuration is merely mentioned as alternative for the fuel and maintenance cost reduction.

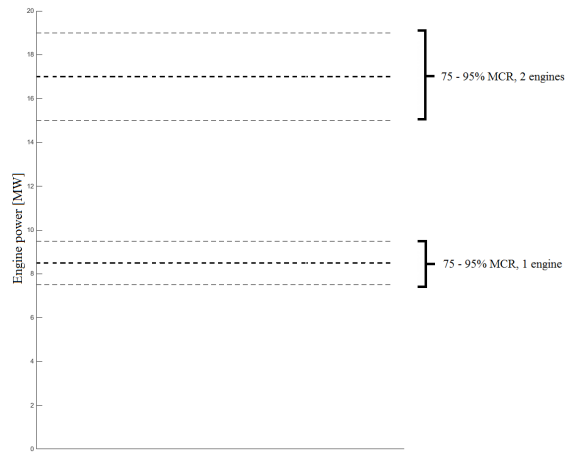


Figure 3.8: 75% - 95% MCR with two engines

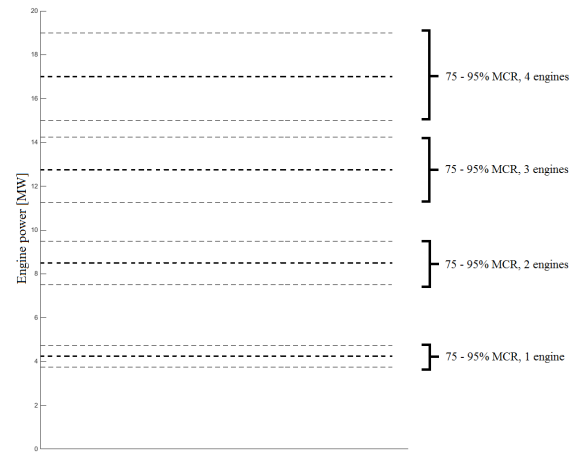


Figure 3.9: 75% - 95% MCR with four engines

# Chapter 4

## Energy storage systems

### 4.1 Energy storage sizing

In this chapter the methodology to determine the power and storage capacity of the energy storage system is explained. First the load on the cutter driveline is analyzed after which the power and energy storage requirements are determined. In short, the following steps are taken for the determination of the energy storage power and energy requirements:

1. From dredging operational data the rate of change of the electric load on the power generation system changes is determined.
2. A limit is defined for the rate of change at which the load on the diesel engines can be increased and decreased.
3. The minimum amount of power delivered by the ESS equals the largest peak that exceeds the set limit.
4. The minimum amount of energy that the ESS has to be able to store is the amount of energy that is delivered during the longest period of continuous discharging.

This methodology will be explained in more detail in this chapter.

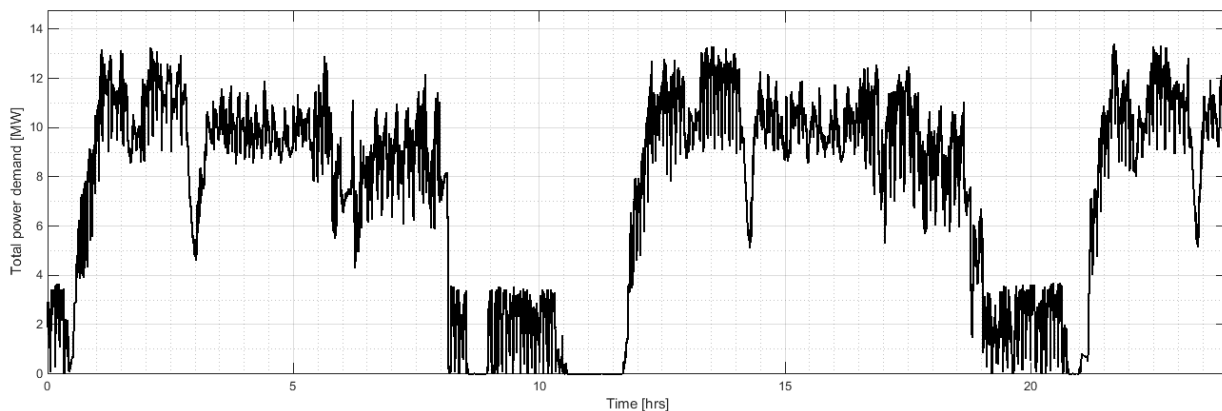


Figure 4.1: Total power demand during twenty-four hours of dredging operation

### 4.1.1 Load analysis

For the determination of the power and storage requirements of the energy storage system the electric load during dredging operation is analyzed. For this analysis data from dredging operations from October 2015 until June 2016 has been used. The data consists of

The conditions during these dredging operations vary from light conditions when cutting packed sand to harsh conditions when cutting rock mixtures. The data is therefore considered to give a good representation of typical operating conditions for a cutter suction dredger. Figure 4.1 shows the total power demand of all consumers of the cutter suction dredger during twenty-four hours of dredging operation. The maximum amount of power that is required is around sixty percent of the total installed diesel power. This power demand is a good representation of all power data that has been used.

To give a better picture of the power demand of the different components the separate power data of seventy-two hours of dredging operation is shown in Figure 4.2. From this figure it becomes clear that the amount of power required by the three dredge pumps combined is around 70% of the total amount of power that is required. This is a lot higher than the amount of power required by the cutter motors, which is around 25% of the total power demand.

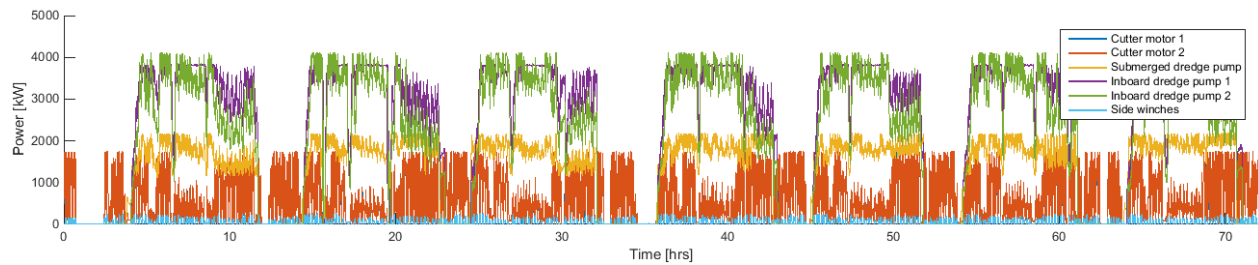


Figure 4.2: Power demand of the different components in the CSD driveline during nine days of dredging operation

However, if the rate of change of the power demand of the different components is considered a completely different picture is painted. This result is shown in Figure 4.3, where the difference in results can immediately be seen. Even though the amount of power required by the cutter motors is lower than that of the dredge pumps, fluctuation in power demand are far greater than for the dredge pumps.

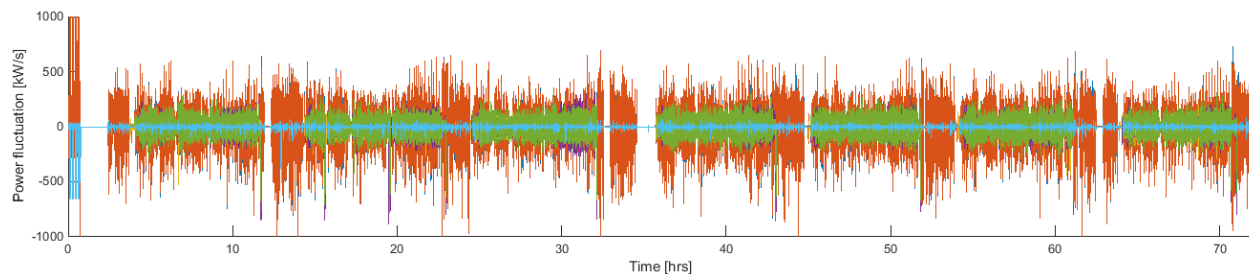


Figure 4.3: Load fluctuation of the different components in the CSD driveline over time

### 4.1.2 Air excess ratio

In Section 3.4 knock and misfire of internal combustion engines is introduced. These terms will be further explained in this section. Both concepts are partially dependent on the air to fuel ratio, as can be seen in Figure 4.4. On the y-axis the brake mean effective pressure (BMEP) is indicated, which is a measure for

the specific power of reciprocating engines.[54]. The air excess ratio, denoted by  $\lambda$ , is the ratio between the actual air to fuel ratio and the stoichiometric air to fuel ratio, as shown in Equation 4.1. The stoichiometric air to fuel ratio  $\sigma$  is defined as the ratio between the exact amount of air required for complete combustion of a given amount of fuel, i.e. the exhaust gas contains no more oxygen or unburned fuel.

$$\lambda = \frac{afr}{\sigma} \quad (4.1)$$

The BMEP is proportional to the air swallowing capacity of the engine. For turbocharged engines the turbocharger pressure determines the amount of trapped air in the cylinders and therefore the BMEP. When the load on the engine is increased a drop in speed will occur. To bring the engine back to the desired speed more fuel is required, which can be injected instantly. Consequently, more air is required for combustion. The turbocharger requires time to supply the required amount of air, however. As a result the air to fuel ratio will drop to a more rich mixture which can lead to engine knocking, as can be seen in Figure 4.4. The term knocking is used to refer to the unwanted spontaneous combustion of the air and fuel mixture. Normally, the mixture is combusted near TDC. If there is insufficient air the conditions for proper combustion will be met by part of the mixture, auto-igniting it before the normal flame front would reach the mixture.[16] When there is a sudden decrease in engine load the opposite effect is created. Less fuel is required to maintain engine speed and consequently less air is needed. If the air excess ratio becomes sufficiently high resulting in a very lean mixture misfiring can occur. When the engine experiences misfiring the amount of air trapped in the cylinders is too high and prevents propagation of the flame. In addition, a decrease in exhaust gas pressure occurs which causes the compressor pressure to drop below the pressure inside the inlet receiver. As a result the airflow is reversed which is referred to as compressor surging, and is to avoided.

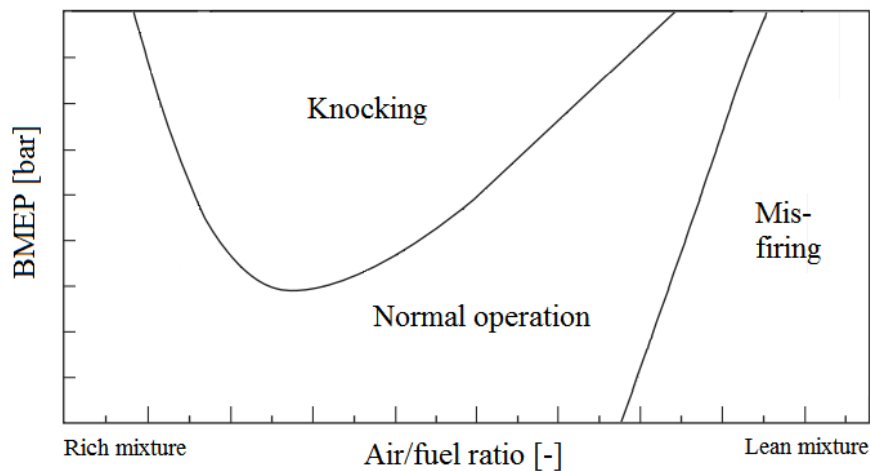


Figure 4.4: Knock and misfire range

### Diesel engine maximum ramp-up

Sizing of the energy storage system is done by defining a maximum for the power increase per unit of time experienced by the power generation system. This maximum value is determined by the engine's maximum transient load conditions stated by the manufacturer. This is defined as a maximum percentage increase in engine power per unit of time. The loading curves for different conditions are displayed in Figure 4.5. The three curves in the figures are described as follows[38]:

- **1. Normal loading, 36 kW/s.** The generally recommended rate at which load can be applied to the diesel engine, assuring uniform heat input and exhaust smoke opacity below ten percent.

- **2. Short loading**,  $180 \text{ kW/s}$ . Applicable when the engine has reached normal operating temperature. This increased rate of load increase results in visible exhaust gas, with opacity up to thirty percent. The visible gas results from incomplete combustion due to insufficient air. Referring to Figure 4.4, the engine will be running on a lower air excess ratio, because the turbocharger is not able to provide the required amount of air yet.
- **3. Emergency loading**,  $360 \text{ kW/s}$ . The rate at which load can be applied in case of emergency. This is close to the engine limit and results in visible exhaust gas. Similar to the short loading, visible smoke in the exhaust gas occurs due to the addition of fuel while the required amount of air can not yet be supplied.

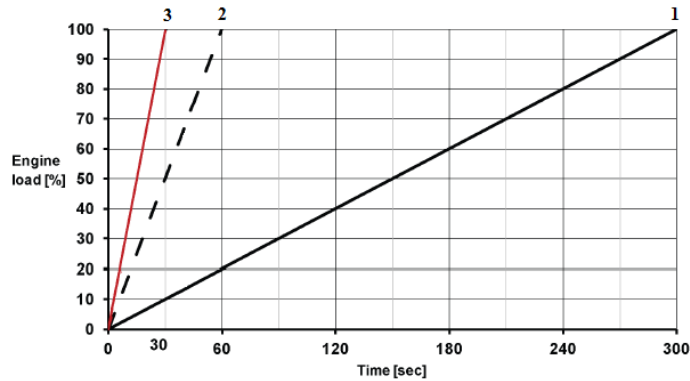


Figure 4.5: Diesel engine maximum ramp-up[38]

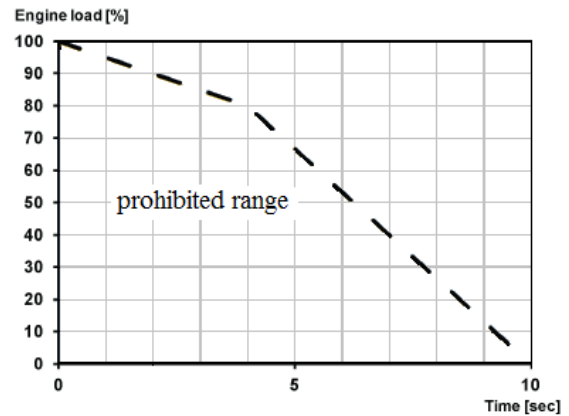


Figure 4.6: Maximum ramp-down[38]

The rate at which the power demand from Figure 4.1 changes over time is displayed in Figure 4.7. The values for the maximum ramp up of two diesel engines are shown to indicate when the limit is exceeded. For the normal loading condition, corresponding to a rate of  $72 \text{ kW/s}$  for two diesel engines, it seems that all load changes exceed the limit. In contrast, the emergency loading limit is rarely exceeded during these twenty-four hours.

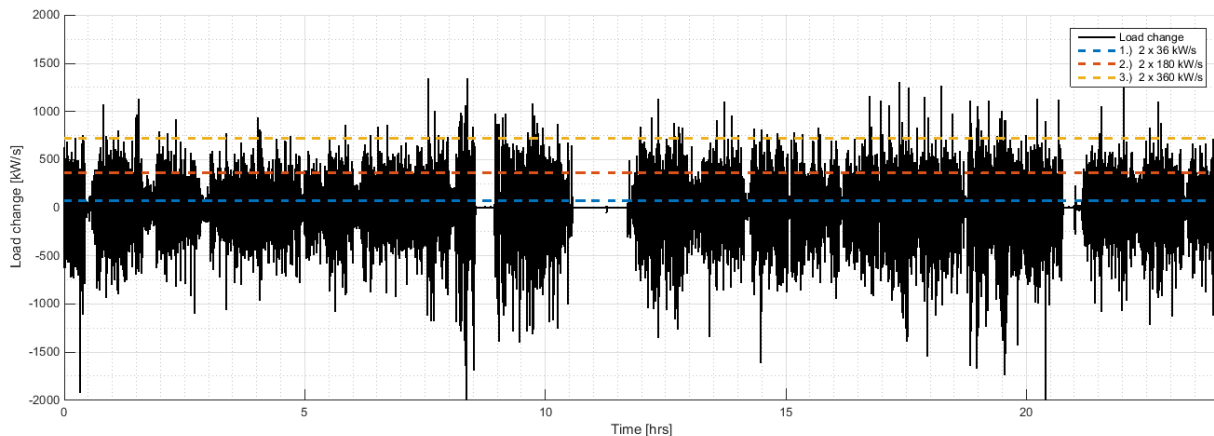


Figure 4.7: Load variation of power shown in Figure 4.1

To get a better picture a cumulative distribution of the total load variation is shown in Figure 4.8. From this figure it becomes clear that for this load roughly 75% of the time the transient load is within the limit set by the manufacturer. For the normal loading and emergency loading curves these values correspond to 98% and over 99%, respectively. Depending on which limit is used, the excess power required will be delivered by the energy storage system at the instances at which the allowed increase in load is exceeded. Furthermore, from

Figure 4.3, where the separate load fluctuations are shown, it can be concluded that with this sizing methodology the requirements of the energy storage system will be mostly determined by the load on the cutter motors.

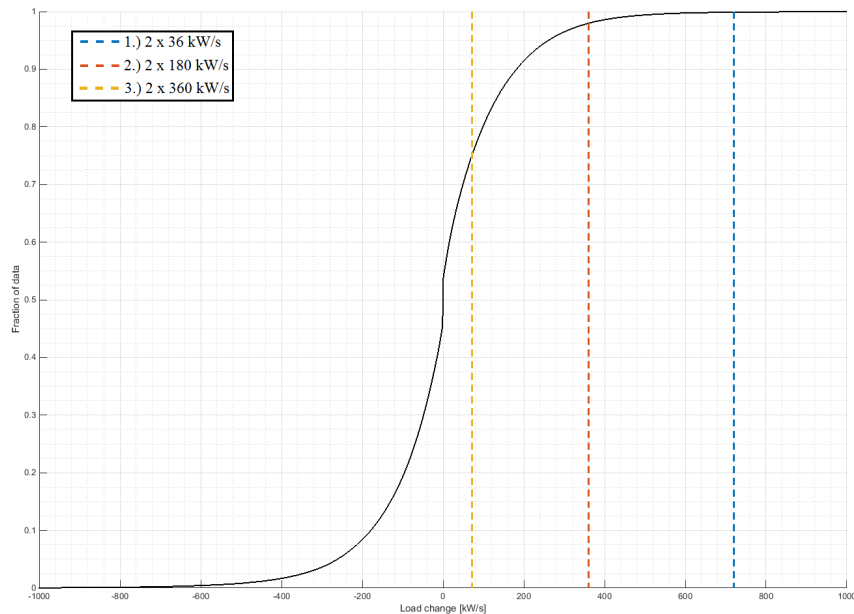


Figure 4.8: Cumulative distribution of load variation

### Maximum ramp-down

Similar to the maximum ramp-up, a limit is defined for the rate at which the load can be reduced. The main reason for a limit on the rate at which the load on the diesel engines can be reduced is to prevent turbocharger surging, as described above. Often a valve called a waste gate is installed on the diesel engine which is used to divert the exhaust gas away from the turbochargers turbine, allowing faster decrease in engine load.[54] The ramp-down limit can be used to determine when the energy storage system is to take up excess energy. The rate at which the load can be reduced is much higher than the rate at which it can be increased, however. For the diesel engines considered here, this rate is set as  $-540 \text{ kW/s}$  at full load to 80% load and  $-1080 \text{ kW/s}$  below 80% load, as can be seen in Figure 4.6.[38] In Figure 4.8 it can be seen that this limit is exceeded less than 1% of the time. Of course, the limit at which the load can be reduced per unit of time can be reduced. By having the load on the diesel engines decrease slower than the demand of power the excess power can be used to charge the energy storage system. The total amount of energy that can be stored is determined by the power requirements over a certain period of time. This storage requirement can be influenced by shifting the engine limits, which will be further discussed in Section 4.1.4. In Figure 4.8 it can be seen that the cumulative distribution is centered around zero. The rate at which the load is reduced and the amount of instances that this occurs more or less seems to equal the load increase. A similar conclusion can be drawn when considering Figure 4.7. The initial ramp-down limit is therefore chosen to be equal to the ramp-up limit, because then charging and discharging of the ESS will be roughly balanced.

### Load steps

Besides the maximum ramp-up and ramp-down described above a maximum is defined for instant load steps allowed for the engine. Figure 4.9 shows the allowed load steps in both diesel and gas mode. The required time between load steps is dependent on the recovery time of the engine's turbocharger. For the determination whether a consecutive load step is allowed the inlet receiver pressure and air excess ratio have to be

known and processed in the power management system, significantly increasing its complexity. As these signal might not always be available, load steps are not taken into consideration so the ESS power is determined by the maximum ramp-up and ramp-down.

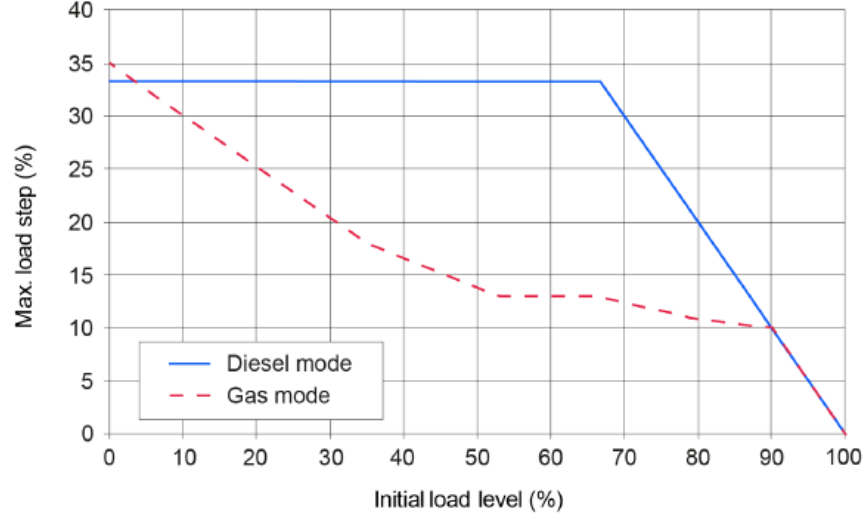


Figure 4.9: Allowed load steps in diesel mode and gas mode[63]

### 4.1.3 Power requirements

The minimum power that has to be delivered by the energy storage system is determined by the maximum allowed increase and decrease in load per second of the diesel engines. According to literature load steps are allowed provided that the turbocharger has sufficient time to recover.[38][63]. For the determination when the ESS is activated, however, load steps are not considered, making the allowed load on the engines somewhat conservative. Therefore, when the increase in power demand, load  $P_{load}$ , is greater than the allowed ramp-up limit that is set for the diesel engines, the load on the diesel engines  $P_{DE}$  is increased by the maximum allowed ramp-up. The additional power to meet the load demand is then supplied by the energy storage system. Alternately, when the decrease in load is greater than the allowed ramp-down, the load on the diesel engine is decreased by the maximum allowed power decrease by charging the energy storage system to store the excess of power delivered by the diesel engines. These conditions are described by:

$$if \quad \frac{P_{load}(t+dt) - P_{load}(t)}{dt} > \left(\frac{dP}{dt}\right)_{max}^{up} \quad \rightarrow \quad P_{load}(t+dt) = P_{DE}(t) + \left(\frac{dP}{dt}\right)_{max}^{up} \cdot dt \quad (4.2)$$

$$if \quad \frac{P_{load}(t) - P_{load}(t+dt)}{dt} > \left(\frac{dP}{dt}\right)_{max}^{down} \quad \rightarrow \quad P_{load}(t+dt) = P_{DE}(t) - \left(\frac{dP}{dt}\right)_{max}^{down} \cdot dt \quad (4.3)$$

The amount of power delivered or consumed by the energy storage system  $P_{ESS}$  is then given by:

$$P_{ESS} = P_{load} - P_{DE} \quad (4.4)$$

The power  $P_{ESS}$  from Equation 4.4 is used to determine the minimum power requirements of the energy storage system to meet the conditions set by Equation 4.2 and Equation 4.3. The amount of power delivered by the energy storage system compared to the total installed power is referred to as the degree of hybridization and is defined as:

$$DOH = \frac{P_{ESS}}{P_{Total}}$$

#### 4.1.4 Energy requirements

The energy requirements of the energy storage system determine the minimum amount of energy that can be stored. After defining the power requirements as described in Section 4.1.3 the minimum energy storage can be determined. This is done by simulation of  $P_{ESS}$  determined in Equation 4.4. Figure 4.10 shows an example of this simulation at an arbitrary maximum diesel engine ramp-up to indicate the ESS sizing methodology. Note that no ramp-down limit is included in this figure.  $P_{ESS}$  is indicated by the yellow line. The total power requirement and the power delivered by the generators are indicated by the blue and red lines, respectively.

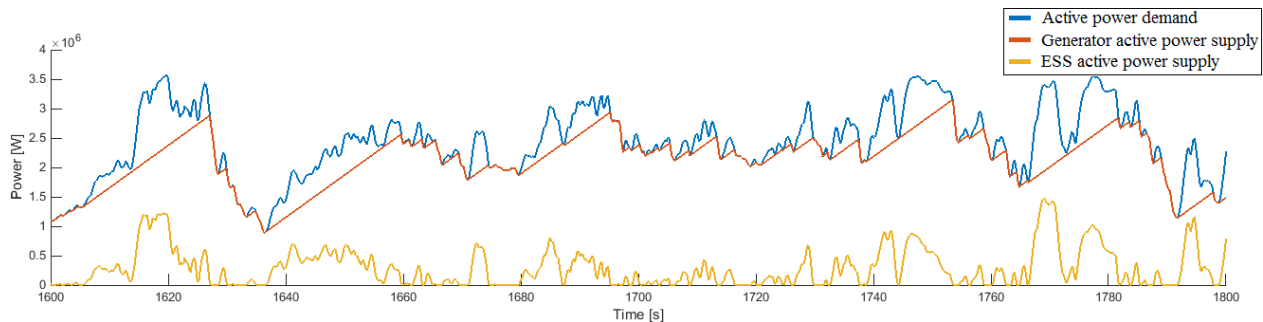


Figure 4.10: Simulation of  $P_{ESS}$  at an arbitrary maximum diesel engine ramp-up

The initial estimate for the storage capacity is based on the maximum peak of each dataset in terms of consumed energy. The minimum amount of energy that can be stored is chosen to be equal to the amount of energy that is delivered between the start and end of the maximum discharge peak. This is done by evaluating the energy used during an interval between every instance where  $P_{ESS}$  is greater than zero and again becomes equal or smaller than zero. Out of all these intervals, a maximum peak in terms of discharge energy is then found for each dataset. The maximum value out all datasets is used to determine the storage capacity. For more details on the ESS sizing methodology, the reader is referred to Appendix C. Next, the maximum allowed power ramp-down for the diesel engines is determined. When the power demand is decreased faster than the ramp-down limit the excess energy is used to charge the energy storage system. Figure 4.11 shows the same load as used in Figure 4.10 with the addition of an arbitrarily chosen ramp-down limit to indicate the charging process. The black line indicates the engine ramp-down resulting in charging of the energy storage system. Secondly, in order to charge the ESS a minimum load on the generators can be defined besides the maximum allowed ramp-down. Only once the ESS is fully charged, the generator load is allowed to fall below this limit.

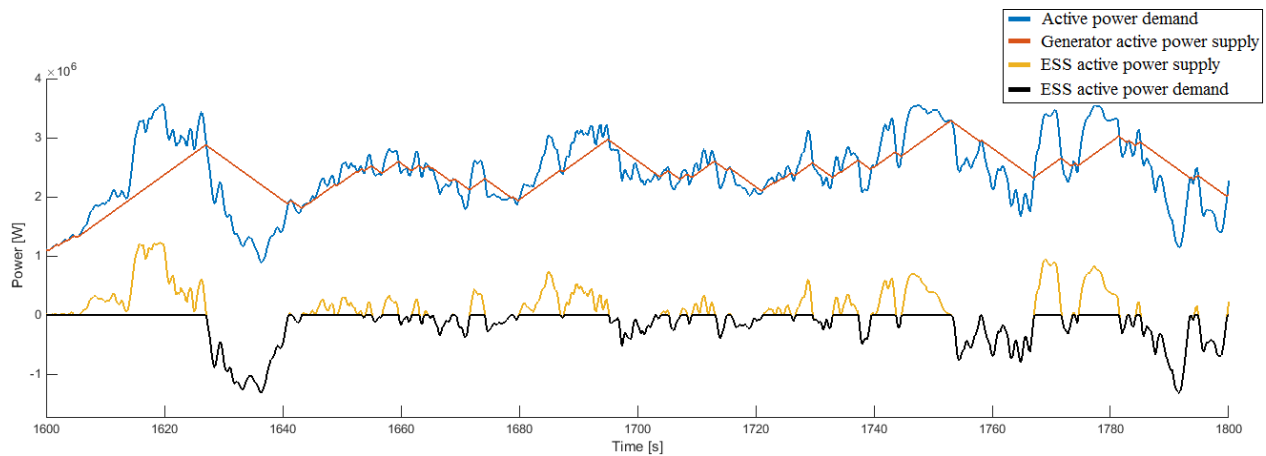


Figure 4.11: Simulation of  $P_{ESS}$  with an added arbitrary maximum diesel engine ramp-down

## 4.2 Energy storage system selection

Table 4.1 shows the results of applying the methodology described in this chapter data from continuous dredging operation from January 2016. Based on the results shown in Table 4.1 a selection is made for the types of energy storage system that are used for simulations.

Table 4.1: Energy storage requirements from January 2016 data

Maximum load increase	Minimum power	Minimum energy	Maximum discharge time
360 kW/s	922 kW	1.80 MJ	4.2 s
180 kW/s	1.91 MW	7.53 MJ	9.0 s
36 kW/s	2.68 MW	57.37 MJ	66.2 s

Figure 4.12 shows a Ragone plot, which can be used for performance analysis of various energy storage systems.[7] In this figure, the amount of power per kilogram, or power density, that can be delivered is displayed on the x-axis. The amount of energy per kilogram, or energy density, is displayed on the y-axis. The lines in the plot represent typical constant discharge times. The discharge times from Table 4.1 are shown in Figure 4.13 to indicate where they are located in the Ragone plot. Given the requirements stated in this chapter, energy storage systems with relatively high power density that can be charged and discharged within seconds, i.e. flywheels, supercapacitors and superconducting magnetic energy storage, are best suited for the application considered in this research. Out of these three types of energy storage superconducting magnetic energy storage is not considered, however, due to the cooling requirements and magnetic fields associated with this technology.[57]

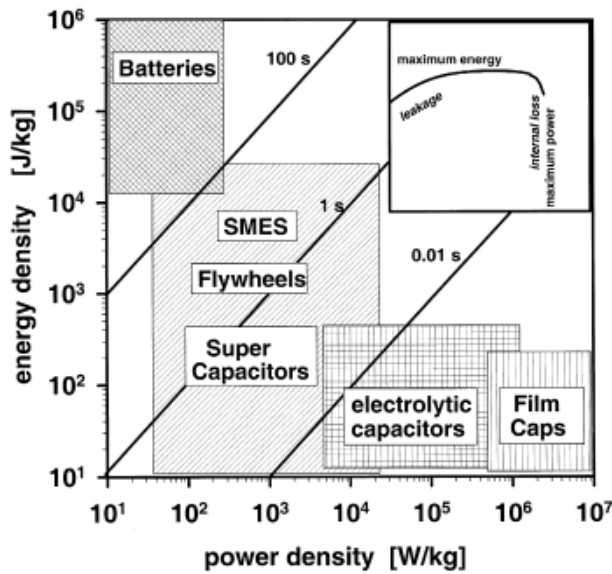


Figure 4.12: Ragone plot[7]

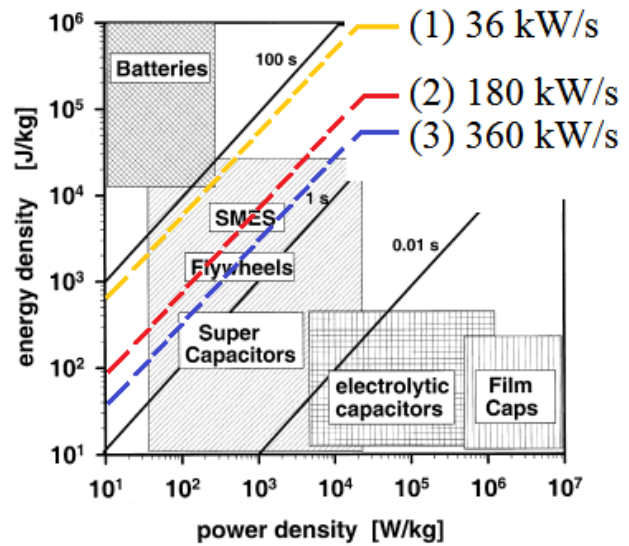


Figure 4.13: Ragone plot with loading limits

## 4.3 Supercapacitors

Supercapacitors, sometimes referred to as ultracapacitors or electric double-layer capacitors, are high capacity capacitors. The use of capacitors has been commonly limited to applications requiring low energy levels due to their low capacitance. Developments in manufacturing techniques have made it possible to produce capacitors capable of storing more energy in the form of electric charge. These capacitors are called supercapacitors. Supercapacitors bridge the gap between batteries and conventional capacitors in the sense that they are able to store more energy than capacitors and deliver more power than batteries. Figure 4.14 shows a schematic of a conventional capacitor. The capacitor consists of two conducting electrodes separated by an insulating dielectric material. The applied voltage results in opposite charges on the surface of the electrodes, which are separated by dielectric material. The electric field that is produced this way allows the capacitor to store energy.[21]

The process described above is completely reversible, resulting in a high efficiency and a large number of charge and discharge cycles. The ability to store electric charge is referred to a capacitance, which is defined as:

$$C = \epsilon_0 \epsilon_r \frac{A}{D} \quad (4.5)$$

Where

$C$  is the capacitance in  $F$

$\epsilon_0$  is the dielectric constant of free space

$\epsilon_r$  is the dielectric constant of the insulating material between the electrodes

$A$  is the surface area of the electrodes in  $m^2$

$D$  is the distance between the electrodes in  $m$

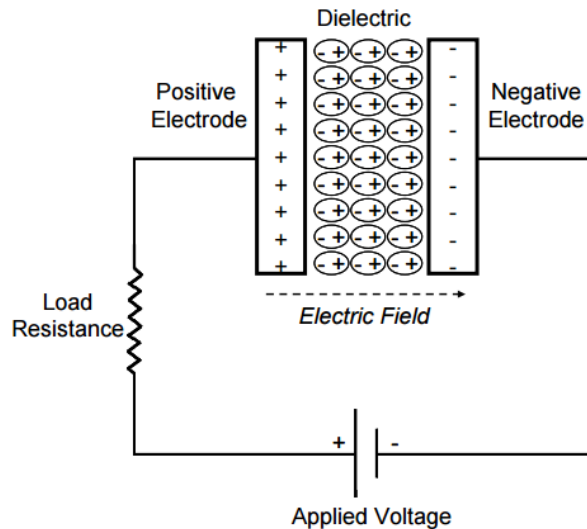


Figure 4.14: Schematic of a conventional capacitor[21]

Supercapacitors are governed by the same principles as conventional capacitors. What separates supercapacitors from conventional capacitors is that the electrodes of supercapacitors have a much higher surface area and much thinner dielectrics, decreasing the distance between the electrodes. This leads to an increase in capacitance and therefore an increase in energy that can be stored, as can be seen in Equation 4.5. More details on supercapacitors will be given in Section 5.2.1.

### 4.3.1 Power and energy

A supercapacitor ESS has a modular design, where a single module consists of several supercapacitor cells placed in series. The amount of supercapacitor cells per module depends on the desired rated voltage per module. Multiple modules can be placed in series to increase the rated voltage  $U_r$  to the desired voltage of the total ESS. The value of  $U_r$  is often dependent on the DC link voltage the supercapacitor ESS is connected to. To increase the power output and storage capacity, branches of supercapacitor modules can be placed in parallel. Furthermore, by placing branches in parallel, the current per branch is reduced, which will be further discussed in Section 4.3.2. Figure 4.15 gives an overview of how a supercapacitor ESS is built up. In the figure,  $M_1$  to  $M_n$  denote the supercapacitor modules.  $B_1$  to  $B_n$  denote the branches.

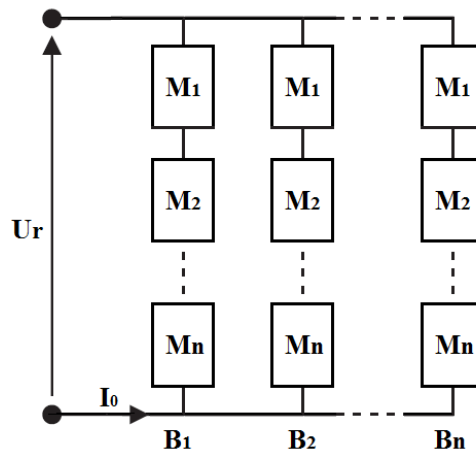


Figure 4.15: Supercapacitor ESS configuration

The power that can be delivered by a supercapacitor is determined by the terminal voltage. This voltage varies depending on the state-of-charge of the supercapacitor, with maximum voltage at full charge. Figure 4.16 shows the supercapacitor voltage over time when charging and discharging at constant current. The small jump in voltage results from the internal resistance of the supercapacitor. This will be further discussed in Chapter 5.2.1.

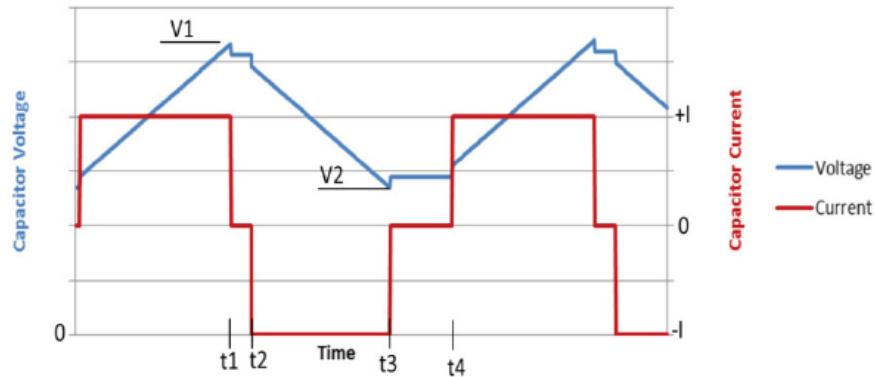


Figure 4.16: Supercapacitor voltage at constant current (dis)charging[40]

### 4.3.2 Losses and constraints

Figure 4.17 gives a schematic overview of supercapacitor ESS components and their respective efficiencies. The predominant loss in supercapacitors results from the internal resistance. Current flowing through the resistance causes energy loss in the form of Ohmic heating. The amount of energy loss is determined by the square of the current magnitude, since Ohmic heating is defined by  $I^2R$ . This means that supercapacitor efficiency increases when charging and discharging currents are reduced. The current per supercapacitor module can be reduced without loss of power output by placing modules in parallel. Often a maximum continuous current and maximum peak current are defined for the supercapacitors. These quantities are defined to limit heating of the supercapacitor, which results in an increase in lifetime. Depending on the rate at which the supercapacitor is (dis)charged the efficiency ranges from 87.5% to 99%, where the latter is the value for very low currents.

The power electronics converter, which converts the supercapacitor ESS to the proper DC bus voltage, is the next cause of energy loss. The DC/DC converter is assumed to have an efficiency ranging from 95% to 98%, depending on the delivered power.[1] The final cause of loss that is considered is the leakage current. The leakage current is only a few  $mA$  and the total amount of loss is dependent on time, and is therefore not expressed as an efficiency.[40]

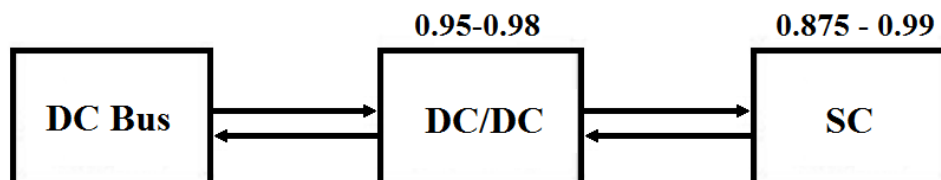


Figure 4.17: Supercapacitor efficiencies

The total maximum and minimum efficiency for a full charge and discharge cycle are then given by:

Maximum cycle efficiency:  $\eta_{cyc,min}^{SC} = 0.98 \cdot 0.99 \cdot 0.99 \cdot 0.98 = 0.94$ .

Minimum cycle efficiency:  $\eta_{cyc,max}^{SC} = 0.95 \cdot 0.88 \cdot 0.88 \cdot 0.95 = 0.70$ .

## 4.4 Flywheel energy storage

In flywheel energy storage systems energy is stored as kinetic energy in an accelerated rotor. The mechanically stored energy is transferred from and to the flywheel by an electric machine. While the concept of storing energy in a rotating mass has been used for decades, modern flywheel systems are able to store far greater amounts of energy due to much higher rotational speeds of up to 50000 rpm.[31] Typically, modern flywheel energy storage systems are comprised of a high-strength rotor attached to a permanent magnet machine.[4] The flywheel spins in a vacuum enclosure to reduce air friction. The flywheel is suspended using low friction bearings. Figure 4.18 shows a schematic overview of a flywheel energy storage system. A power electronics converter is connected to the electric machine ensure the correct power output. More details on flywheels will be given in Section 5.2.2.

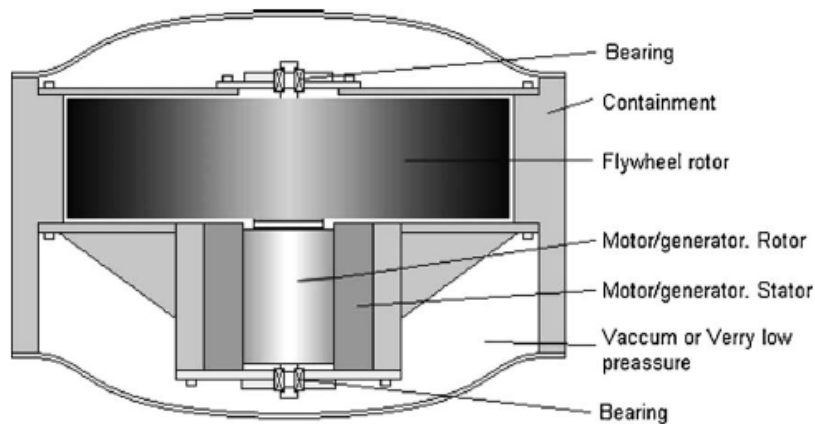


Figure 4.18: Schematic of flywheel components[4]

### 4.4.1 Power and energy

The configuration of the flywheel ESS is more simple than for the supercapacitors. The flywheel ESS consists of several parallel modules. Each module has an identical power output and storage capacity. All modules combined add up to the total power output and storage capacity. Figure 4.19 gives an overview of how a flywheel ESS is built up. In the figure,  $M_1$  to  $M_n$  denote the individual flywheel modules.

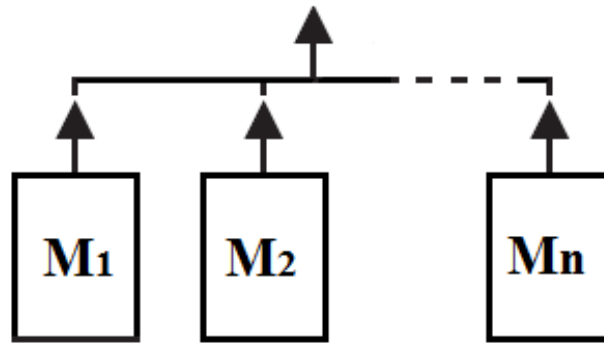


Figure 4.19: Flywheel ESS configuration

#### 4.4.2 Losses and constraints

Figure 4.20 gives a schematic overview of flywheel ESS components and their respective efficiencies. Like with the supercapacitor, the power electronics converter used to connect the flywheel ESS to the DC bus of the frequency drives is the first cause of energy loss. The efficiency for the DC/AC converter is also assumed to have an efficiency between 95% and 98%, depending on the delivered power. The permanent magnet motor connected to the flywheel is assumed to have an efficiency of 97%. [11] The self-discharge of the flywheel is the predominant cause of energy loss. However, because this dependent on time and the rotational speed of the flywheel this is not expressed as an efficiency here. The self-discharge of the flywheel is expressed as a power loss dependent on the SOC and will be further discussed in Section 5.2.2.

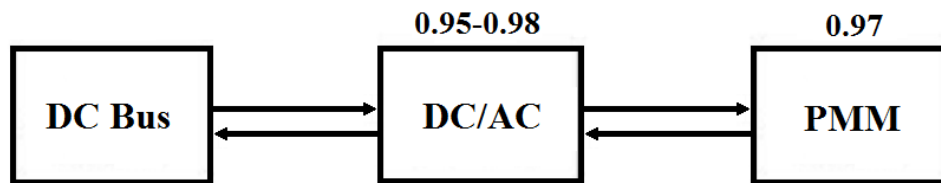


Figure 4.20: Flywheel efficiencies

The total maximum and minimum efficiency for a full charge and discharge cycle are then given by:

$$\text{Maximum cycle efficiency: } \eta_{cyc,max}^{FW} = 0.98 \cdot 0.97 \cdot 0.97 \cdot 0.98 = 0.90.$$

$$\text{Minimum cycle efficiency: } \eta_{cyc,min}^{FW} = 0.95 \cdot 0.97 \cdot 0.97 \cdot 0.95 = 0.85.$$

## 4.5 Cycle life

Another important aspect to consider when selecting energy storage techniques is their projected lifetime. Typically, the lifetime is expressed in the number of cycles where the energy storage system is fully discharged and fully charged. In contrast to batteries, the lifetime of both supercapacitors and flywheel energy storage systems is not affected by the degree to which they are (dis)charged, referred to as the depth-of-discharge (DOD). For flywheels there is no degradation over time and, as stated earlier, cycle life is not directly related to DOD. The critical aspect in high-speed flywheels is the material fatigue resulting from cyclic loading. Due to these aging characteristics, flywheel energy storage cycle lifetimes are in excess of one million cycles. [24]

While the cycle lifetime is not influenced by the DOD, there are some aging effects present for supercapacitors. The internal resistance of supercapacitors can increase over time, reducing power output and causing more heating. Secondly, the capacitance of the supercapacitor becomes lower over time due to capacitance retention. Both these effects are significantly affected by high temperatures, which is why it is important to reduce the operating temperature to increase the lifetime.[59] The cycle lifetime of supercapacitors is often claimed to be in the order of magnitude of one million cycles by manufacturers. However, many results of documented cycle tests claim to reach a maximum of 150000 cycles, while other research claims over ten million cycles.[40][44] Given the wide spread in the cycle lifetime of supercapacitors found in literature, the number of cycles stated by the manufacturer will be used to estimate the lifetime.

When considering the number of lifetime cycles stated here and applying them to the same data as shown in Table 4.1, lifetime estimation results as shown in Table 4.2 are found. It should be noted here that these values are rough estimations where non-stop dredging operation is assumed. Furthermore, a single cycle is defined as one instance of charging and one instance of discharging and no distinction is made between large and small power peaks, making it a very conservative estimation.

Table 4.2: Average number of ESS cycles for January 2016 data

Maximum load increase	Average cycles per hour	Projected lifetime
36 kW/s	1 cycles/hour	114 years
180 kW/s	13 cycles/hour	8.8 years
360 kW/s	164 cycles/hour	0.7 years

## 4.6 Power management

The power management system (PMS) determines when power is supplied by or to the energy storage system based on the current power demand and the amount of power delivered by the generators. The PMS has the following functions:

- **Deliver power on increasing electric load.** When the increase in electric load on the generators exceeds the limit, the ESS delivers power according to Equation 4.2. Consequently, the mechanical load on the diesel engines is reduced.
- **Consume power on decreasing electric load.** When the decrease in electric load on the generators exceeds the limit, the ESS consumes power by charging according to Equation 4.3. Consequently, the mechanical load on the diesel engine is reduced more slowly.
- **Consume power below minimum engine load.** When the total mechanical load on the diesel engines drops below a certain value, the electric load is kept at a predefined minimum to charge the ESS.

An important factor in the PMS is the response time of the ESS. The response time is given by the amount of time that is required to go from no discharge to discharge at rated power. The response time is limited by the power electronics converter and the ESS itself. For the power electronic converter (PEC), the response to load changes is instantaneous. For both supercapacitors and flywheels the response time is in the order of milliseconds.[13][36] The sampling rate of the cutter data that is used is 5 Hz, so the time steps are 200 ms. Because the smallest data time step exceeds the response time of the ESS, switching in the PMS is taken as instantaneous. Table 4.3 shows the inputs that are used to assess which action is taken by the PMS.

Table 4.3: Power management system inputs

General inputs	Supercapacitor specific inputs	Flywheel specific inputs
Current power demand	Rated voltage	Flywheel moment of inertia
Transient power limit	Current voltage	Max. rotational speed
Current diesel power	Capacitance	Min. rotational speed
Nominal diesel engine power	Series resistance	Current rotational speed
ESS stored energy		Maximum power
Minimum ESS SOC		

## 4.7 Performance evaluation criteria

In order to analyze the performance of the proposed CSD drivelines criteria need to be defined on which the evaluation is based. Considering the research objective stated in Chapter 1 the predominant criterion would be the capability of reducing the mechanical load on the internal combustion engines. Other criteria to consider are the fuel consumption, ESS cycle life, and the cost of the ESS. These evaluation criteria are discussed below.

### 4.7.1 Transient loads

Although research on the effect on engine wear caused by transient load is not conclusive, it is suspected that transient loads cause an increased wear of diesel engines.[58] Figure 4.21 shows the series of events that result from a sudden increase in load. The increase in load results in a torque deficit that needs to be compensated for. As a result the engine speed is lowered and more fuel is injected. The air-to-fuel ratio is lowered because it takes some time for the turbocharger to supply the required amount of air. This has some negative effects on the combustion process, like incomplete combustion. Soot formation on the cylinder liner results from incomplete combustion which is assumed to increase engine wear.[54][58] The actual wear is difficult to quantify, however. The performance of the proposed CSD drivelines with respect to this criterion will therefore be evaluated on the degree to which the transient load limit is exceeded.

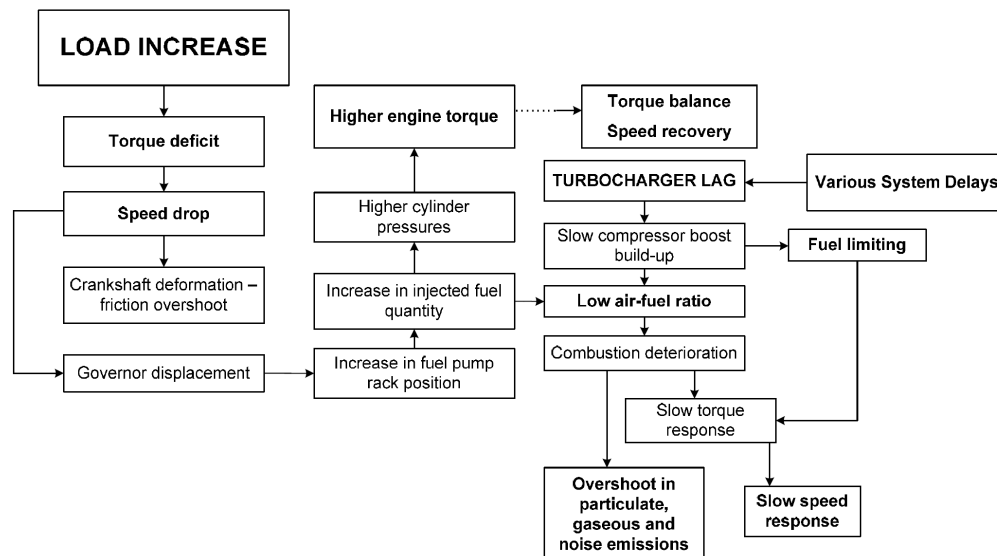


Figure 4.21: Series of events after a step load increase of a turbocharged diesel engine[48]

### 4.7.2 Fuel consumption

An important aspect to consider when determining the fuel consumption is the effect of transient loads in the diesel engines. The general assumption is that during acceleration fuel consumption is increased, but previous research showed that it is difficult to quantify this effect.[49] Comparison of a static and dynamic diesel engine model showed that transient loads have an effect of less than 1% on fuel consumption.[37] Following this research a more extensive analysis on the effect of transient loads has been conducted. Here, it is concluded that for turbocharged four stroke diesel engines in generator mode fuel consumption will not increase as a result of transient loads, provided there is a sufficiently high air excess ratio.[18]

Since the engine limits stated at the beginning of this chapter are mainly determined by the air excess ratio it is assumed that there is always a sufficiently high air excess ratio. Therefore, it is assumed that the fuel consumption can be estimated by the steady-state values provided by the engine manufacturer. Because the load on the internal combustion engines changes as a result of alterations to the CSD driveline this fuel consumption is expected to be different for each configuration. Due to the lack of fuel consumption data on the original CSD driveline only a comparison in simulated fuel consumption can be made. Performance in terms of fuel consumption can then be compared relative to a benchmark simulation of the original driveline.

### 4.7.3 ESS cycle life

The approximation for the cycle life given in Section 4.5 is based on one instance of discharging and one instance of charging, regardless of the amount of power and energy delivered. The amount of lifetime cycles is independent of the degree to which the ESS is charged and discharged. It is therefore considered to be more accurate to assess the total amount of energy taken up and supplied by the ESS during simulations to get a better approximation of the ESS cycle life. The total cycle lifetime that is considered is unchanged and is taken as one million cycles for both ESS.[40][12]

### 4.7.4 Cost analysis

The determination of the initial cost of the energy storage system is based on the cost per unit power and cost per unit energy storage capacity. The major components that determine the cost of the energy storage system are displayed in Figure 4.22.

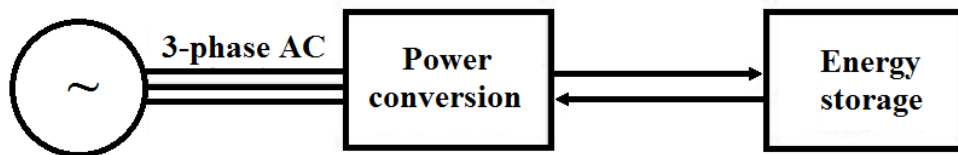


Figure 4.22: Major cost components in an energy storage system[53]

Cost estimates for supercapacitor modules are available, so a fairly accurate estimation of the total cost of a supercapacitor energy storage system can be made.[56] Unfortunately, manufacturers of flywheel modules were unable to provide such an estimate. There are, however, ranges for cost per  $kW$  and cost per  $kWh$  available in literature.[14][36] An attempt has been made use these values to make a good assumption of the total cost, so that the total cost can be determined by Equation 4.6:[53]

$$Cost_{total}(\text{€}) = UnitCost_{pcs}(\text{€/kW}) \cdot P(\text{kW}) + UnitCost_{storage}(\text{€/kWh}) \cdot E(\text{kWh}) \quad (4.6)$$

Where

$UnitCost_{pcs}$  is the cost per  $kW$  that can be delivered

$UnitCost_{storage}$  is the cost per  $kWh$  that can be stored

$P$  is the maximum power that can be delivered

$E$  is the amount of usable energy that can be stored

Due to the wide spread between the minimum and maximum values of these costs a comparison is made with the available estimates for the supercapacitor modules. Based on this comparison, a value of 35 €/kW is assumed for the cost per amount of power delivered. It should be noted here that this value has been converted to represent peak power, where the costs found in the literature are based on continuous power. It is assumed that the cost per kW is slightly higher for the flywheel than for supercapacitor modules, which can also be concluded from the literature. A similar approach has been used to determine values for the cost per kWh that can be stored. The values are summarized in Table 4.4.

Table 4.4: Values to determine energy storage module cost

Supercapacitor $UnitCost_{pcs}$	35 €/kW
Supercapacitor $UnitCost_{storage}$	7500 €/kWh
Flywheel $UnitCost_{pcs}$	50 €/kW
Flywheel $UnitCost_{storage}$	4000 €/kWh
Supercapacitor module	5825 €
Flywheel module	31000 €

#### 4.7.5 Size and weight

Table 4.5 shows the dimensions and weight of both ESS considered. For the supercapacitor module it is assumed that the dimensions are proportional to the number of supercapacitor cells in the module. Furthermore, the power electronics converter for the flywheel ESS is included in the size and weight.

Table 4.5: ESS dimensions and weight[2][22]

ESS type	Dimensions, l x h x d [m]	Weight [kg]
Supercapacitor module	0.550 x 0.436 x 0.167	31
Supercapacitor DC/DC converter	0.502 x 0.477 x 0.203	22
Flywheel module	0.780 x 0.780 x 0.450	375

#### 4.7.6 Fuel specifications

The main diesel engines are assumed to use marine diesel oil (MDO) as fuel. For the dual fuel engines LNG with a MN of 80 is assumed as fuel. The gas quality as described in Section 3.4.4 is not considered here. Table 4.6 shows the prices and specifications assumed for fuel. The MDO price is based on prices in Rotterdam in January 2017.[45] Prices for LNG are often represented without the cost for liquefaction and transportation.[10] Prices at which the LNG is delivered on board are often expressed as fraction of current diesel oil prices.[6] When considering average prices, the price for LNG is assumed as 0.7 times the MDO prices.

Table 4.6: Fuel prices

Fuel type	Price €/1000 kg	LHV [MJ/kg]	Price €/GJ
Marine diesel oil	460	42.48	10.83
Liquefied natural gas (MN80)	322	49.62	6.49

### 4.7.7 Network voltage and frequency

The requirements regarding allowed voltage and frequency variations are given in Section 2.4. However, considering the line from the classification society quoted below, this is not an issue for the vessel considered in the research because the correct operation of the electrical devices has been proven.[61]

Bureau Veritas, Rules for the Classification of Steel Ships, Section 2.4.3:

*"Higher values for the harmonic content (e.g. in electric propulsion plant systems) may be accepted on the basis of correct operation of all electrical devices."*

The addition of an ESS is expected to reduce the load variations on the power generation system, which consequently cause the variation in voltage and network frequency to drop. Therefore, it is assumed that correct operation of electrical devices is unchanged.

# Chapter 5

## Modeling

### 5.1 Modeling principles

#### 5.1.1 Per unit representation

For computational simplicity, the per unit system is often used to normalize variables in power system analysis. Instead of using physical units all system quantities are expressed as dimensionless ratios as follows:

$$\text{quantity in per unit} = \frac{\text{actual quantity}}{\text{base value of quantity}}$$

In the performed simulations all system quantities are also expressed in per unit form. This means that, for instance, the measured motor parameters will have to be divided by some base value before they can be used for simulations. The nominal apparent power and nominal voltage of the induction motor have been chosen as basis for the per unit system. The nominal apparent power is determined by:

$$S_{nom} = \frac{P_{nom}}{\cos\phi} [VA]$$

So the base values of the per unit system are defined as  $S_{base} = S_{nom}$  and  $U_{base} = U_{nom}$ . The base values for the current and impedance follow from these values:

$$I_{base} = \frac{S_{base}}{\sqrt{3} \cdot U_{base}} [A]$$

$$Z_{base} = \frac{U_{base}}{\sqrt{3} \cdot I_{base}} [\Omega]$$

All other quantities are derived in a similar way. Table 5.1 gives an overview of all used per unit quantities.

Table 5.1: Base values used to convert SI unit to per unit quantity

Base quantity	Value	SI Unit	Base quantity	Value	SI Unit
$S_{base}$	$S_{nom}$	$VA$	$\Psi_{base}$	$L_{base} \cdot I_{base}$	$V \cdot s$
$U_{base}$	$U_{nom}$	$V$	$\omega_{e,base}$	$2\pi \cdot f_{nom}$	$\frac{rad}{s}$
$f_{base}$	$f_{nom}$	$Hz$	$L_{base}$	$\frac{Z_{base}}{\omega_{e,base}}$	$H$
$I_{base}$	$\frac{S_{base}}{\sqrt{3} \cdot U_{base}}$	$A$	$\omega_{m,base}$	$\frac{2}{p} \cdot \omega_{e,base}$	$\frac{rad}{s}$
$Z_{base}$	$\frac{U_{base}}{\sqrt{3} \cdot I_{base}}$	$\Omega$	$\tau_{base}$	$\frac{S_{base}}{\omega_{m,base}}$	$Nm$

### 5.1.2 DQ-reference frame

Most power systems have an electrical frequency of 50 or 60  $Hz$ . As a result, a lot of cosine and sine functions are needed to describe, for instance, transfer between rotor and stator phenomena. Furthermore, due to inductance terms varying with the electrical frequency computational complexity is increased. Since only the amplitude and frequency of voltages, currents et cetera are relevant and not the shape of the sinusoidal signals themselves, a dq-reference frame is used to model the power system quantities. The direct-quadrature-zero (dq0) transformation allows the expression of a three-phase AC signal in a dq-reference frame.[62] The transformation from  $abc$  phase variables to the dq0 variables is given by Equation 5.1:[35]

$$\begin{bmatrix} x_d \\ x_q \\ x_0 \end{bmatrix} = \frac{2}{3} \begin{bmatrix} \cos\theta & \cos(\theta - \frac{2\pi}{3}) & \cos(\theta + \frac{2\pi}{3}) \\ -\sin\theta & \sin(\theta - \frac{2\pi}{3}) & -\sin(\theta + \frac{2\pi}{3}) \\ \frac{1}{2} & \frac{1}{2} & \frac{1}{2} \end{bmatrix} \begin{bmatrix} x_a \\ x_b \\ x_c \end{bmatrix} \quad (5.1)$$

Where

$a, b, c$  are the phase variables of a three-phase system

$x_i$  can represent voltages, currents, or fluxes

Balanced conditions are assumed, meaning all lines of the three-phase system share equivalent loads and each line will produce equal voltage and current magnitudes at phase angles equally spaced from each other. For balanced conditions  $x_a + x_b + x_c = 0$ . Therefore, the zero sequence component  $x_0$  is also zero. Equation 5.1 can therefore be simplified to:

$$\begin{bmatrix} x_d \\ x_q \end{bmatrix} = \frac{2}{3} \begin{bmatrix} \cos\theta & \cos(\theta - \frac{2\pi}{3}) & \cos(\theta + \frac{2\pi}{3}) \\ -\sin\theta & \sin(\theta - \frac{2\pi}{3}) & -\sin(\theta + \frac{2\pi}{3}) \end{bmatrix} \begin{bmatrix} x_a \\ x_b \\ x_c \end{bmatrix} \quad (5.2)$$

The active  $P$  and reactive power  $Q$  can be extracted from the dq-values by Equation 5.3:[35]

$$P = \frac{2}{3}(u_d \cdot i_d + u_q \cdot i_q) \cdot S_{base} \quad \text{and} \quad Q = \frac{2}{3}(u_q \cdot i_d - u_d \cdot i_q) \cdot S_{base} \quad (5.3)$$

More details on the dq0 transformation can be found in Appendix A.

## 5.2 Energy storage system models

### 5.2.1 Supercapacitor model

#### Description

The supercapacitor is modeled using the standard R-C equivalent circuit, as shown in figure 5.1. This circuit is composed of equivalent series resistance  $R_{ESR}$  and a capacitance  $C$ . This model represents the energetic behavior of the supercapacitor and its storing capacity and is usually used to model global management of embedded energy.[9] The R-C model is associated with a charge and discharge test at constant current. Figure 5.2 shows the change in voltage during discharge at constant current. The amount of energy that is stored in a supercapacitor is given by:

$$E_{sc} = \frac{1}{2}CU_0^2 \quad (5.4)$$

Where

$U_0$  is the supercapacitor voltage

$C$  is the capacitance

Not all stored energy can be extracted, however, since the voltage is never reduced to zero. Typically, supercapacitors are discharged to a minimum voltage  $U_{min}$ , equaling half the rated voltage  $U_r$ . [40]

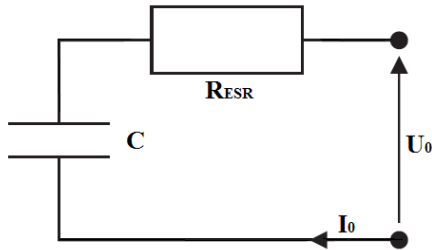


Figure 5.1: R-C equivalent circuit of a supercapacitor.

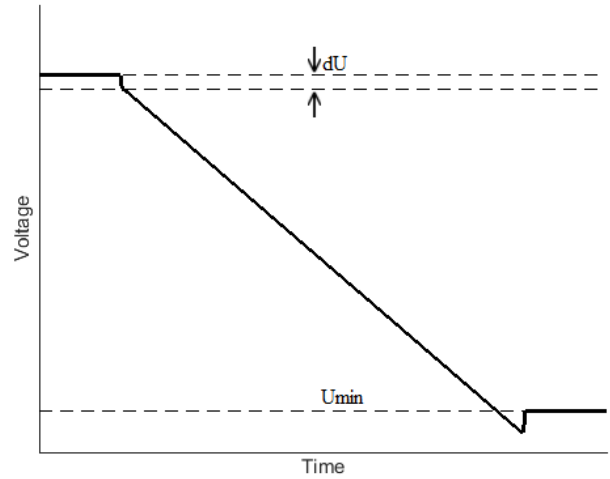


Figure 5.2: Supercapacitor voltage drop.

Because the minimum voltage is higher than zero the effective stored energy is lower than the total amount of energy stored in the supercapacitor. The effective stored energy is given by:

$$E_{sc,eff} = \frac{1}{2}C(U_r^2 - U_{min}^2) \quad (5.5)$$

From equation 5.5 it can be seen that when discharging to half the rated voltage, which is the minimum voltage, 75% of the stored energy can be extracted. For easier determination of the amount of stored energy the state-of-charge (SOC) is used, which is defined by Equation 5.6. Keeping  $U_{min}$  in consideration, this means that the SOC can never be lower than 25%.

$$SOC = \frac{\frac{1}{2}CU_0^2}{E_{sc,max}} \cdot 100 \% \quad (5.6)$$

During the discharge as shown in Figure 5.2 the capacitance of the supercapacitor can be obtained through the tangent of the voltage:

$$C = I_d \cdot \frac{\Delta t}{\Delta U}$$

The small drop in voltage at the start of discharge results from the difference in voltage caused by  $R_{ESR}$  and is defined by Equation 5.7. The equivalent series resistance (ESR) is also responsible for power loss during charging and discharging of the supercapacitor. In Section 4.5 the increase of the ESR over time is described. Since relative short simulations are performed, this effect will not be considered and the ESR will be taken as a constant value. The maximum allowed current during charging and discharging is considered during

simulations.

$$dU = R_{ESR} \cdot I_0 \quad (5.7)$$

### Model parameters

The relation between the supercapacitor's voltage and state of charge is then given by:

$$U = \sqrt{\frac{2 \cdot SOC \cdot E_{sc,max}}{C}} \quad (5.8)$$

According to [26], the maximum currents during charging and discharging are equal. The maximum power during charging and discharging is then given by:

$$P_{max} = \frac{U_0^2}{8 \cdot R_{ESR}} \quad (5.9)$$

The power loss resulting from  $R_{ESR}$  is given by:

$$P_{Loss} = I_0^2 \cdot R_{ESR} \quad (5.10)$$

### Specifications

For the supercapacitors the BCAP3000 P270 K04 by manufacturer Maxwell have been selected. Some relevant specifications for these supercapacitors are displayed in Table 5.2. The supercapacitors are placed in modules of 42 to 48 cells. Multiple modules can be placed in parallel or series to get the desired output.

Table 5.2: Maxwell BCAP3000 P270 K04 Supercapacitor specifications[40]

<b>Capacitance <math>C</math></b>	75 F
<b>Rated voltage <math>U_r</math></b>	2.7 V
<b>Equivalent series resistance <math>R_{ESR}</math></b>	0.29 mΩ
<b>Maximum peak current <math>I_{peak}</math></b>	1900 A
<b>Maximum continuous current <math>I_{cont}</math></b>	210 A <sub>rms</sub>
<b>Leakage current <math>I_L</math></b>	5.2 mA
<b>Module (48 cells) weight</b>	33 kg
<b>Module (48 cells) width</b>	600 mm
<b>Module (48 cells) depth</b>	436 mm
<b>Module (48 cells) height</b>	167 mm

The maximum voltage produced by each branch of supercapacitor modules in series is based on the average rectified voltage in the DC-link of the frequency drive. The average voltage for an ideal rectifier is given by:[47]

$$U_{ia} = \frac{3 \cdot \sqrt{2} \cdot U_{line}}{\pi} \quad (5.11)$$

Where  $U_{line}$  is the line voltage of 690V produced by the generators.

When placing 8 modules of 44 cells in series the following rated voltage for each branch of supercapacitor modules are obtained:

$$\text{Rated voltage } U_r = 8 \text{ modules} \cdot 44 \text{ cells} \cdot 2.7 \text{ V} = 950.4 \text{ V} \quad (5.12)$$

The equivalent series resistance and capacitance for each branch are then given by:

$$R_{ESR} = 8 \text{ modules} \cdot 44 \text{ cells} \cdot 0.29 \text{ m}\Omega = 102.08 \text{ m}\Omega \quad (5.13)$$

$$C = \frac{3000 \text{ F}}{8 \text{ modules} \cdot 44 \text{ cells}} = 8.523 \text{ F} \quad (5.14)$$

Assuming the minimum voltage is half the rated voltage, the amount of usable energy stored per branch and discharge power per branch are given by Equation 5.15 and Equation 5.16:

$$E_{eff,branch} = \frac{1}{2} \cdot C \cdot (U_r^2 - \left(\frac{U_r}{2}\right)^2) = 2.887 \text{ MJ} \quad (5.15)$$

$$P_{d,branch} = \frac{U_r^2}{8 \cdot R_{ESR}} = 1.106 \text{ MW} \quad (5.16)$$

Several branches of supercapacitor modules can be placed in parallel to get the desired power output and to limit the current per branch.

### Model verification

The model of the supercapacitor has been implemented as described in the previous sections. For verification of the model the specifications from Table 5.2 have been used. To test the model a simulation is conducted where an initially fully charged supercapacitor module consisting of 48 cells is discharged to minimum charge and again charged to full charge at constant current. Figure 5.3 and Figure 5.4 show the change of the state-of-charge and the power during charging and discharging. Note that the amount of power the supercapacitors can deliver is determined by the voltage. Therefore, at constant current the power decreases depending on the state-of-charge as can be seen in Figure 5.4.

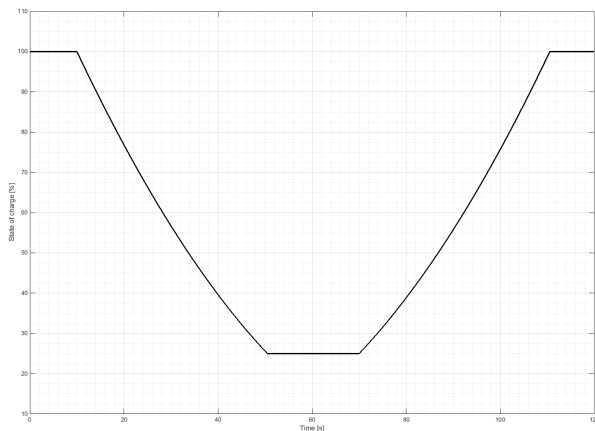


Figure 5.3: Supercapacitor state-of-charge of a full charge/discharge cycle

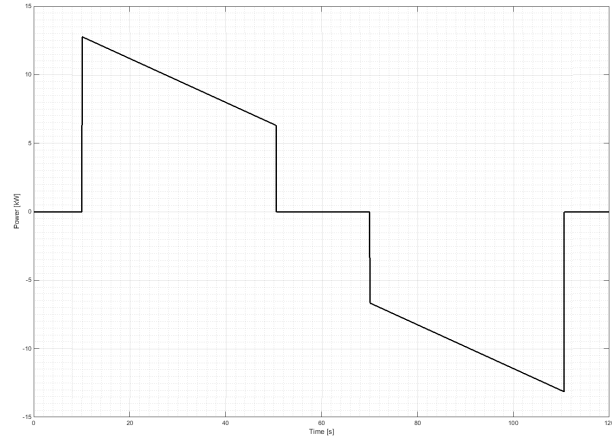


Figure 5.4: Supercapacitor charge/discharge power at constant current

The supercapacitor voltage is shown in Figure 5.5 when discharging at a constant current of 100 A to the minimum allowed voltage and consecutively charging at a constant current of 100 A to the rated voltage.

The small jump in voltage resulting from the equivalent series resistance  $R_{ESR}$  at the start of (dis)charge is clearly visible in the figure, and is the main cause of energy loss in the supercapacitor module, especially at high currents. This result follows the theoretical description given in Section 4.3.1. Furthermore, the figure shows the same behaviour as given by the manufacturer.[40] Because of the timescale in the figures shown here, the leakage current which causes self-discharge of the supercapacitors is not visible, as this can only be observed after a few hours. More details on the model of the supercapacitor can be found in Appendix D.3.1.

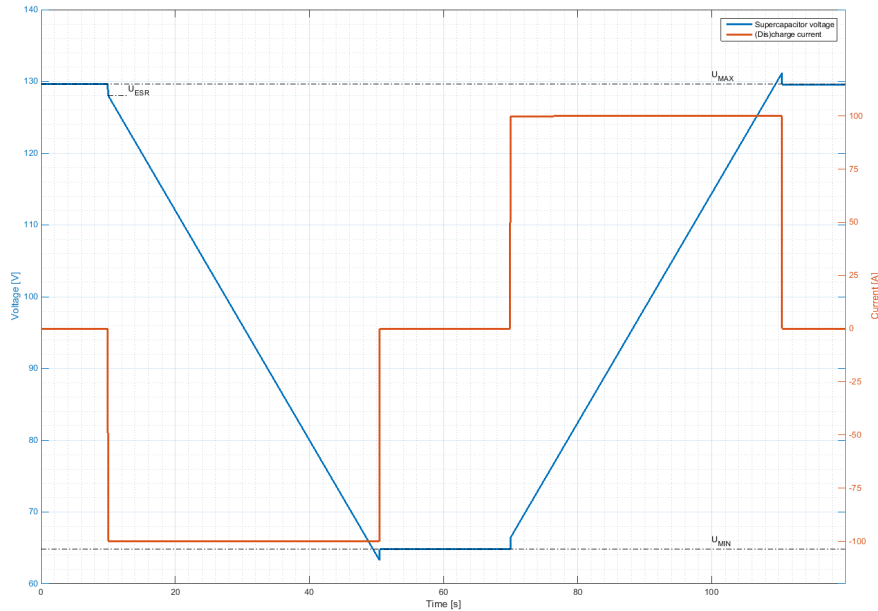


Figure 5.5: Supercapacitor voltage when (dis)charging at constant current

## 5.2.2 Flywheel model

### Description

Flywheels are used to store energy in the form of kinetic energy in a rotating mass. The amount of energy that is stored in a flywheel is given by:

$$E_{fw} = \frac{1}{2} J \omega^2 \quad (5.17)$$

From Equation 5.17 it is clear that the speed at which the flywheel rotates is more important than the mass, since moment of inertia  $J$  is proportional to the flywheel's mass. Permanent magnet synchronous machines are typically used for flywheel energy storage systems because of their high power density and high efficiency characteristics. The rotational speed of the flywheel is never reduced to zero. Therefore, the total amount of energy stored in the flywheel can not be used. The effective amount of stored energy that can be used is given by:

$$E_{fw.eff} = \frac{1}{2} J (\omega_{max}^2 - \omega_{min}^2) \quad (5.18)$$

In [57], the ratio between the maximum and minimum rotational speed is said to be 0.2. This would mean that 96% of the total amount of stored energy is usable. In practice manufacturers choose a higher value for the minimum rotational speed. The discharge power of a flywheel energy storage system is determined by

the torque of the electric machine:

$$P_d = M_{em} \cdot \omega_m \quad (5.19)$$

When a very low minimum rotational speed is allowed the torque developed by the electric machine needs to be very high to be able to deliver the required amount of power. Therefore, the minimum rotational speed is often chosen to be half the maximum rotational speed so the size and weight of the selected electric machine can be reduced.[57] With this value up to 75% of the stored energy can be extracted from the flywheel.

### Flywheel self-discharge

The main cause of energy loss in flywheel energy storage results from flywheel self-discharge. Self-discharge of the flywheel is caused by friction in the bearings and from air friction on the flywheel itself. In many cases the flywheel rotates in a vacuum to minimize air friction. The total energy loss is at least twenty percent per hour, and is assumed to exponentially decay, depending on the rotational speed of the flywheel.[15][32] The self-discharge power  $P_{sd}$  is therefore assumed to be described by:

$$P_{sd} = \frac{dE_{fw}}{dt} = \lambda E_{fw,max} e^{\lambda t} \quad (5.20)$$

Where

$$t = \left( \frac{SOC - 1}{\kappa} \right) \quad (5.21)$$

And

$E_{fw}$  is the stored energy

$E_{fw,max}$  is the maximum amount of stored energy

$SOC$  is the state-of-charge

$\lambda$  is a constant and determines the rate of decay, given by  $\lambda = \ln(1 - \Delta E)/\Delta t$

$\kappa$  is a constant that is determined by the percentage of energy lost for a certain period of time and is given by  $\kappa = -\Delta E/\Delta t$

Twenty percent energy lost in one hour results in values for  $\lambda$  and  $\kappa$  of  $\lambda = -6.1984 \cdot 10^{-5}$  and  $\kappa = -5.556 \cdot 10^{-5}$ , respectively. When applying Equation 5.20 to these value it can be seen that this results in a twenty percent energy loss in one hour:

$$\int_{0.8}^1 \lambda E_{fw,max} e^{\lambda \left( \frac{SOC-1}{\kappa} \right)} d(SOC) = -\frac{E_{fw,max}}{5} \quad (5.22)$$

Plotting the self-discharge power as a function of the state-of-charge results in Figure 5.6. It can be seen that Equation 5.20 does not perfectly describe the power loss because the amount of self-discharge is not zero when the flywheel is stationary. This is due to the fact that the considered friction is increasingly present at higher speeds. However, since the state-of-charge is never below twenty-five percent, it is therefore assumed that Equation 5.20 describes the flywheel's self-discharge well enough.

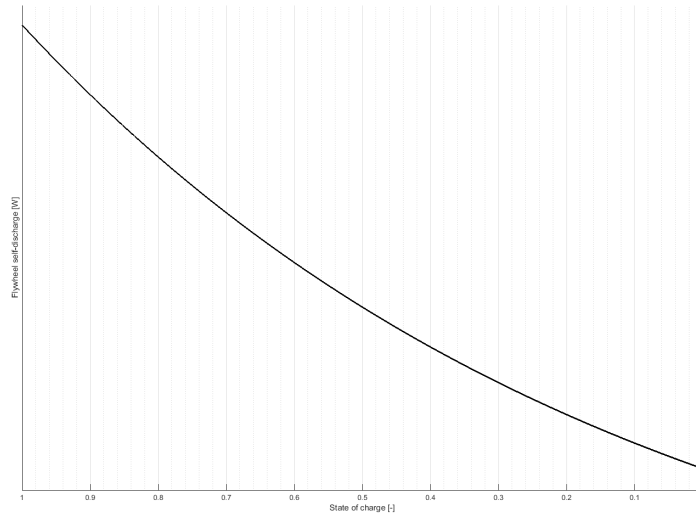


Figure 5.6: Flywheel self-discharge as a function of state-of-charge

## Specifications

For the flywheel energy storage system the EMAFER RxV-II by manufacturer CCM has been selected. These modules are used in heavy-duty vehicles and are considered more suitable for the application considered in this research. Relevant specifications of this flywheel module are displayed in Table 5.3. There are larger flywheel modules available which are used in, for instance, voltage regulation in large powergrids. These modules are designed for stationary applications, however, and are therefore not considered here.

Table 5.3: CCM EMAFER RxV-II Flywheel module specifications[22]

<b>Maximum rotational speed</b> $n_{max}$	22000 <i>rpm</i>
<b>Maximum power</b> $P_{max}$	300 <i>kW</i>
<b>Delivered energy</b> $E_{eff}$	4 <i>kWh</i>
<b>System weight</b>	375 <i>kg</i>
<b>System diameter</b>	780 <i>mm</i>
<b>System height</b>	450 <i>mm</i>
<b>Round trip efficiency</b>	90 %

The manufacturer states the maximum amount of energy delivered. Here, it is assumed that the minimum rotational speed of the flywheel is half the maximum speed, as stated in above. This results in the following value for the moment of inertia:

$$J = \frac{2 \cdot E_{fw,eff}}{\omega_{max}^2 - \omega_{min}^2} = 7.235 \text{ kg} \cdot \text{m}^2 \quad (5.23)$$

## Model verification

The model for the flywheel energy storage system has been implemented as described in the previous sections. Unlike the supercapacitor model, the flywheel model is tested by charging and discharging at constant power. The flywheel is tested at constant power because the power in flywheel energy storage systems is determined by the electric machine the flywheel is attached to. If the speed of the flywheel is decreased the torque

of the electric machine increases to maintain constant power. Figure 5.7 and Figure 5.8 show the flywheel state-of-charge and power, respectively.

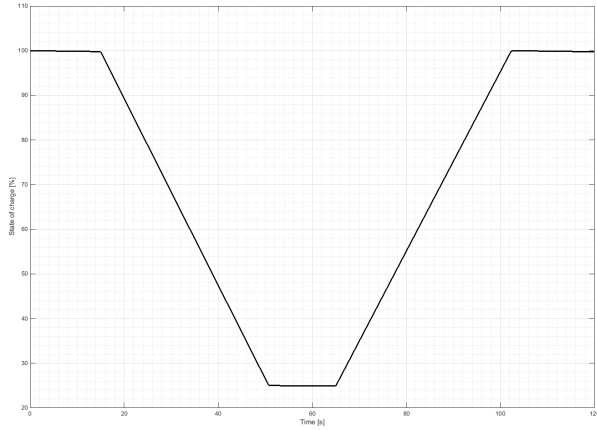


Figure 5.7: Flywheel state-of-charge of a full charge/discharge cycle

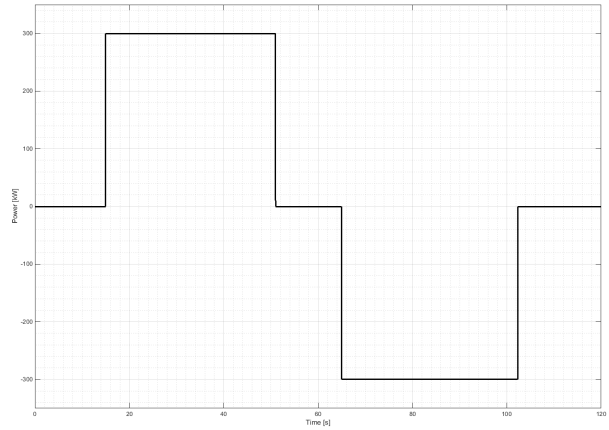


Figure 5.8: Flywheel discharging and charging at constant power

In Figure 5.7, it can be seen that the state-of-charge of the flywheel module slowly decreases over time. Besides the losses caused by the electric machine and the power conversion equipment, the self-discharge of the flywheel is the primary source of energy loss. Figure 5.9 shows a longer period of time after the charge and discharge cycle described above where the self-discharge of the flywheel is displayed better. Secondly, it can be seen that the rate at which the rotational speed decreases, which is proportional to the amount of stored energy, becomes lower as the speed is decreased. More details on the model of the flywheel can be found in Appendix D.3.1.

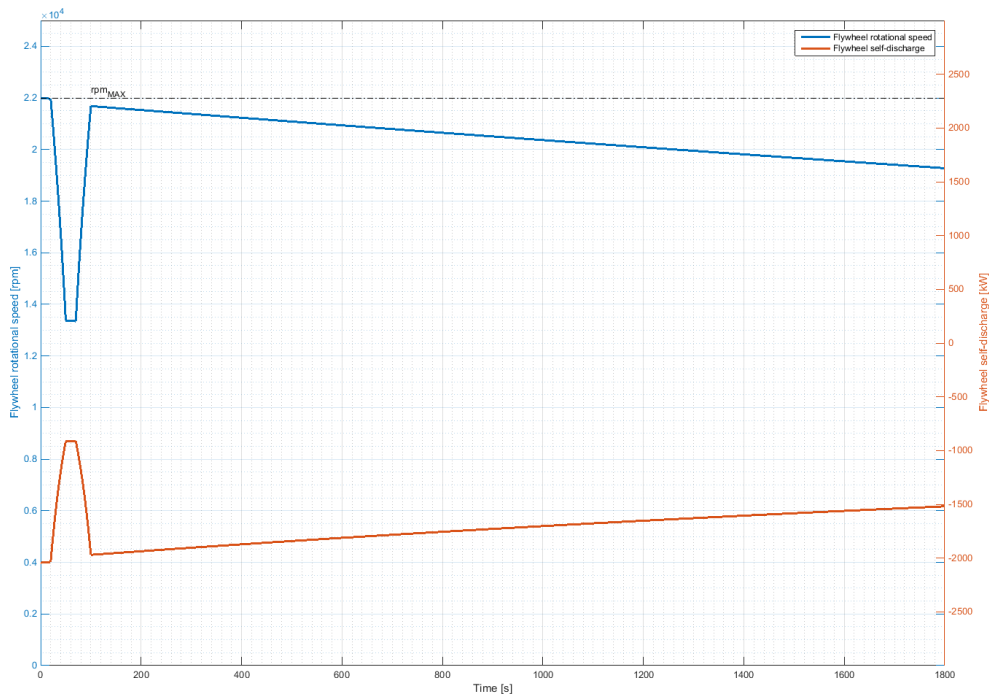


Figure 5.9: Flywheel self-discharge over time

### 5.2.3 Network connection

Both the energy storage systems are connected to the DC bus of the frequency drive of the induction motor. Therefore, the DC bus voltage determines the current from the energy storage  $\bar{i}_{ess}$ . It is possible to directly use the power delivered by the energy storage through the following relation:

$$P_{ess} = \frac{3}{2} \cdot \bar{i}_{ess} \cdot \bar{u}_{dc} \quad (5.24)$$

The multiplication by  $\frac{3}{2}$  in Equation 5.24 is to convert the instantaneous power delivered by the energy storage system to three-phase voltage and current in a dq-reference frame. Rewriting this equation results in the following relation, which determines the current supplied to the frequency drive's DC bus by the energy storage system during discharge.

$$\bar{i}_{ess} = \begin{bmatrix} u_{d,dc} & u_{q,dc} \\ u_{q,dc} & -u_{d,dc} \end{bmatrix}^{-1} \begin{bmatrix} \frac{2}{3} P_{ess} \\ 0 \end{bmatrix} = \frac{\frac{2}{3} P_{ess}}{u_{d,dc}^2 + u_{q,dc}^2} \begin{bmatrix} u_{d,dc} \\ u_{q,dc} \end{bmatrix} = \frac{\frac{2}{3} P_{ess}}{\|\bar{u}_{dc}\|^2} \bar{u}_{dc} \quad (5.25)$$

Charging of the energy storage system when there is a surplus of energy available is modeled as an impedance on the network, so that the power demand changes exponentially with the terminal voltage ( $I^2R$ ). The inputs of the impedance model are a terminal voltage and the active and reactive power of the load. The output of the impedance model is an impedance which is used to determine the relation between the voltage and current. The general impedance is defined as:[62]

$$Z = R + Xj = \frac{U_{nom}^2}{P - Qj} = \frac{U_{nom}^2}{P^2 - Q^2} (P + Qj) \quad (5.26)$$

Where

$R$  and  $X$  denote the resistance and inductance, respectively

$U_{nom}$  is the terminal voltage of the energy storage system

$P$  and  $Q$  denote the active and reactive power, respectively

Equation 5.26 results in a complex impedance, and since all other quantities are expressed in separate d and q terms, this equation needs to be rewritten. Furthermore, the voltage is treated as DC, so there is no reactive power. Finally, by multiplying by  $\frac{-2}{3}$  to denote consumption and to convert the instantaneous power to the dq-reference frame this results in the following impedance matrix:

$$Z = \frac{U_{nom}^2}{\left(\frac{-2P}{3}\right)^2 + Q^2} \begin{bmatrix} \frac{2P}{3} & -Q \\ Q & \frac{2P}{3} \end{bmatrix} = \frac{U_{nom}^2}{\left(\frac{-2P}{3}\right)^2} \begin{bmatrix} \frac{2P}{3} & 0 \\ 0 & \frac{2P}{3} \end{bmatrix} \quad (5.27)$$

Like all other components, the energy storage system can now be connected to the network by a current vector  $\bar{p}$  and admittance matrix  $B$ :

$$\bar{i} = \bar{p} + B\bar{u} \quad (5.28)$$

The current follows directly from the terminal voltage over the source by  $Z$ , so  $\bar{p}_{ess}$  and  $B_{ess}$  are defined as:

$$\bar{p}_{ess} = \begin{bmatrix} 0 \\ 0 \end{bmatrix} \text{ and } B_{ess} = Z^{-1} \quad (5.29)$$

### 5.2.4 Power management

The power management system is modeled according to the description in Section 4.6. Charging and discharging of the ESS is determined based on the evaluation of Equation 4.2 and Equation 4.3. More details on the PMS can be found in Appendix D.3.1.

## 5.3 Driveline component models

### 5.3.1 Main diesel engines

For the modeling of the main diesel engines the Diesel A5.0 model has been used, which has been jointly developed by TU Delft and MTI Holland. The model is based on the Seiliger thermodynamic process and is used to simulate the dynamic behavior of diesel engines.[43] To be compliant with gas mode operation changes have been made to the former version of the model, resulting in desired behavior in both static and transient conditions in gas mode.[41] In the model used to simulate the diesel engines the engine parameters from the medium speed four-stroke MAN L9 48/60CR diesel engines found in the CSD driveline are used.

#### Fuel consumption

The parameters from the engine's product guide have been used to properly simulate the diesel engines. As described in Section 4.7.6 MDO is selected as fuel for the diesel engines. In the model a value of 42.5  $MJ/kg$  is used for the lower heating value (LHV), which is close to the LHV of 42.7  $MJ/kg$  specified by the manufacturer.[38] The specific fuel consumption of the main diesel engines at a constant speed of 500  $rpm$  and different loads is shown in Table 5.4:

Table 5.4: Specific fuel consumption diesel engine[38]

<b>Engine load</b> [%]	100	75	50	25	10
<b>Spec. fuel consumption</b> [g/kWh]	183	183	185	199.5	242

The values from Table 5.4 are used to simulate the specific fuel consumption of the diesel engines. Figure 5.10 shows the results of a simulation where the load on the diesel engine is increased from zero to full load at constant nominal speed. The blue data points in the figure indicate the fuel consumption values displayed in Table 5.4.

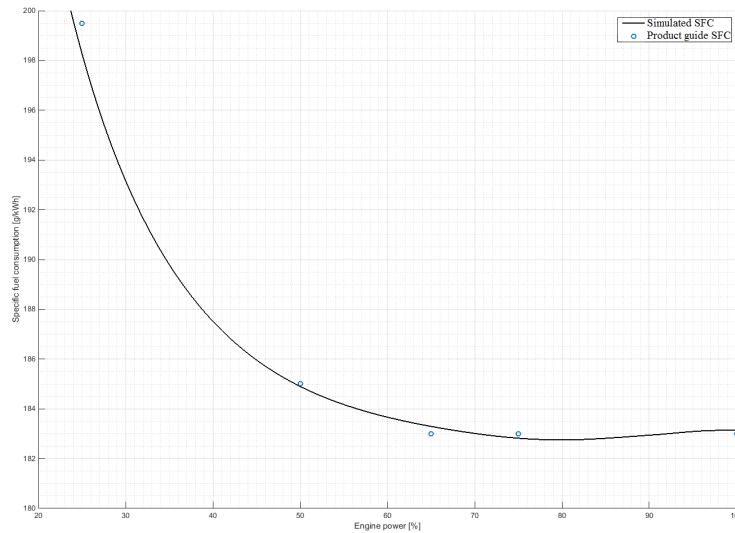


Figure 5.10: Specific fuel consumption at 500 rpm as function of engine load

From Figure 5.10 it can be concluded that the optimum load on the diesel engines in terms of fuel consumption is around 80% to 85% of the total power at constant speed.

### 5.3.2 Dual fuel engines

For the dual fuel engines the specification from the Wärtsilä 12V34DF dual fuel engine is used. The specifications are shown in Table 5.5:

Table 5.5: Wärtsilä 12V34DF specifications [63]

<b>Nominal power</b> $P_{nom}$	6 MW
<b>Nominal speed</b> $n_{nom}$	750 rpm
<b>Strokes per cycle</b> $k$	4
<b>Number of cylinders</b> $i$	12
<b>Engine bore</b> $D$	0.34 m
<b>Engine stroke</b> $S$	0.4 m
<b>Moment of inertia</b> $I$	840 - 930 kg · m <sup>2</sup>

The power output of the dual fuel engine is 6 MW. In the model used to simulate the dual fuel engines the power output of a single cylinder is determined which is then scaled to the total number of cylinders in the engine. To make a better comparison with the diesel engines in the original CSD driveline ten extra cylinders have been added to make a better comparison. The power output of the dual fuel engines is then 11 MW, compared to the 10.8 MW for the original main diesel engines.

### Fuel consumption

For LNG a gas with a MN of 80 is selected, as this is the recommended minimum MN for highly developed engines.[28] Furthermore, referring to Figure 3.7, this MN will not lead to limitations in the engine's power output provided the charge air receiver temperature is not too high.[63]. For LNG a LHV of 49.6 MJ/kg is used. Table 5.6 shows the specific fuel consumption of the dual fuel engines running on LNG. The values specified in the product guide by the manufacturer are expressed in kJ/kWh. The values in Table 5.6 have

been converted to  $g/kWh$  using the LHV stated above.

Table 5.6: Specific fuel consumption dual fuel engines[63]

Engine load [%]	100	85	75	50
Spec. fuel consumption [g/kWh]	149.7	153.0	157.4	172.3
Spec. pilot fuel consumption [g/kWh]	1.9	2.2	2.5	3.8

Figure 5.11 shows the results of a simulation where the load on the dual fuel engine is increased from zero to full load at constant speed. The blue data points in the figure indicate the fuel consumption values displayed in Table 5.6.

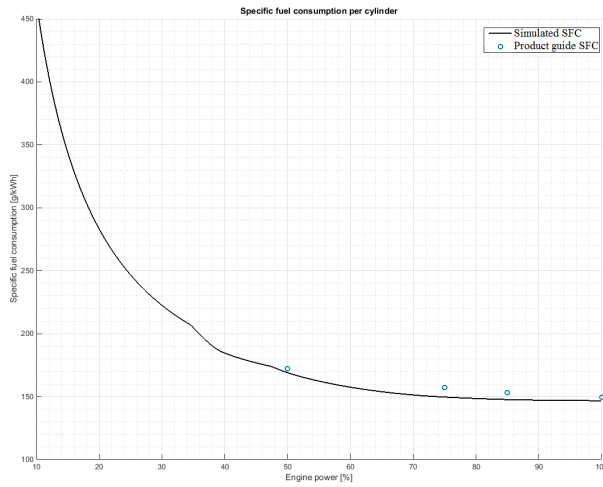


Figure 5.11: Specific fuel consumption at 750 rpm as function of engine load

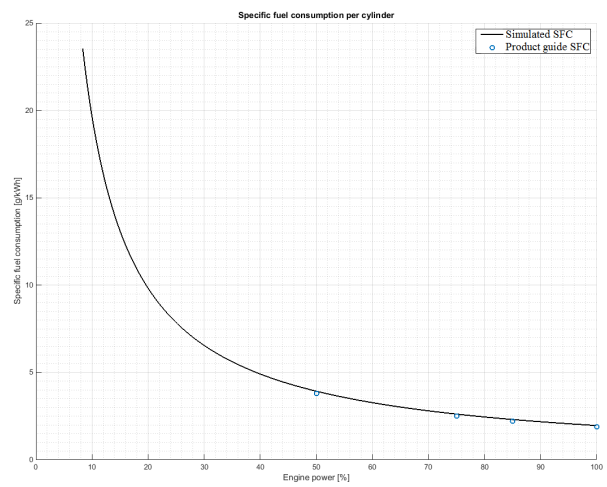


Figure 5.12: Specific pilot fuel consumption at 750 rpm as function of engine load

Typically, a small amount of pilot fuel is added for ignition of LNG. For pilot fuel 1-5% of HFO or MDO is added.[29] Table 5.6 pilot shows the specific pilot fuel consumption. The modelled SFC is shown in Figure 5.12.

Figure 5.13 shows the normalized SFC from Figure 5.10 and Figure 5.11. The values for the SFC are normalized by dividing all values by the SFC of the MAN 9L 48/60CR diesel engine at 100% MCR. From the figure it can be concluded that at high loads the dual fuel engines are more efficient than the diesel engines. At low loads, however, efficiency of the dual fuel engines drops rapidly compared to the diesel engines. It should be noted here that this comparison is made between two different engines running on different fuels.

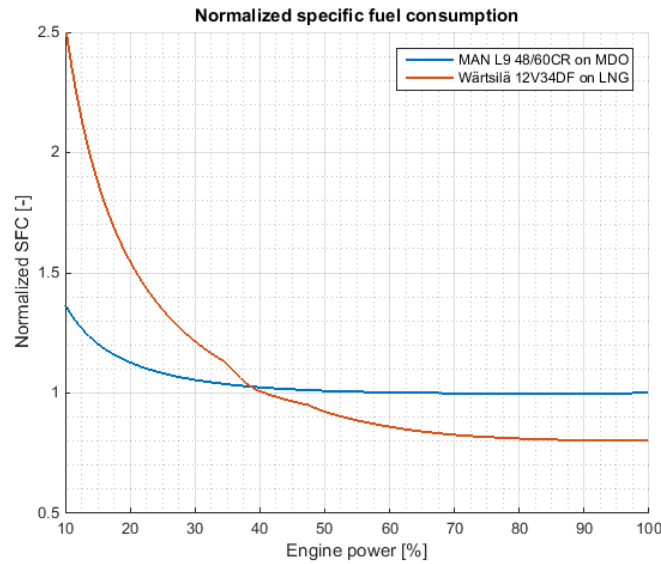


Figure 5.13: Normalized SFC of the diesel and dual fuel engines

### 5.3.3 Induction motors

For modeling of the induction motors a model created at IHC MTI is used. The model parameters have been adapted to properly simulate the induction motors used to drive the CSD cutter head. The model is validated using available measurement data.

Induction motors carry alternating current in both the stator and rotor windings. The stator windings are connected to a balanced three-phase system. Rotor currents are induced by electromagnetic induction from the stator, hence the name induction motor. The stator windings are similar to those of a synchronous machine, as described in Section 5.3.5. The type of induction motor considered here are squirrel cage type induction motors, meaning the rotor windings are short-circuited internally. The alternating current applied to the stator windings produce a field rotating at synchronous speed. Relative motion between the stator field and rotor induces voltages and current in the rotor windings, producing torque depending on the magnitude. Equation 5.30 to Equation 5.37 describe the basis machine equations:

Per unit voltage equation:

$$u_{ds} = R_s i_{ds} - \omega_s \psi_{ds} + \dot{\psi}_{ds} \quad (5.30)$$

$$u_{qs} = R_s i_{qs} + \omega_s \psi_{qs} + \dot{\psi}_{qs} \quad (5.31)$$

$$u_{dr} = R_r i_{dr} - (\omega_s - \omega_r) \psi_{dr} + \dot{\psi}_{dr} \quad (5.32)$$

$$u_{qr} = R_r i_{qr} + (\omega_s - \omega_r) \psi_{qr} + \dot{\psi}_{qr} \quad (5.33)$$

Per unit flux linkage equations:

$$\psi_{ds} = L_{ss} i_{ds} + L_m i_{dr} \quad (5.34)$$

$$\psi_{qs} = L_{ss} i_{qs} + L_m i_{qr} \quad (5.35)$$

$$\psi_{dr} = L_m i_{ds} + L_{rr} i_{dr} \quad (5.36)$$

$$\psi_{qr} = L_m i_{qs} + L_{rr} i_{qr} \quad (5.37)$$

Where

$\omega_s$  is the stator angular velocity in electrical  $rad/s$

$\omega_r$  is the rotor angular velocity in electrical  $rad/s$

$R_s$  is the stator resistance in per unit value

$R_r$  is the rotor resistance in per unit value

$L_m$  is the magnetizing inductance in per unit value

$L_{ss}$  is the stator self-inductance in per unit value

$L_{rr}$  is the rotor self-inductance in per unit value

In the equation given above it is assumed that magnetic saturation and hysteresis can be neglected. Furthermore, purely sinusoidal distribution of flux waves are assumed.[35]

For modeling purposes, the equations for the voltages and flux linkages are summarized by Equation 5.38 and Equation 5.39. Time is expressed in seconds, therefore all quantities are multiplied by base frequency  $\omega_{eB}$ . Furthermore, since induction motor of the squirrel-cage type are considered, the rotor voltages are zero because of short-circuiting through end rings on the rotor.[35]

$$\begin{bmatrix} \dot{\psi}_{ds} \\ \dot{\psi}_{qs} \\ \dot{\psi}_{dr} \\ \dot{\psi}_{qr} \end{bmatrix} = \begin{bmatrix} 0 & \omega_s & 0 & 0 \\ -\omega_s & 0 & 0 & 0 \\ 0 & 0 & 0 & (\omega_s - \omega_r) \\ 0 & 0 & (\omega_s - \omega_r) & 0 \end{bmatrix} \begin{bmatrix} \psi_{ds} \\ \psi_{qs} \\ \psi_{dr} \\ \psi_{qr} \end{bmatrix} + \omega_{eB} \begin{bmatrix} -R_s & 0 & 0 & 0 \\ 0 & -R_s & 0 & 0 \\ 0 & 0 & -R_r & 0 \\ 0 & 0 & 0 & -R_r \end{bmatrix} \begin{bmatrix} i_{ds} \\ i_{qs} \\ i_{dr} \\ i_{qr} \end{bmatrix} + \omega_{eB} \underbrace{\begin{bmatrix} 1 & 0 \\ 0 & 1 \\ 0 & 0 \\ 0 & 0 \end{bmatrix}}_{S_{im}} \begin{bmatrix} u_{ds} \\ u_{qs} \end{bmatrix} \quad (5.38)$$

$$\begin{bmatrix} \psi_{ds} \\ \psi_{qs} \\ \psi_{dr} \\ \psi_{qr} \end{bmatrix} = \underbrace{\begin{bmatrix} L_{ss} & 0 & L_m & 0 \\ 0 & L_{ss} & 0 & L_m \\ L_m & 0 & L_{rr} & 0 \\ 0 & L_m & 0 & L_{rr} \end{bmatrix}}_{L_{im}} \begin{bmatrix} i_{ds} \\ i_{qs} \\ i_{dr} \\ i_{qr} \end{bmatrix} \quad (5.39)$$

### Mechanical equations

The rotor current reacting with the stator field produces a torque, accelerating the rotor in the direction of the rotation of the stator field. The current and voltages induced in the rotor approach zero when the rotor speed  $n_r$  approaches stator field speed  $n_s$ . In order to produce positive torque,  $n_r$  must be smaller than  $n_s$ . The slip of the rotor is defined by Equation 5.40:

$$s = \frac{n_s - n_r}{n_s} \quad (5.40)$$

At zero load, the slip of the induction motor is negligible. When a mechanical load is applied the rotor speed decreases. The slip is increased and consequently the voltage and current increase, producing the required torque. The electrical torque developed in the induction machine follows from the power transfer across the air-gap. Eliminating the rotor currents by expressing them in terms of stator currents and rotor flux linkages using Equation 5.39 the mechanical torque is given by:[35]

$$\tau_m = (\psi_{dr} i_{qs} - \psi_{qr} i_{ds}) \frac{L_m}{L_{rr}} - K_D \omega_{shaft} \quad (5.41)$$

The torque developed by the diesel engine model is in SI units. Therefore, the motor torque in Equation 5.41 needs to be multiplied by the base value for the torque  $\tau_B$ . Here,  $K_D$  denotes the coefficient of viscous damping and  $\omega_{shaft}$  is the mechanical speed of the motor shaft, which follow from Equation 5.42:

$$\frac{d}{dt} \omega_{shaft} = \frac{1}{J_m + J_l} (\tau_m - \tau_l) = \frac{2}{p} \frac{d}{dt} \omega_r \quad (5.42)$$

Where

$J_m$  is the moment of inertia of the motor in  $kg \cdot m^2$

$J_l$  is the moment of inertia of the load in  $kg \cdot m^2$

$\omega_r$  is the rotor's electrical angular velocity in  $rad/s$   
 $p$  is the number of poles

### Motor parameter measurement

Figure 5.14 shows the equivalent circuit of an induction motor as recommended by the IEEE. The parameters needed for motor calculations can be measured by performing several tests. First, the stator resistance  $R_s$  can be measured by applying a DC voltage to the stator windings. Since the reactances are zero when applying direct current and because there is no induced voltage, so no resulting current in the rotor circuit, the only resistance that remains is the stator resistance. By conducting a no-load test, the slip becomes zero. As a result the rotor resistance becomes infinite, as can be seen in Figure 5.14, and no current will flow through the rotor. This makes it possible to determine the value of the combined stator and magnetizing reactances. Finally, by blocking the rotor the slip will become one and no current will flow through the magnetizing reactance. The remaining values can now be measured and by combining these measurements all motor parameters can be determined. The parameters of the dredge pump motors determined in this way are shown in table 5.7.

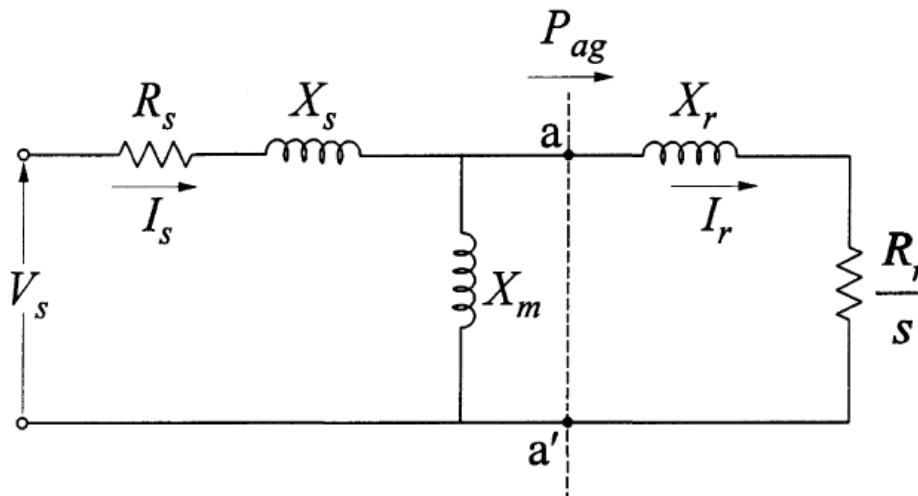


Figure 5.14: Induction motor equivalent circuit[35]

The values of stator reactance  $X_s$  and rotor reactance  $X_r$  used in the motor calculations can be found using the following equations:[35]

$$X_s = \omega_s(L_{ss} - L_m) \quad (5.43)$$

$$X_r = \omega_s(L_{rr} - L_m) \quad (5.44)$$

Where  $\omega_s$  is the angular velocity of the stator field in electrical  $rad/s$ .

Table 5.7: Measured dredge pump motor parameters

<b>Stator self-inductance</b> $L_{ss}$	0.053 $mH$
<b>Rotor self-inductance</b> $L_{rr}$	0.053 $mH$
<b>Magnetizing inductance</b> $L_m$	1.942 $mH$
<b>Stator resistance</b> $R_s$	1.218 $m\Omega$
<b>Rotor resistance</b> $R_r$	3.028 $m\Omega$

The motor parameters determined here are the same for the electric motors used in the cutter driveline. However, by operating the motors at an electrical frequency of 40  $Hz$  and a voltage of 566  $V$  the power output of the motor is 1750  $kW$  instead of 2200  $kW$ .

### Motor parameters for simulations

The parameters used for simulation of the electric motor are shown in table 5.8. The values are found by using Equation 5.43 and Equation 5.44 and dividing all values by the base value for that quantity. For all other simulation quantities per unit values are also used.

Table 5.8: Motor parameters used in simulations

<b>Stator reactance</b> $X_s$	6.4826 p.u.
<b>Rotor reactance</b> $X_r$	6.4826 p.u.
<b>Magnetizing reactance</b> $X_m$	6.4241 p.u.
<b>Stator resistance</b> $R_s$	0.0079 p.u.
<b>Rotor resistance</b> $R_r$	0.0196 p.u.

### Motor efficiency

The efficiency of the induction motor model is dependent on the load applied to the motor. As a result, the efficiency at low loads is above 100% and decreases to the correct efficiency as the load on the motor is increased. Therefore, the efficiency has been corrected based on the load applied to the induction motor resulting in a constant efficiency equal to the value given in Table 2.4.

### Model validation

In Figure 5.15 the torque-slip characteristic of the electric motor when applying nominal voltage is shown. The starting torque and starting current are displayed as a function of the motor slip. Figure 5.16 shows the simulated torque-slip characteristic when applying nominal voltage. At first glance the shape of the simulated figure seems to match the one from the measurements. When comparing the maximum torque, however, there is some difference between the two values. During measurements the maximum torque reaches over three times the nominal value for torque at around 45  $kNm$  where the simulated maximum torque during start-up is only 36  $kNm$ . The difference in maximum starting torque is unlikely to cause problems during simulation because the starting of the motors is not considered during simulations. The electric motors will already be running near their nominal speed during simulation and it is only during start-up that the large difference in torque is present. During the cutting proces the torque of the electric motors is unlikely to greatly exceed the nominal torque.

Secondly, when applying nominal torque to the motors at nominal speed, the current matches the nominal current, as can be seen in Figure 5.17. Here, a load of half the nominal torque followed by a load at nominal torque is applied after starting of the motor. These loads are indicated by the dashed lines. At nominal torque the motor draws a current of just over 2300  $A$ . This closely matches the value of 2345  $A$  given by the manufacturer. At half the nominal torque the motor draws a current of around 1200  $A$ , which matches the measured current at this load during the cutting process. It is therefore concluded that the parameters determined in this section match the real values well enough to be used to simulate the cutter motors.

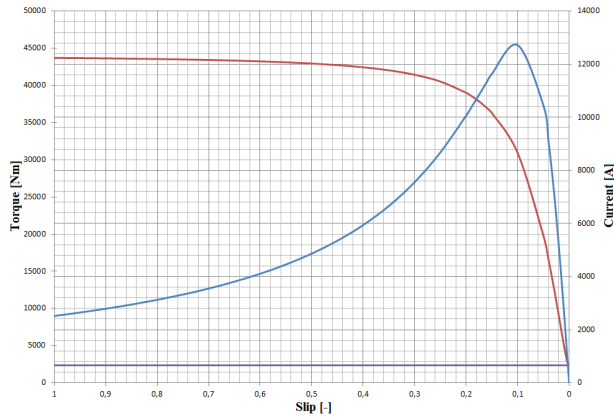


Figure 5.15: Measured torque-slip characteristic

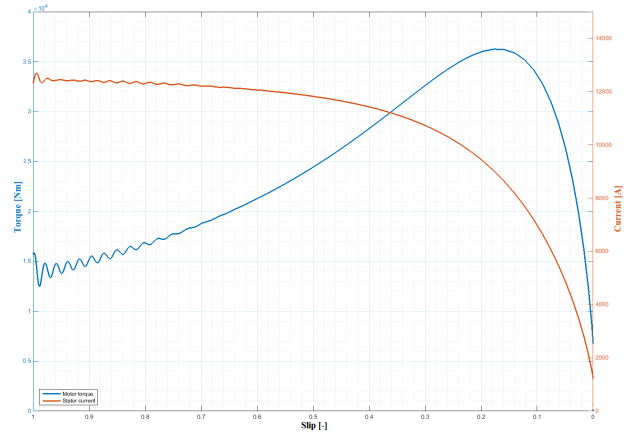
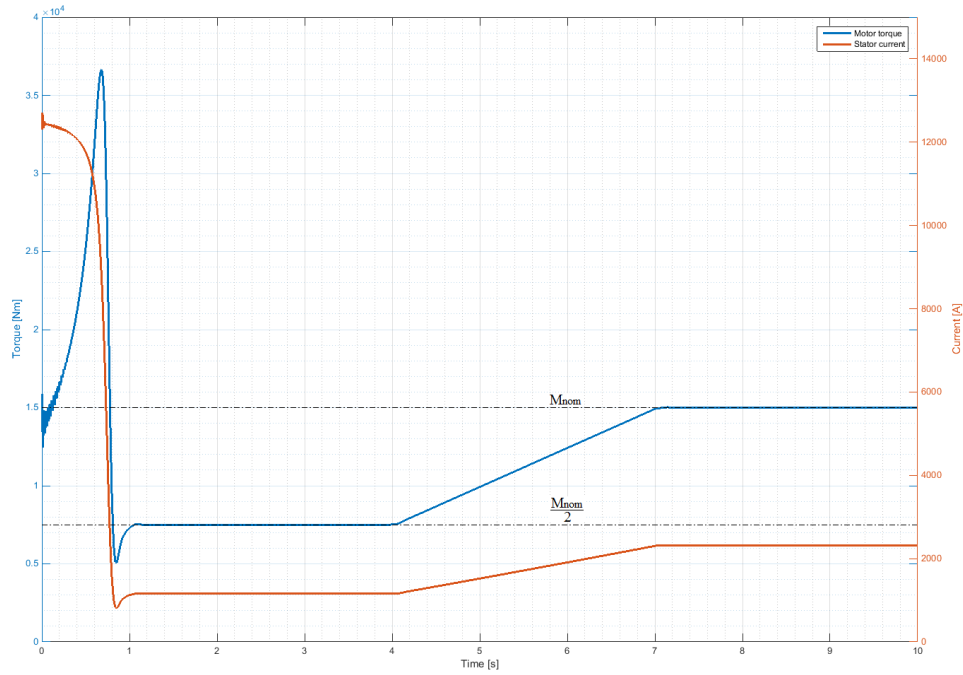


Figure 5.16: Simulated torque-slip characteristic

Figure 5.17: Current at  $M_{nom}$  and  $\frac{1}{2}M_{nom}$ 

### Network connection

The induction motor is connected to the network by a current vector  $\bar{p}$  and an admittance matrix B so that the relation between the induction motor voltage and current is defined as:

$$\bar{i} = \bar{p} + B\bar{u} \quad (5.45)$$

Current vector  $\bar{p}$  can be derived from Equation 5.39. The voltage is determined by the frequency drive's DC bus voltage  $\bar{u}_{dc}$  so B has no contribution to the induction motor current.

$$\bar{i}_{im} = \underbrace{-S_{im}^{-1} \cdot L_{im}^{-1} \cdot \bar{\Psi} \cdot I_B}_{\bar{p}_{im}} + \underbrace{\begin{bmatrix} 0 & 0 \\ 0 & 0 \end{bmatrix}}_{B_{im}} \bar{u}_{im} \quad (5.46)$$

As described in the previous section the rotor voltages are zero. Therefore, the current vector is multiplied by  $S_{im}$ . The negative sign results from the fact the the induction motor draws current. Finally, all quantities are in per unit values, so the current is multiplied by the base value  $I_B$  to get the actual value.

### 5.3.4 Frequency drives

For the frequency drive a model created at IHC MTI is used. Similar to the induction motor model, the parameters have been adapted to make the frequency drive model compatible with the induction motors used to drive the cutter head. The frequency drive, which is used to slowly bring the induction motor up to speed, is modeled according to the schematic shown in Figure 5.18. The frequency drive assures a slow increase in load to the grid caused by the high currents during starting of the induction motors.

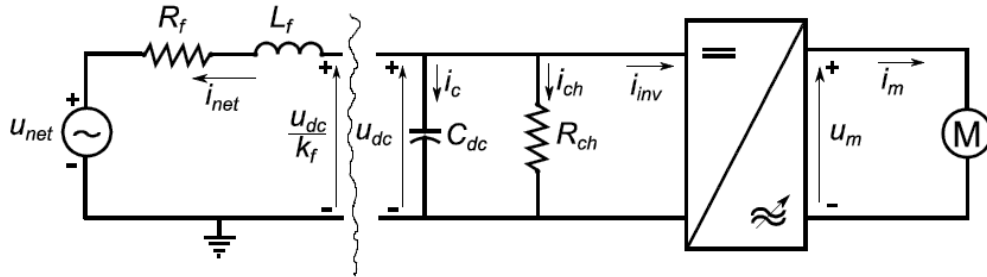


Figure 5.18: Modeled frequency drive interconnection with motor and network[62]

The DC bus is modeled by a dynamics capacitor model, which is defined by:[62]

$$\frac{d}{dt} \bar{u}_{dc} = -\frac{1}{C_{dc}} (\bar{i}_{net} + \bar{i}_{ch} + \bar{i}_{inv}) \quad (5.47)$$

Where

$\bar{u}_{dc}$  is the DC voltage vector

$C_{dc}$  is the capacitance of the DC bus

$\bar{i}_{ch}$  is the current vector of the chopper

$\bar{i}_{inv}$  is the current vector of the inverter

The relation between the network voltage, current and the voltage of the DC-bus is given by Equation 5.48:

$$\underbrace{\frac{u_{dc}}{k_f} - u_{net}}_{\Delta U} = \frac{i_{net}}{\sqrt{2}} \cdot Z_f \quad (5.48)$$

Where

$Z_f$  is the impedance given by  $\|R_f + X_f\|$

$k_f$  is the conversion factor of the converter

Because all voltages and currents are composed of dq-components it is convenient to also express DC voltage  $\bar{u}_{dc}$  in dq-components. Network current  $i_{net}$  is a RMS value, therefore Equation 5.48 can be rewritten as:

$$\bar{i}_{net} = \frac{1}{Z_f^2} ((R_f - X_f) \cdot \Delta U_d + (R_f + X_f) \cdot \Delta U_q) \quad (5.49)$$

Equation 5.49 can be rewritten as:

$$\bar{i}_{net} = \frac{1}{R_f^2 + X_f^2} \begin{bmatrix} R_f & X_f \\ -X_f & R_f \end{bmatrix} \Delta \bar{U} \quad (5.50)$$

Finally, the frequency drive needs to be compliant with the rest of the network so that the following network equation can be solved:

$$\bar{i} = \bar{p} + B\bar{u} \quad (5.51)$$

Therefore, by substitution of Equation 5.26, Equation 5.50 is rewritten as:

$$\bar{i}_{net,fd} = \underbrace{\begin{bmatrix} R_f & -L_f\omega_{net} \\ L_f\omega_{net} & R_f \end{bmatrix}^{-1} \frac{\bar{u}_{dc}}{k_f}}_{\bar{p}_{fd}} + \underbrace{\begin{bmatrix} -R_f & L_f\omega_{net} \\ -L_f\omega_{net} & -R_f \end{bmatrix}^{-1}}_{B_{fd}} \bar{u}_{net} \quad (5.52)$$

### Speed control

The speed of the induction motors is controlled using a PI-controller. This controller adjusts the stator's electric angular velocity based on the error between the angular velocity of the rotor and the desired speed. A schematic overview of the PI-controller is shown in Figure 5.19.

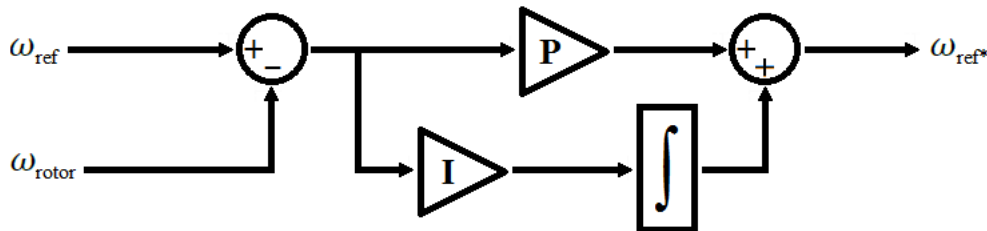


Figure 5.19: PI controller used to control the speed of the induction motors

Because the torque produced by an induction motor is proportional to the air gap flux the air gap flux has to remain constant to be able to produce maximum torque. The magnitude of the magnetic flux in the air gap is proportional to the ratio of the per unit voltage to the per unit frequency. So in order to maintain a constant air gap flux the stator voltage needs to be adjusted accordingly if the stator frequency changes.[35] This is referred to as volt per Hertz control and is used to make the induction motor's torque independent of the motor speed.

### 5.3.5 Synchronous generators

#### Generator model

For the generator model a model is used created at IHC MTI, the parameters used and the model verification is described at the end of this section. A three-phase synchronous generator consists of two elements, the field

winding and the armature winding. The field winding carries DC and produces a magnetic field inducing alternating voltages in the armature windings, which are distributed 120° apart in space. Figure 5.20 shows the schematic of a cross section of a three-phase synchronous machine.

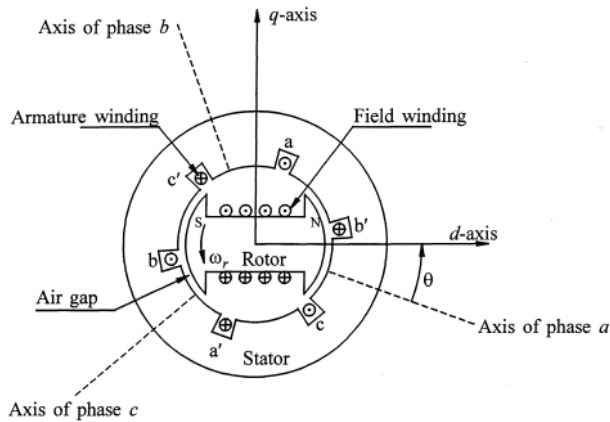


Figure 5.20: Schematic diagram of a three-phase synchronous machine[35]

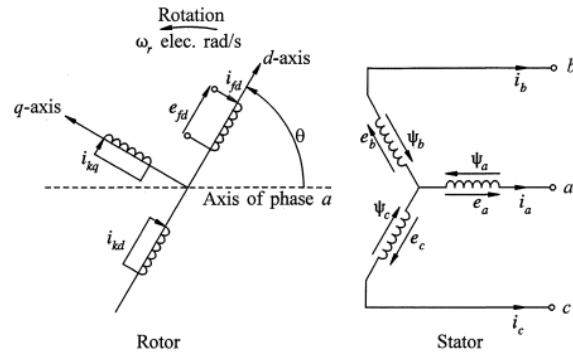


Figure 5.21: Stator and rotor circuits of a synchronous machine[35]

For the mathematical description of the synchronous machine the coupled circuits in Figure 5.21 are used. The rotor circuit is comprised of a field winding and a number of amortisseur windings. The amortisseur windings are connected to the end rings of the rotor to form short-circuited windings similar to those of a squirrel cage induction motor. For simplicity only one amortisseur circuit is assumed in each axis in Figure 5.21. Two currents are considered, one flowing in line with the field axis and one perpendicular to it.

Values for the inductances, defined by the flux linkage per unit current, are a function of the rotor position and hence vary in time. Therefore, a dq0 reference frame which rotates with the rotor is used to simplify computation. The stator circuits are now represented by two fictitious armature windings of which the axes coincide with the d-axis and q-axis, respectively. In this analysis only one d-axis amortisseur circuit is considered, denoted by the subscript 1d. The voltage in the q-axis, which leads the d-axis by 90° in Figure 5.21, is induced by the flux in the d-axis. Similarly, the voltage in the d-axis is induced by the flux in an axis lagging the d-axis by 90°. Therefore, two q-axis amortisseur circuits are considered, denoted by 1q and 2q. By taking the basic equations of a synchronous machine converted to dq0 components and dividing each quantity by its base value the following per unit equation for the voltages  $e_k$  and flux  $\psi_k$  linkages are obtained:[35]

Per unit stator voltage equations:

$$e_d = \dot{\psi}_d - \psi_q \omega_r - R_a i_d \quad (5.53)$$

$$e_q = \dot{\psi}_q + \psi_d \omega_r - R_a i_q \quad (5.54)$$

Per unit rotor voltage equations:

$$e_{fd} = \dot{\psi}_{fd} + R_{fd} i_{fd} \quad (5.55)$$

$$0 = \dot{\psi}_{1d} + R_{1d} i_{1d} \quad (5.56)$$

$$0 = \dot{\psi}_{1q} + R_{1q} i_{1q} \quad (5.57)$$

$$0 = \dot{\psi}_{2q} + R_{2q} i_{2q} \quad (5.58)$$

Per unit stator flux linkage equations:

$$\psi_d = -(L_{ad} + L_l) i_d + L_{ad} i_{fd} + L_{ad} i_{1d} \quad (5.59)$$

$$\psi_q = -(L_{aq} + L_l) i_q + L_{aq} i_{1q} + L_{aq} i_{2q} \quad (5.60)$$

Per unit rotor flux linkage equations:

$$\psi_{fd} = L_{fdd} i_{fd} + L_{f1d} i_{1d} - L_{ad} i_d \quad (5.61)$$

$$\psi_{1d} = L_{f1d} i_{fd} + L_{11d} i_{1d} - L_{ad} i_d \quad (5.62)$$

$$\psi_{1q} = L_{11q} i_{1q} + L_{aq} i_{2q} - L_{aq} i_q \quad (5.63)$$

$$\psi_{2q} = L_{aq} i_{1q} + L_{22q} i_{2d} - L_{aq} i_q \quad (5.64)$$

Where

$\omega_r$  is the rotor angular velocity in electrical rad/s

$R_k$  is the resistance of subscript  $k$  in per unit value

$L_k$  is the inductance of subscript  $k$  in per unit value

$i_k$  is the current flowing through subscript  $k$  in per unit value

For Equation 5.53 to Equation 5.64 it is assumed that sinusoidally distributed flux waves are produced. Again, no magnetic saturation is neglected

For modeling purposes, the equations for the voltages and flux linkages are summarized by Equation 5.65 and Equation 5.66. Time is expressed in seconds, therefore all quantities are multiplied by base frequency  $\omega_{eB}$ .

$$\begin{aligned}
 \begin{bmatrix} \dot{\psi}_d \\ \dot{\psi}_q \\ \dot{\psi}_{fd} \\ \dot{\psi}_{1d} \\ \dot{\psi}_{1q} \\ \dot{\psi}_{2q} \end{bmatrix} &= \begin{bmatrix} 0 & \omega_r & 0 & 0 & 0 & 0 \\ -\omega_r & 0 & 0 & 0 & 0 & 0 \\ 0 & 0 & 0 & 0 & 0 & 0 \\ 0 & 0 & 0 & 0 & 0 & 0 \\ 0 & 0 & 0 & 0 & 0 & 0 \\ 0 & 0 & 0 & 0 & 0 & 0 \end{bmatrix} \begin{bmatrix} \psi_d \\ \psi_q \\ \psi_{fd} \\ \psi_{1d} \\ \psi_{1q} \\ \psi_{2q} \end{bmatrix} + \omega_{eB} \begin{bmatrix} R_a & 0 & 0 & 0 & 0 & 0 \\ 0 & R_a & 0 & 0 & 0 & 0 \\ 0 & 0 & -R_{fd} & 0 & 0 & 0 \\ 0 & 0 & 0 & -R_{1d} & 0 & 0 \\ 0 & 0 & 0 & 0 & -R_{1q} & 0 \\ 0 & 0 & 0 & 0 & 0 & -R_{2q} \end{bmatrix} \\
 &+ \omega_{eB} \begin{bmatrix} 1 & 0 \\ 0 & 1 \\ 0 & 0 \\ 0 & 0 \\ 0 & 0 \\ 0 & 0 \end{bmatrix} \begin{bmatrix} e_d \\ e_q \end{bmatrix} + \omega_{eB} \begin{bmatrix} 0 \\ 0 \\ 1 \\ 0 \\ 0 \\ 0 \end{bmatrix} e_{fd} \tag{5.65}
 \end{aligned}$$

$$\begin{bmatrix} \psi_d \\ \psi_q \\ \psi_{fd} \\ \psi_{1d} \\ \psi_{1q} \\ \psi_{2d} \end{bmatrix} = \begin{bmatrix} -(L_{ad} + L_l) & 0 & L_{ad} & L_{ad} & 0 & 0 \\ 0 & -(L_{aq} + L_l) & 0 & 0 & L_{aq} & L_{aq} \\ -L_{ad} & 0 & L_{ffd} & L_{f1d} & 0 & 0 \\ -L_{ad} & 0 & L_{f1d} & L_{11d} & 0 & 0 \\ 0 & -L_{aq} & 0 & 0 & L_{11q} & L_{aq} \\ 0 & -L_{aq} & 0 & 0 & L_{aq} & L_{22q} \end{bmatrix} \begin{bmatrix} i_d \\ i_q \\ i_{fd} \\ i_{1d} \\ i_{1q} \\ i_{2q} \end{bmatrix} \tag{5.66}$$

Where the inductances in Equation 5.66 are defined as:

$$\begin{aligned}
 L_{ad} &= L_d - L_l & L_{11d} &= L_{f1d} + L_{1d} \\
 L_{aq} &= L_q - L_l & L_{11q} &= L_{aq} + L_{1q} \\
 L_{ffd} &= L_{ad} + L_{fd} & L_{22q} &= L_{aq} + L_{2q} \\
 L_{f1d} &= L_{ffd} - L_{fd}
 \end{aligned}$$

The per unit system with reciprocal mutual inductances allows the use of the equivalent circuits in Figure 5.22 and Figure 5.23 to represent synchronous machine characteristics. The difference between the two circuits is field winding source  $u_{fd}$ , which is used to control the magnetization in the rotor's d-axis

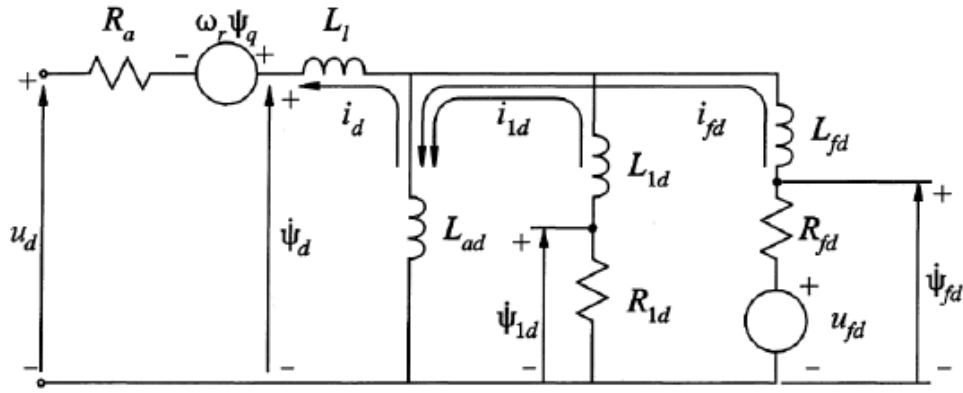


Figure 5.22: d-axis equivalent circuit[35]

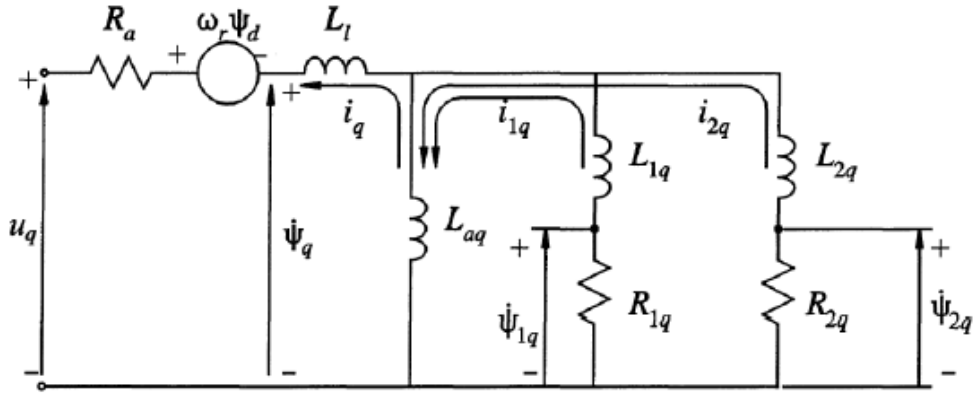


Figure 5.23: q-axis equivalent circuit[35]

Since the transients of a network decay quickly, especially in small networks, network dynamics are neglected. The dynamics of the stator, which is connected to the network, can therefore also be neglected, meaning  $\dot{\psi}_d$  and  $\dot{\psi}_q$  are both zero. This leaves the following equations for the flux dynamics:[65]

$$\dot{\psi}_{fd} = \omega_{eB} \left( \frac{-R_{fd}}{L_{fd}} \psi_{fd} + \frac{R_{fd}}{L_{fd}} \psi_{ad} + e_{fd} \right) \quad (5.67)$$

$$\dot{\psi}_{1d} = \omega_{eB} \left( \frac{-R_{1d}}{L_{1d}} \psi_{1d} + \frac{R_{1d}}{L_{1d}} \psi_{ad} \right) \quad (5.68)$$

$$\dot{\psi}_{1q} = \omega_{eB} \left( \frac{-R_{1q}}{L_{1q}} \psi_{1q} + \frac{R_{1q}}{L_{1q}} \psi_{aq} \right) \quad (5.69)$$

$$\dot{\psi}_{2q} = \omega_{eB} \left( \frac{-R_{2q}}{L_{2q}} \psi_{2q} + \frac{R_{2q}}{L_{2q}} \psi_{aq} \right) \quad (5.70)$$

Here,  $\psi_{aq}$  and  $\psi_{aq}$  are the mutual flux linkages of the d-axis and q-axis given by:

$$\psi_{ad} = \frac{L''_{ad}}{L_{fd}} \psi_{fd} + \frac{L''_{ad}}{L_{1d}} \psi_{1d} - L''_{ad} i_d \quad (5.71)$$

$$\psi_{aq} = \frac{L''_{aq}}{L_{1d}} \psi_{1d} + \frac{L''_{aq}}{L_{2q}} \psi_{2q} - L''_{aq} i_q \quad (5.72)$$

Where  $L_{ad}$  and  $L_{aq}$  are the subtransient mutual inductances in per unit value and defined as:

$$L''_{ad} = \left( \frac{1}{L_{ad}} + \frac{1}{L_{fd}} + \frac{1}{L_{1d}} \right)^{-1}$$

$$L''_{aq} = \left( \frac{1}{L_{aq}} + \frac{1}{L_{1q}} + \frac{1}{L_{2q}} \right)^{-1}$$

Rearranging and substituting the equations above into Equation 5.65 results in the relation between the stator voltage and stator current:

$$\underbrace{\begin{bmatrix} -R_a & \frac{\omega_r}{\omega_{eB}} L_l & 0 & -\frac{\omega_r}{\omega_{eB}} L_{aq} \\ -\frac{\omega_r}{\omega_{eB}} L_l & -R_a & \frac{\omega_r}{\omega_{eB}} L_{aq} & 0 \\ L''_{ad} & 0 & L_{ad} & 0 \\ 0 & L''_{aq} & 0 & L_{aq} \end{bmatrix}}_{L_g} \begin{bmatrix} i_d \\ i_q \\ i_{ad} \\ i_{aq} \end{bmatrix} = \underbrace{\begin{bmatrix} 0 & 0 & 0 & 0 \\ 0 & 0 & 0 & 0 \\ \frac{L''_{ad}}{L_{fd}} & \frac{L''_{ad}}{L_{1d}} & 0 & 0 \\ 0 & 0 & \frac{L''_{aq}}{L_{1q}} & \frac{L''_{aq}}{L_{2q}} \end{bmatrix}}_{F_g} \begin{bmatrix} \psi_{fd} \\ \psi_{1d} \\ \psi_{1q} \\ \psi_{2q} \end{bmatrix} + \underbrace{\begin{bmatrix} 1 & 0 \\ 0 & 1 \\ 0 & 0 \\ 0 & 0 \end{bmatrix}}_{S_g} \begin{bmatrix} u_d \\ u_q \end{bmatrix} \quad (5.73)$$

### Voltage regulation

An automatic voltage regulator (AVR) is used to maintain the generator output voltage constant. The AVR is modelled as a PID-controller that calculates the error between the generator's output voltage and the reference voltage. Based on the error between the two voltages, the field excitation  $e_{fd}$  is consequently altered.

### Mechanical equations

The torque developed by the generator follows from the power transfer across the air gap is given by:[35]

$$\tau_g = (\psi_d i_q - \psi_q i_d) - K_D \omega_{shaft} \quad (5.74)$$

The torque developed by the diesel engine model is in SI units. Therefore, the generator torque in Equation 5.74 needs to be multiplied by the base value for the torque  $\tau_B$ . Here,  $K_D$  denotes the coefficient of viscous damping and  $\omega_{shaft}$  is the mechanical speed of the generator shaft, which follows from Equation 5.75:

$$\frac{d}{dt} \omega_{shaft} = \frac{1}{J_g + J_{de}} (\tau_{de} - \tau_g) = \frac{2}{p} \frac{d}{dt} \omega_r \quad (5.75)$$

Where

$J_g$  is the moment of inertia of the generator shaft in  $kg \cdot m^2$

$J_{de}$  is the moment of inertia of the diesel engine shaft in  $kg \cdot m^2$

$\omega_r$  is the rotor's electrical angular velocity in  $rad/s$

$p$  is the number of poles

### Generator parameters

Some of the parameters necessary to simulate the four 4500 KVA synchronous generators that provide power to the cutter driveline are unknown. Therefore, the parameters of the generators from a pipelay vessel have been used, which provide a similar amount of power but operate at 6600 V instead of 690V. The parameters used are shown in Table 5.9.

Table 5.9: Generator parameters used in simulations

D-axis synchronous reactance $X_d$	2.65 p.u.
Q-axis synchronous reactance $X_q$	2.40 p.u.
D-axis transient reactance $X'_d$	0.217 p.u.
Q-axis transient reactance $X'_q$	1.000 p.u.
D-axis subtransient reactance $X''_d$	0.127 p.u.
Q-axis subtransient reactance $X''_q$	0.200 p.u.
Transient D-axis open circuit time constant $T'_{do}$	2.5918 p.u.
Transient Q-axis open circuit time constant $T'_{qo}$	1.5626 p.u.
Subtransient D-axis open circuit time constant $T''_{do}$	0.0081 p.u.
Subtransient Q-axis open circuit time constant $T''_{qo}$	0.1584 p.u.
Armature resistance $R_a$	0.009 p.u.
Leakage reactance $X_l$	0.07 p.u.

### Model verification

An advantage of using the parameters shown in Table 5.9 is that for these values the generator model as described here has already been validated.[62] However, since the generator model is scaled the model will still have to be verified as it is implemented here. The verification of the generator current is described in Section 5.6. For the validation of the torque developed by the scaled generator the same validation process has been repeated as for the original model. The results are shown in Figure 5.24 and Figure 5.25.

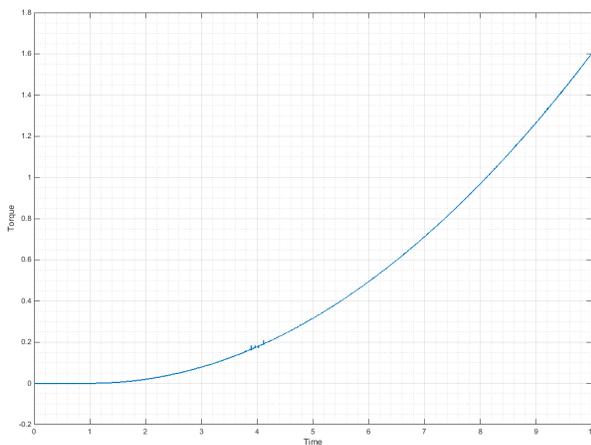


Figure 5.24: Torque produced by the original 4100 kVA generator

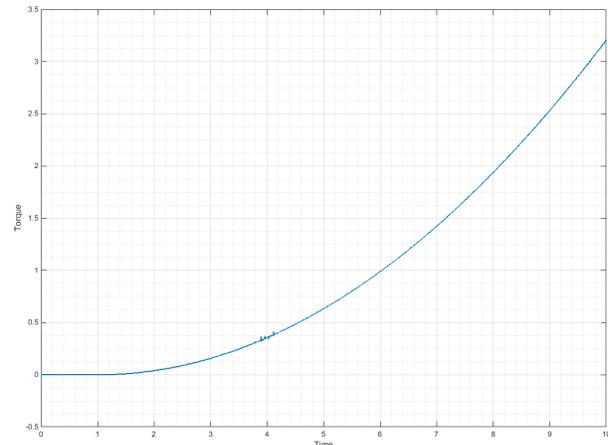


Figure 5.25: Torque produced by a 8200kVA generator at double load

In Figure 5.25 the result is shown of a synchronous generator that has been scaled to double the apparent power of the generator shown in Figure 5.24. Double the electric load is applied to the scaled generator and as can be seen in the figure, the generator produces double the torque. Therefore, it is concluded that a single scaled generator behaves the same as several smaller generators. The amount of torque produced by a single larger generator is the same as the combined amount of torque produced by several smaller generators

sharing the same load.

### Network connection

The generator is connected to the network by a current vector  $\bar{p}$  and an admittance matrix  $B$  so that the relation between generator voltage and current is defined as:

$$\bar{i} = \bar{p} + B\bar{u} \quad (5.76)$$

Both current vector  $\bar{p}$  and admittance matrix  $B$  can be derived from Equation 5.73:

$$\bar{i} = \underbrace{F_g \cdot \bar{\Psi} \cdot L_g^{-1}}_{\bar{p}} + \underbrace{S_g \cdot L_g^{-1}}_B \cdot \bar{u} \quad (5.77)$$

The terminal voltage and current of the synchronous machine still have to be transformed to the actual voltage and current it is delivering to the network, however. If the frequency and phase of the generator are the same as that of the network no power will be delivered. The torque angle  $\delta_g$ , defined by  $\frac{d}{dt}\delta_g = \omega_r - \omega_e$ , determines the actual voltage and current. The relation between the synchronous machine output and the network is defined as:

$$\bar{u}_g = D_g \cdot \bar{u}_{net} \quad \text{and} \quad \bar{i}_g = D_g \cdot \bar{i}_{net} \quad (5.78)$$

Where

$$D_g = \begin{bmatrix} \sin \delta_g & -\cos \delta_g \\ \cos \delta_g & \sin \delta_g \end{bmatrix}$$

Finally, all synchronous machine parameters are in per unit values and need to be converted to actual values. Multiplying by the base values for current and voltage results in the following definition for  $\bar{p}_g$  and  $B_g$ :

$$\bar{p}_g = D_g^{-1} \cdot S_g^T \cdot L_g^{-1} \cdot F_g \cdot \bar{\Psi} \cdot I_B \quad (5.79)$$

$$B_g = D_g^{-1} \cdot S_g^T \cdot L_g^{-1} \cdot S_g \cdot \frac{I_B}{D_g^{-1} \cdot U_B} \quad (5.80)$$

The network equation for the generator then becomes:

$$\bar{i}_{net,g} = \bar{p}_g + B_g \bar{u}_{net} \quad (5.81)$$

### Generator scaling

Expressing all generator parameters in per unit values allows for convenient scaling of the generator. After per unit scaling all machine parameters fall within a certain range that can be identified as normal.[20] Furthermore, the interaction between multiple generators is outside the scope of this thesis. The four generators are therefore replaced by a single 18 MVA generator to simplify modelling of the power generation system. For the scaling of the voltage and current, the current vector and admittance matrix determined by Equation 5.79 and Equation 5.80 are used. From these equations it can be concluded that, with respect to the voltage and apparent power,  $\bar{p}_g$  and  $B_g$  can be written as:

$$\bar{p}_g = c1 \cdot \frac{S_B}{U_B} \quad \text{and} \quad B_g = c2 \cdot \frac{S_B}{U_B^2} \quad (5.82)$$

Therefore, scaling the generator voltage by a factor  $sf$  results in the following scaling of  $\bar{p}_g$  and  $B_g$ :

$$U_{new} = sf \cdot U_{old} \rightarrow \begin{cases} \bar{p}_{g,new} = \frac{\bar{p}_{g,old}}{sf} \\ B_{g,new} = \frac{B_{g,old}}{sf^2} \end{cases} \quad (5.83)$$

This will result in a constant power output, but at the desired voltage and current. The current and voltage vectors that are sent to the generator by the network are scaled back to the original voltage and current in a similar way, again maintaining constant power. It can be argued that physical losses might be different resulting from this transformation due to higher currents. This effect, however, is not considered here.

### 5.3.6 Other electric components

The other loads consist of the dredge pumps, side winches, spudpole system and hotel loads. In Section 4.1.1 the electric load on the CSD power generation system is analysed. From this analysis it is concluded that, even though the magnitude of the power demand by the dredge pumps is greater than the power demand of the cutter motors, the cutter motors determine when power is delivered or consumed by the ESS. Therefore, the choice has been made to add the data of all other loads together to be modelled as a single varying electric load on the network.

#### Network connection

Similar to the other models described in this chapter, the other electric loads are connected to the network by a current vector  $\bar{p}$  and admittance matrix  $B$ :

$$\bar{i} = \bar{p} + B\bar{u} \quad (5.84)$$

The other loads are modelled as an impedance on the network, similar to the charging of the ESS in Equation 5.26. The current follows directly from the terminal voltage over the source by impedance  $Z$ , so that  $\bar{p}_{OL}$  and  $B_{OL}$  are defined as:

$$\bar{p}_{OL} = \begin{bmatrix} 0 \\ 0 \end{bmatrix} \quad \text{and} \quad B_{OL} = Z^{-1} \quad (5.85)$$

## 5.4 AC network

The AC network is modeled according to Figure 5.26. Again, the model that is used to simulate the network is created at IHC MTI. This model is described in this section. For this network an admittance matrix  $Y_{bus}$  is defined that relates the sum of all currents through the busses with their voltages. For short transmission lines, the capacitance can be neglected.[35] When all capacitances are chosen as zero, however, the admittance matrix becomes singular and is therefore not invertible. Instead, the capacitance is chosen as  $10^{-8}F$ . [62]

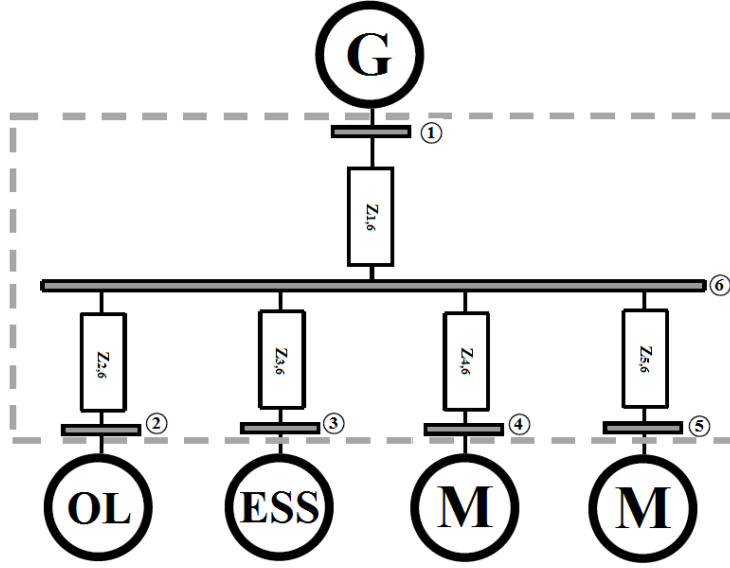


Figure 5.26: Schematic representation of the electric grid

For the network displayed in Figure 5.26 the relation between the voltages and currents can be given by:

$$\begin{bmatrix} I_1 \\ I_2 \\ I_3 \\ I_4 \\ I_5 \\ I_6 \end{bmatrix} = \underbrace{\begin{bmatrix} Z_{11}^{-1} + Z_{16}^{-1} & 0 & 0 & 0 & 0 & 0 & -Z_{16}^{-1} \\ 0 & Z_{22}^{-1} + Z_{26}^{-1} & 0 & 0 & 0 & 0 & -Z_{26}^{-1} \\ 0 & 0 & Z_{33}^{-1} + Z_{36}^{-1} & 0 & 0 & 0 & -Z_{36}^{-1} \\ 0 & 0 & 0 & Z_{44}^{-1} + Z_{46}^{-1} & 0 & 0 & -Z_{46}^{-1} \\ 0 & 0 & 0 & 0 & Z_{55}^{-1} + Z_{56}^{-1} & 0 & -Z_{56}^{-1} \\ -Z_{16}^{-1} & -Z_{26}^{-1} & -Z_{36}^{-1} & -Z_{46}^{-1} & -Z_{56}^{-1} & Z_{66}^{-1} & 0 \end{bmatrix}}_{Y_{bus}} \begin{bmatrix} U_1 \\ U_2 \\ U_3 \\ U_4 \\ U_5 \\ U_6 \end{bmatrix} \quad (5.86)$$

Where

$I_j$  denotes the current through the bus  $j$  in Figure 5.26

$U_j$  denotes the voltages over bus  $j$  in Figure 5.26

$Z_{jj}$  denotes the self-inductance of bus  $j$

$Z_{jk}$  denotes the mutual inductance between bus  $j$  and bus  $k$

The size of  $Y_{bus}$  increases exponentially with the number of busses in the network. To be able to solve the network this matrix is inverted, which costs a lot of computational effort.[62] Therefore, the Kron reduction method is used to reduce the size of the matrix. Using this reduction all busses that are not connected to a source or consumer can be eliminated.[19][34] More details on the Kron reduction can be found in Appendix B. Recalculation of admittance matrix  $Y_{bus}$  can be summarized as:[19]

$$Y_{jk(new)} = Y_{jk} - \frac{Y_{jp}Y_{pk}}{Y_{pp}} \quad \text{for } j, k \neq p \quad (5.87)$$

By applying Equation 5.87 to  $Y_{bus}$  in Equation 5.86 the following new admittance matrix  $Y_{bus}$  is found:

$$Y_{bus} = \begin{bmatrix} Z_{11}^{-1} + Z_{16}^{-1} - \frac{Z_{16}^{-2}}{Z_{66}^{-1}} & -\frac{Z_{16}^{-1}Z_{26}^{-1}}{Z_{66}^{-1}} & -\frac{Z_{16}^{-1}Z_{36}^{-1}}{Z_{66}^{-1}} & -\frac{Z_{16}^{-1}Z_{46}^{-1}}{Z_{66}^{-1}} & -\frac{Z_{16}^{-1}Z_{56}^{-1}}{Z_{66}^{-1}} \\ -\frac{Z_{16}^{-1}Z_{26}^{-1}}{Z_{66}^{-1}} & Z_{22}^{-1} + Z_{26}^{-1} - \frac{Z_{26}^{-2}}{Z_{66}^{-1}} & -\frac{Z_{26}^{-1}Z_{36}^{-1}}{Z_{66}^{-1}} & -\frac{Z_{26}^{-1}Z_{46}^{-1}}{Z_{66}^{-1}} & -\frac{Z_{26}^{-1}Z_{56}^{-1}}{Z_{66}^{-1}} \\ -\frac{Z_{16}^{-1}Z_{36}^{-1}}{Z_{66}^{-1}} & -\frac{Z_{26}^{-1}Z_{36}^{-1}}{Z_{66}^{-1}} & Z_{33}^{-1} + Z_{36}^{-1} - \frac{Z_{36}^{-2}}{Z_{66}^{-1}} & -\frac{Z_{36}^{-1}Z_{46}^{-1}}{Z_{66}^{-1}} & -\frac{Z_{36}^{-1}Z_{56}^{-1}}{Z_{66}^{-1}} \\ -\frac{Z_{16}^{-1}Z_{46}^{-1}}{Z_{66}^{-1}} & -\frac{Z_{26}^{-1}Z_{46}^{-1}}{Z_{66}^{-1}} & -\frac{Z_{36}^{-1}Z_{46}^{-1}}{Z_{66}^{-1}} & Z_{44}^{-1} + Z_{46}^{-1} - \frac{Z_{46}^{-2}}{Z_{66}^{-1}} & -\frac{Z_{46}^{-1}Z_{56}^{-1}}{Z_{66}^{-1}} \\ -\frac{Z_{16}^{-1}Z_{56}^{-1}}{Z_{66}^{-1}} & -\frac{Z_{26}^{-1}Z_{56}^{-1}}{Z_{66}^{-1}} & -\frac{Z_{36}^{-1}Z_{56}^{-1}}{Z_{66}^{-1}} & -\frac{Z_{46}^{-1}Z_{56}^{-1}}{Z_{66}^{-1}} & Z_{55}^{-1} + Z_{56}^{-1} - \frac{Z_{56}^{-2}}{Z_{66}^{-1}} \end{bmatrix}$$

### 5.4.1 Network interface

For each of the electrical component connected to the network the relation between current and voltage is defined by a current vector  $\bar{p}$  and admittance matrix  $B$ . Collecting all the machine equations into a single matrix allows solving of the network interface as shown in Figure 5.27. Note that the electrical frequency  $\omega_e$  is displayed as if it is determined by some external source. The electrical frequency is in fact determined the generator's rotational speed.

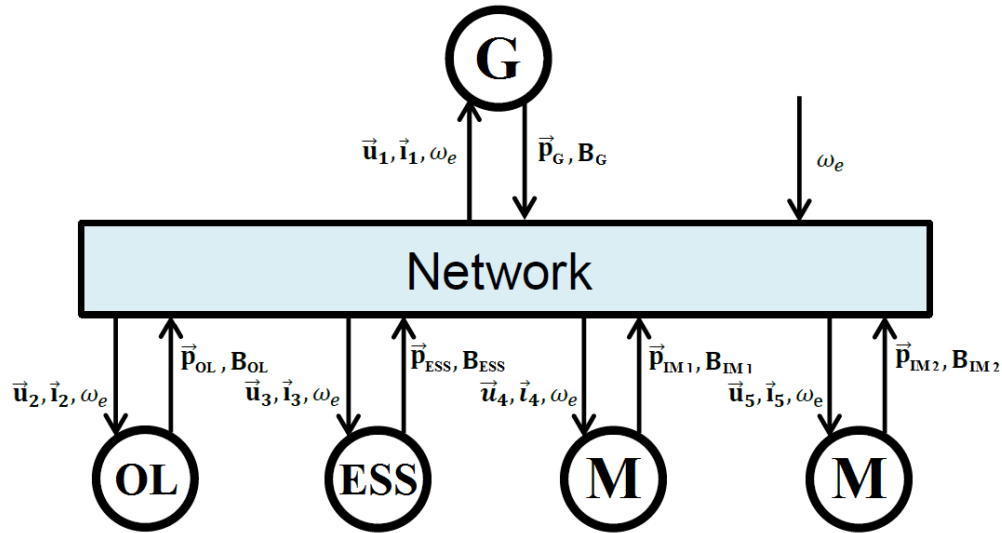


Figure 5.27: Network interface of all sources and consumers

Combining all machine equations results in the following equation for all components:

$$\begin{bmatrix} \vec{i}_1 \\ \vec{i}_2 \\ \vec{i}_3 \\ \vec{i}_4 \\ \vec{i}_5 \end{bmatrix} = \underbrace{\begin{bmatrix} \vec{p}_g \\ \vec{p}_{OL} \\ \vec{p}_{ESS} \\ \vec{p}_{IM1} \\ \vec{p}_{IM2} \end{bmatrix}}_{\vec{p}_{tot}} + \underbrace{\begin{bmatrix} B_g & 0 & 0 & 0 & 0 \\ 0 & B_{OL} & 0 & 0 & 0 \\ 0 & 0 & B_{ESS} & 0 & 0 \\ 0 & 0 & 0 & B_{IM1} & 0 \\ 0 & 0 & 0 & 0 & B_{IM2} \end{bmatrix}}_{B_{tot}} \begin{bmatrix} \vec{u}_1 \\ \vec{u}_2 \\ \vec{u}_3 \\ \vec{u}_4 \\ \vec{u}_5 \end{bmatrix} \quad (5.88)$$

The network equation for the voltages and currents in the busses is given in Equation 5.86. Together with the machine equations in Equation 5.88 the total network interface can be solved so all voltages and currents are known, as shown in the following equation:

$$\begin{bmatrix} \vec{u}_1 & \vec{u}_2 & \vec{u}_3 & \vec{u}_4 & \vec{u}_5 \end{bmatrix}^T = \left( Y_{bus} - B_{tot} \right)^{-1} \cdot \vec{p}_{tot} \quad (5.89)$$

## 5.5 Cutter head

The cutter head is modelled as a varying torque applied to the cutter motors through a cutter shaft and gearbox. The torque from the cutter head is determined by the load from the simulation input data. Figure 5.28 shows an overview of the components connected to the cutter shaft. The mass moment of inertia for the cutter head, cutter shaft and gearbox can be found in Appendix E.

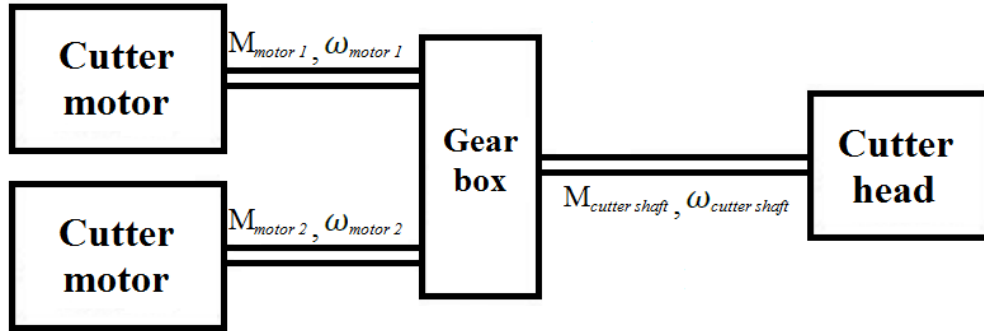


Figure 5.28: Overview of the cutter shaft model components

To maintain their desired rotational speed a counter-acting torque is applied by the cutter motors, given by Equation 5.41. The torque applied by the cutter motors to the cutter shaft then is given by:

$$M_{cs} = \frac{M_{im1} + M_{im2}}{i} \cdot \eta_{GB} \quad (5.90)$$

Where

$i$  is the gear ratio of the gearbox between the cutter motors and the cutter shaft

$\eta_{GB}$  is the efficiency of the gearbox between the cutter motors and the cutter shaft

Similarly, the inertia of the cutter motors as experienced by the cutter shaft is determined by:

$$I = \frac{I_{im1} + I_{im2}}{i^2} \quad (5.91)$$

The rotational speed of the cutter shaft is determined by Equation 5.92. The rotational speed of the cutter shaft can then be divided by the gear ratio of the gearbox between the cutter shaft and cutter motors. The resulting speed is the speed at which the rotor of the electric motors rotate and is fed back to the induction motor models.

$$\omega_{shaft} = \int \alpha dt + \omega_0 = \int \frac{\Sigma M}{\Sigma I} dt + \omega_0 \quad (5.92)$$

Where

$\omega_{shaft}$  is the rotational speed of the cutter shaft in  $rad/s$

$\omega_0$  is the initial rotational speed of the cutter shaft in  $rad/s$

$\alpha$  is the angular acceleration in  $rad/s^2$

$\Sigma M$  is the sum of torques applied to the cutter shaft in  $Nm$

$\Sigma I$  is the total inertia of the cutter shaft in  $kg \cdot m^2$





### 5.6.1 Model verification

#### Generator current

For the verification of the benchmark model data from simulations is compared with measured data. Data is available that contains power demand from all electric consumers listed in Section 2.4 and the static converter connected to the auxiliary switchboard. Furthermore, the corresponding generator currents and main diesel engine powers have been logged. The combined measured currents from the four main generators are compared with the simulated current that results from applying the corresponding power demands. The results from this comparison can be seen in Figure 5.31. It can be seen that, although there is similar trend in both the measured as the simulated current, there is a clear offset. This offset is a result of the lower voltage due to the total harmonic distortion (THD) on the main switchboard caused by the load on the electric network. The total power factor (TPF) resulting from the THD is given by:[61]

$$TPF = \frac{PF}{\sqrt{1 + THD^2}} \quad (5.93)$$

From Equation 5.93 it can be concluded that the TPF is smaller than the original power factor (PF) as result of the THD. Consequently, a larger is current is required for the same amount of power. Secondly, the data from measurements that are used here have a sampling frequency of 3 Hz, while the simulation results in data at a much higher frequency.

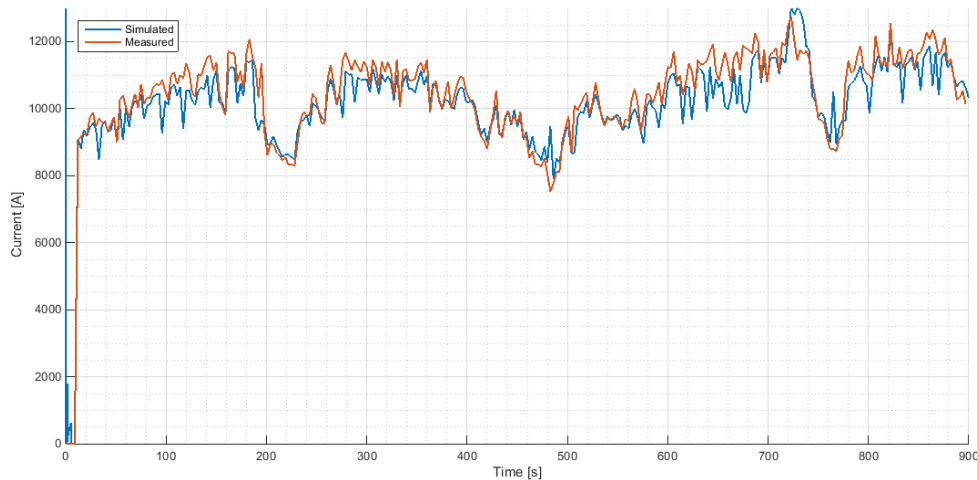


Figure 5.31: Simulated and measured combined generator current, showing a similar trend with an offset

#### Diesel engine power

From Figure 5.31 it can be concluded that the value of the offset is fairly constant. Therefore, a constant power consumption is added to compensate for the THD. The value of the added constant power consumption is chosen by varying the added load in separate simulations and selecting the value that results in the smallest Normalized Root Mean Square Error (NRMSE) between the simulated diesel engine power and the measured diesel engine power. For the calculation of the NRMSE Equation 5.94 is used:

$$NRMSE = \sqrt{\frac{\sum_{t=1}^n (P_m - P_s)^2}{n \cdot \overline{P_m}}} \quad (5.94)$$

Where

$P_m$  is the measured diesel engine power

$P_s$  is the simulated diesel engine power

$n$  is the length of the time vector

Table 5.10 shows the NRMSE corresponding to the varying electric load added to the existing power data. From the table it can be concluded that the smallest NRMSE occurs at an electric load of 1.20 MW. This value is chosen to represent the power demand of the electric consumers missing in the data. The resulting RMSE has a value of 0.0413 and is thought to give the best possible fit between the measured and the simulated power data. With the addition of the constant load the results shown in Figure 5.32 is found.

Table 5.10: Diesel engine power Normalized Root Mean Square Error

Load [MW]	NRMSE [-]	Load [MW]	NRMSE [-]	Load [MW]	NRMSE [-]
0.10	0.0831	0.60	0.0580	1.10	0.0459
0.20	0.0773	0.70	0.0539	1.20	<b>0.0413</b>
0.30	0.0722	0.80	0.0503	1.30	0.0430
0.40	0.0672	0.90	0.0462	1.40	0.0469
0.50	0.0624	1.00	0.0463	1.50	0.0525

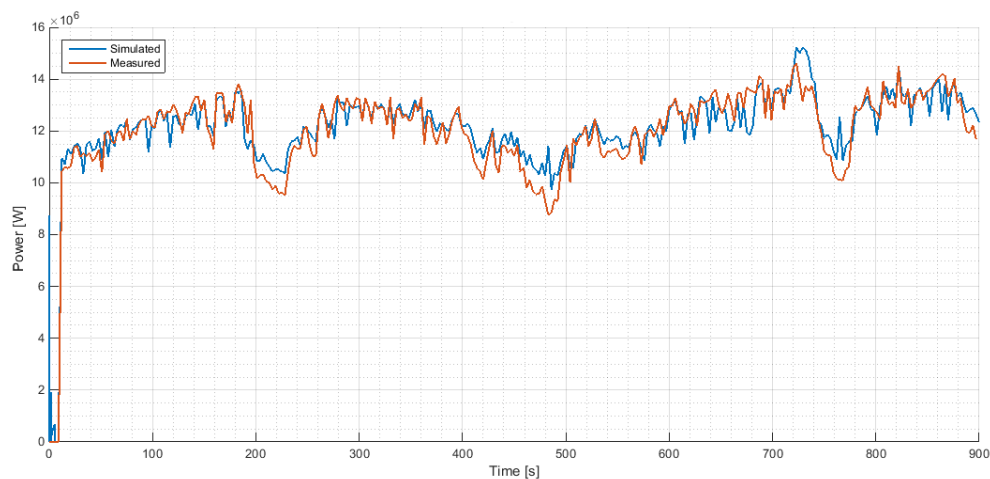


Figure 5.32: Fitted simulated and measured diesel engine powers

A second simulation is done using different data to verify that the added constant power is valid for other data. The results of this verification is shown in Figure 5.33. For the diesel engine powers shown in the figure a NRMSE of 0.0648 is found.

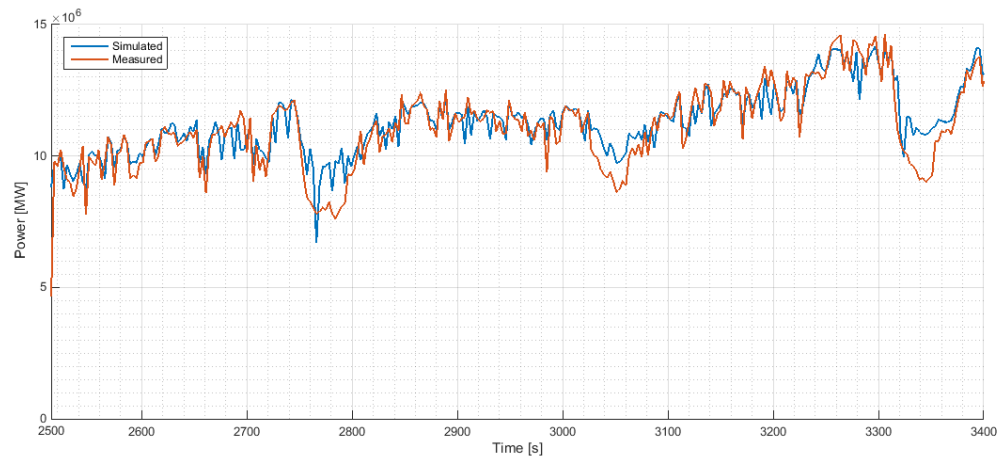


Figure 5.33: Verification of simulated and measured combined main diesel engine power

# Chapter 6

## Simulations

In this chapter the relevant simulations that have been performed are described. For each of the simulations the relevant input is listed followed by the simulation results. The simulation are divided into two separate categories: Diesel engines and dual fuel engines. For all sets of simulations the details of the first simulation is described and analyses in this chapter. An overview of all simulations and results is given in Appendix F.6.

The CSD driveline as described in Section 2.4 has been modeled according to the models described in Chapter 5. Separate driveline models have been created for simulations where an ESS has been added, one containing the supercapacitor model and one containing the flywheel ESS model. Both the ESS models have been modeled according to the description in Chapter 5. For the simulations with dual fuel engines the main diesel engines in the models have been replaced by dual fuel engines. For each of the simulations a random 30 minute part of the cutter data is used as input. This sample is taken from a month of dredging operation data and can be seen in Appendix F.6. As can be seen, the data shows a repetitive pattern and therefore each sample is assumed to be a good representation of a typical load on the CSD.

### 6.1 Simulation 1 - Diesel engines

For Simulation 1 four separate simulations have been performed:

- Simulation 1.1 - Benchmark simulation of the original CSD driveline without energy storage
- Simulation 1.2 - Original driveline with added flywheel energy storage
- Simulation 1.3 - Original driveline with added supercapacitor energy storage
- Simulation 1.4 - Alternate engine configuration with three smaller engines providing the same total amount of power, but with one engine switched off.

#### 6.1.1 Load

The load input used for the simulation is 30 minutes of data from May 5th, 2016, 19:00 to 19:30. The data can be seen in Figure 6.1. The blue line indicates the electric load consisting of the dredge pumps, side winches, and other electric loads. The red line indicates the total torque on the cutter head.

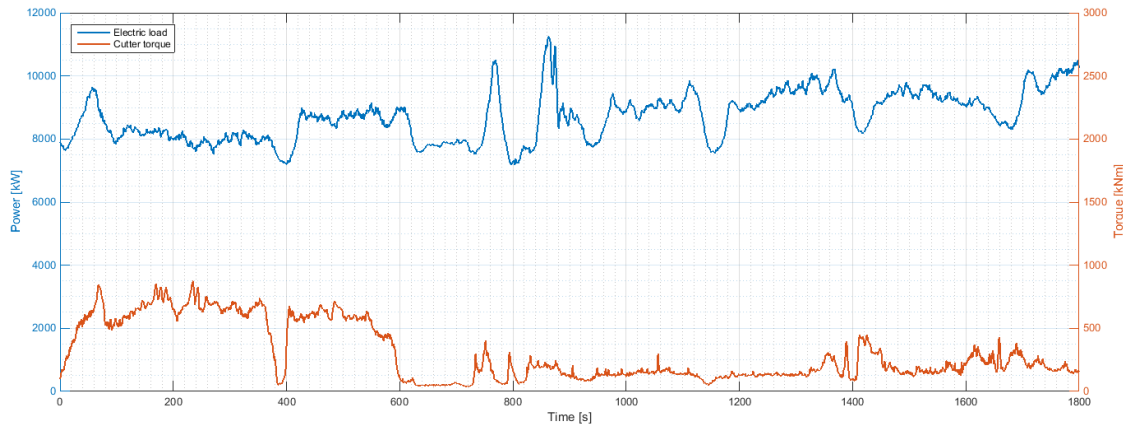


Figure 6.1: Input for Simulation 1. Data of May 5th, 2016, 19:00 - 19:30

### 6.1.2 Maximum load increase

For the simulations with diesel engines maximum normal loading conditions for a preheated engine are assumed. This means that for the diesel engines the ramp for short loading in Figure 4.5 is used as maximum increase in load, which corresponds to a maximum increase of  $180 \text{ kW/s}$  per diesel engine.

### 6.1.3 Power and energy requirements

Based on the maximum load increase defined above the methodology described in Section 4.1 is used. The resulting minimum power and energy are  $1.91 \text{ MW}$  and  $7.53 \text{ MJ}$ , respectively. The ESS configuration following from these requirements are shown in Table 6.1. It can be seen that for the supercapacitor ESS the amount of energy that can be stored determines the configuration, while for the flywheel ESS this is determined by the amount of required power.

Table 6.1: Energy storage sizing for diesel engine simulations

Energy storage system	Configuration	Peak power	Energy capacity
Supercapacitors + Diesel	3 parallel branches	$3.32 \text{ MW}$	$8.66 \text{ MJ}$
Flywheels + Diesel	7 modules	$2.1 \text{ MW}$	$100.8 \text{ MJ}$

### 6.1.4 ESS size and weight

Table 6.2: Energy storage system volume and weight

Energy storage system	ESS volume [ $m^3$ ]	ESS weight [ $kg$ ]
24 supercapacitor modules + 3 converters	1.11	810
7 Flywheels modules	1.92	2625

### 6.1.5 Results

#### Simulation 1.1 - Original driveline benchmark

For Simulation 1.1 the original CSD driveline is simulated and is used as benchmark simulation. The load on the diesel engines and the fuel consumption of the other simulations are compared with the results of Simulation 1.1. Figure 6.2 shows the variation of the load experienced by the diesel engines. The dashed line

indicates the maximum load increase. It should be noted here that the load variation in Figure 6.2 shows the variation that is applied to the power generation system. During some of the simulations, it was found that the PID controller which controls the generator voltage on rare occasions resulted in undesired small fluctuations in generator voltage. As a result, generator torque fluctuations occurred that are not a result of an increase in electric load. Because it proved difficult to distinguish these fluctuations, the load fluctuations as shown in the figure are considered, as these are the actual load fluctuations as experienced by the diesel engines.

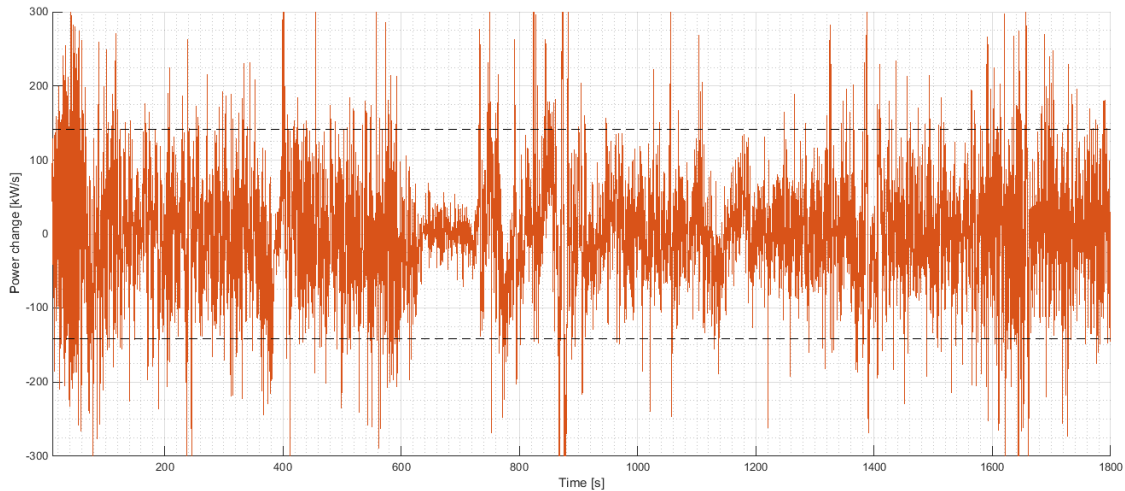


Figure 6.2: Simulation 1.1 - Load variation on the diesel engines and the maximum load increase

Figure 6.3 shows a cumulative distribution function of the load variation on the diesel engines. In the figure, it can be seen that roughly 85% of the load variation is within the defined limit.

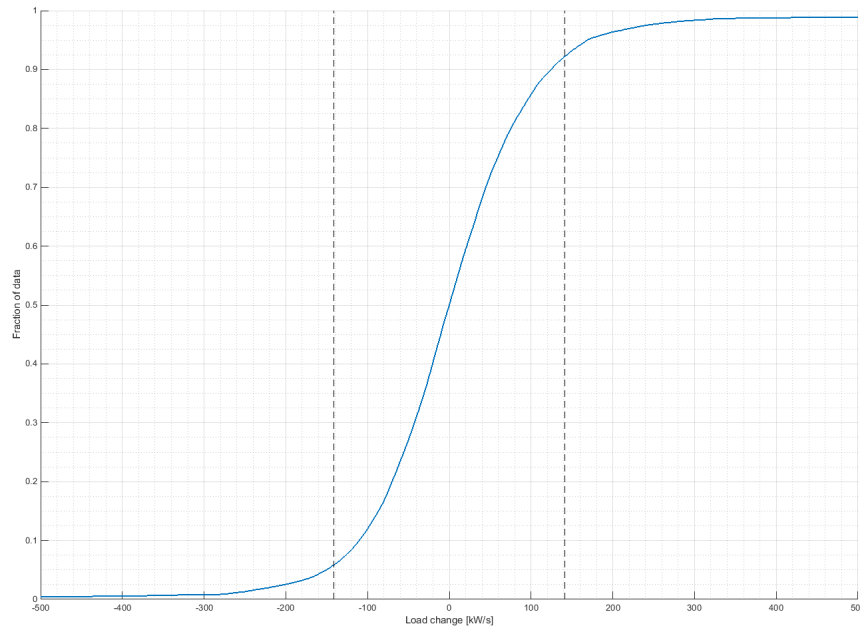


Figure 6.3: Simulation 1.1 - Cumulative distribution function of load variation and maximum allowed change

Figure 6.4 shows the load on each of the main diesel engines. The dashed line in the figure indicates the amount of power that corresponds with a MCR of 85%. It can be seen that the required power of each diesel

engine is around 50% MCR. The amount of fuel consumed during the 30 minute simulation equals 916.29 kg MDO.

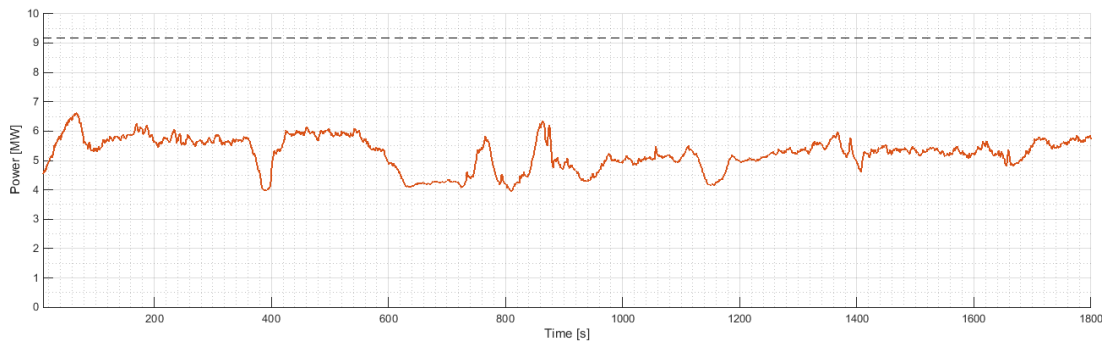


Figure 6.4: Simulation 1.1 - Load on a single diesel engine and 85% MCR line

### Simulation 1.2 - Original driveline with flywheel ESS

For Simulation 1.2 a flywheel ESS has been added to the original CSD driveline. The specifications of the flywheel ESS can be seen in Table 6.1. The flywheel ESS has an initial state of charge of 0.9. Figure 6.5 shows the active power demand, generator active power and flywheel ESS power. Figure 6.8 shows an enlarged section to give a better picture of the effect of the flywheel ESS.

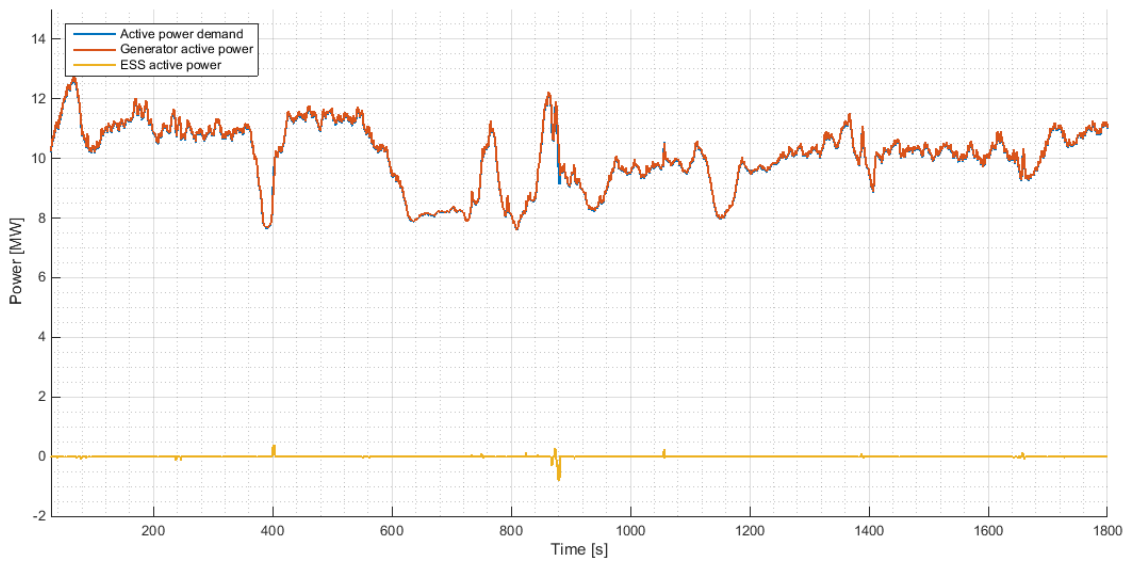


Figure 6.5: Simulation 1.2 - Active power demand, generator active power, and ESS active power

The load variation experienced by the diesel engines is shown in Figure 6.6. The dashed line indicates the maximum allowed load increase. It can be seen that the maximum load increase and decrease is no longer exceeded.

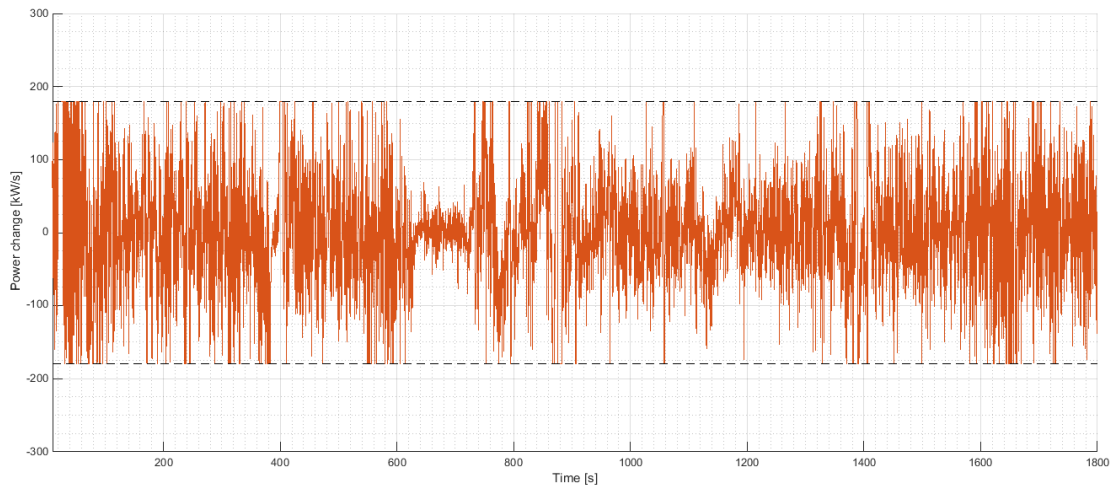


Figure 6.6: Simulation 1.2 - Load variation on the diesel engines and the maximum load increase

The stored energy and the rotational speed of the flywheel ESS are displayed in Figure 6.7. The state of charge at the end of the simulation equals 0.823 and does not change significantly during the simulation, meaning the ESS is not used very often. In the figure it can be seen that the predominant source of energy loss is the self-discharge of the flywheel ESS. A similar image is shown in Figure 6.5, where it is clear that there are only a few instances where the ESS is charging or discharging. A close-up of the ESS power is shown in Figure 6.9. The maximum charge and discharge power are around  $800\text{ kW}$  and  $400\text{ kW}$ , respectively. The amount of fuel consumed during the 30 minute simulation equals  $916.41\text{ kg}$  MDO.

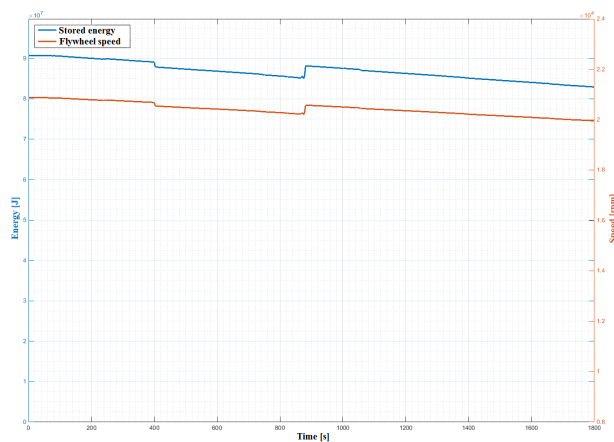


Figure 6.7: Simulation 1.2 - Flywheel ESS stored energy and flywheel rotational speed

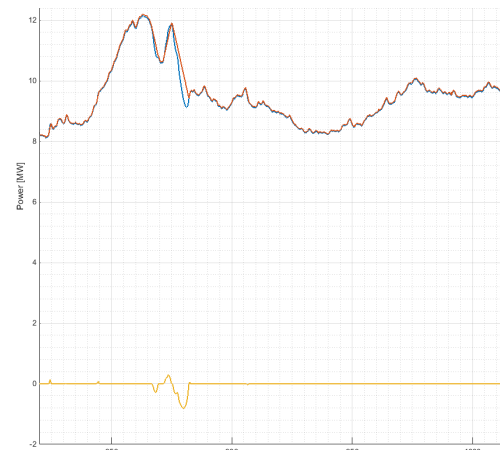


Figure 6.8: Simulation 1.2 - Close-up of Figure 6.5

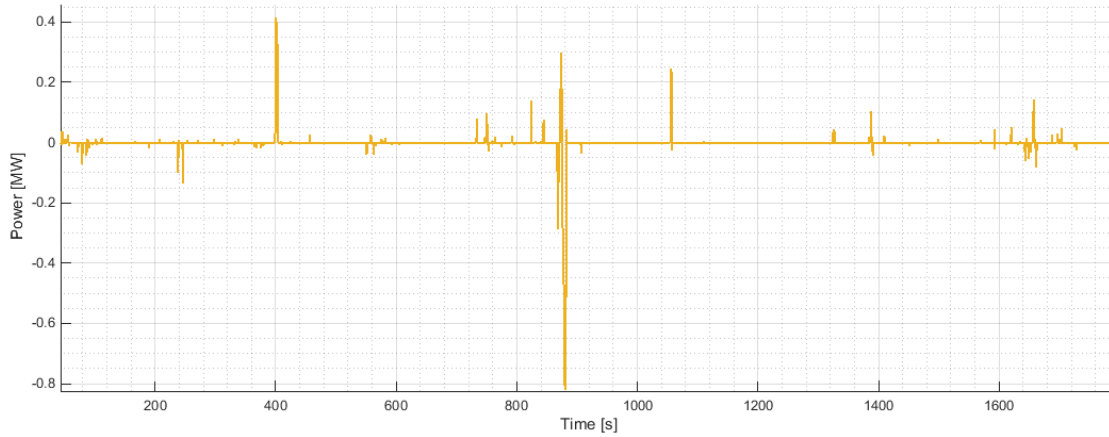


Figure 6.9: Simulation 1.3 - Close-up of ESS power from Figure 6.6

### Simulation 1.3 - Original driveline with supercapacitor ESS

For Simulation 1.3 a supercapacitor ESS has been added to the original CSD driveline. The specifications of the supercapacitor ESS can be seen in Table 6.1. The supercapacitor ESS has an initial state of charge of 0.9. Figure 6.10 shows the active power demand, generator active power and the supercapacitor ESS power. The load variation experienced by the diesel engines is shown in Figure 6.11. The dashed line indicates the maximum allowed load increase. As can be seen in the figure, the load variation stays within the limit except for one instance at around 900 seconds.

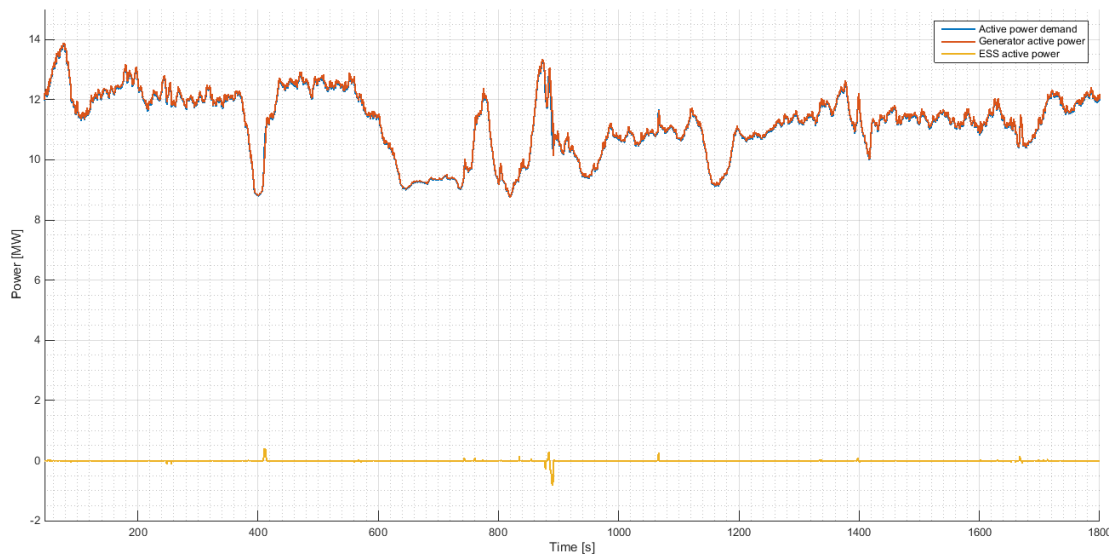


Figure 6.10: Simulation 1.3 - Active power demand, generator active power, and ESS active power

Similar to Simulation 1.2, there is very little power delivered to and by the ESS. This is to expected, since the limit for the load increase per unit of time is the same as for Simulation 1.2. The lowest state of charge during the simulation is 0.787. The total progress of the state of charge can be seen in Figure 6.12. The supercapacitor current is shown in Figure 6.13. To avoid excessive heat development the current during charging and discharging of the supercapacitor ESS should stay below the current limit shown in Table 5.2. As can be seen in the figure, the current stays well below the limit. The amount of fuel consumed during the 30 minute simulation equals 916.36 *kg* MDO.

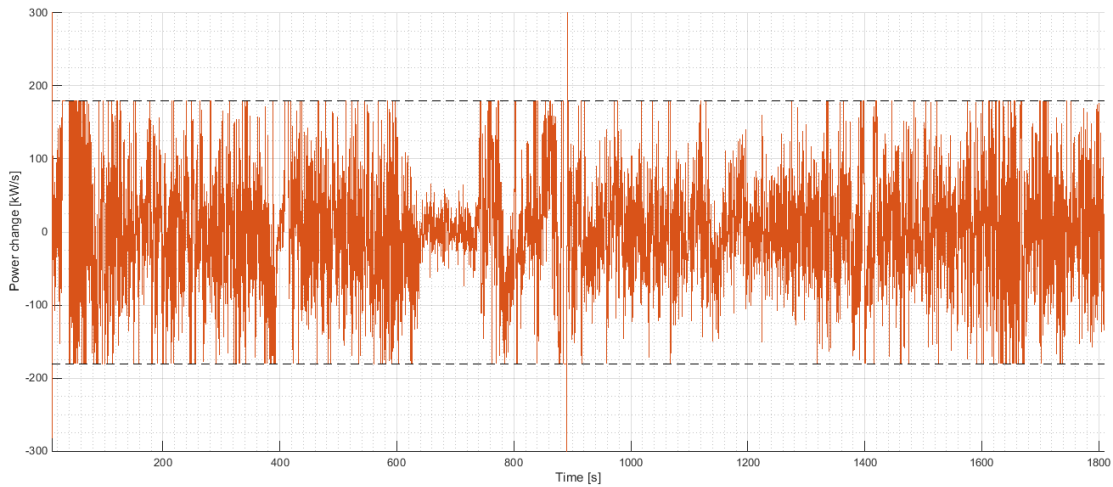


Figure 6.11: Simulation 1.3 - Load variation on the diesel engines and the maximum load increase

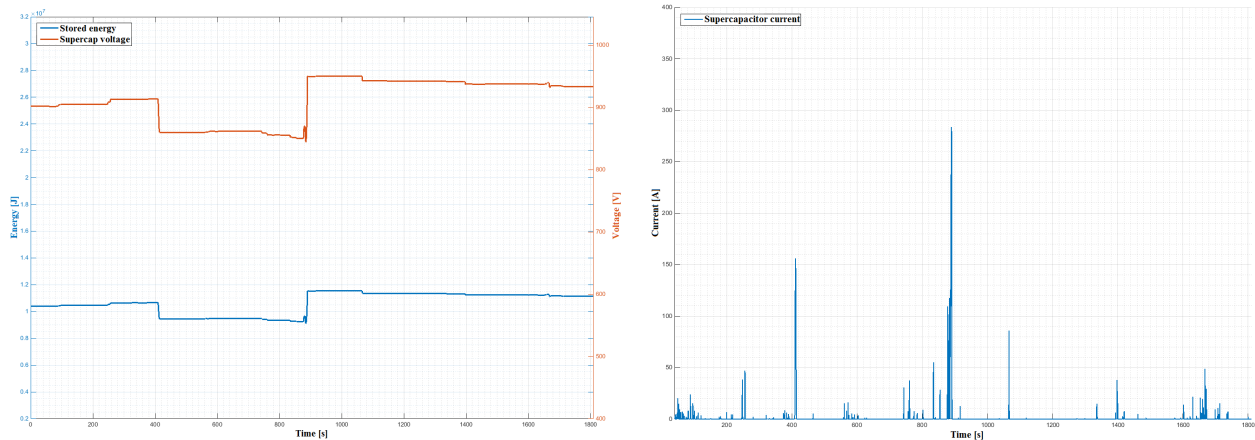


Figure 6.12: Simulation 1.3 - Supercapacitor ESS stored energy and voltage

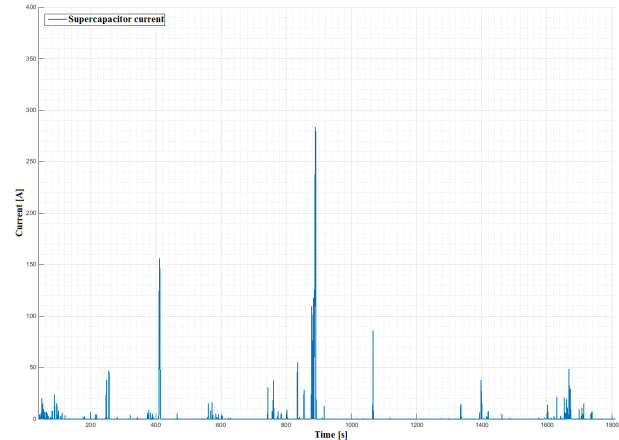


Figure 6.13: Simulation 1.3 - Supercapacitor (dis)charge current

### Simulation 1.4 - Alternate engine configuration

For Simulation 1.4 the two 9 cylinder main diesel engines have been replaced by three 6 cylinder diesel engines of the same type. Furthermore, one of the three diesel engines has been disabled resulting in a higher load on the two remaining diesel engines. Comparing Figure 6.14 to the original situation as displayed in Figure 6.4 shows that with 3 smaller diesel engines, the diesel engines operate closer to 85% MCR. The amount of fuel consumed during the 30 minute simulation equals 904.96 *kg* MDO.

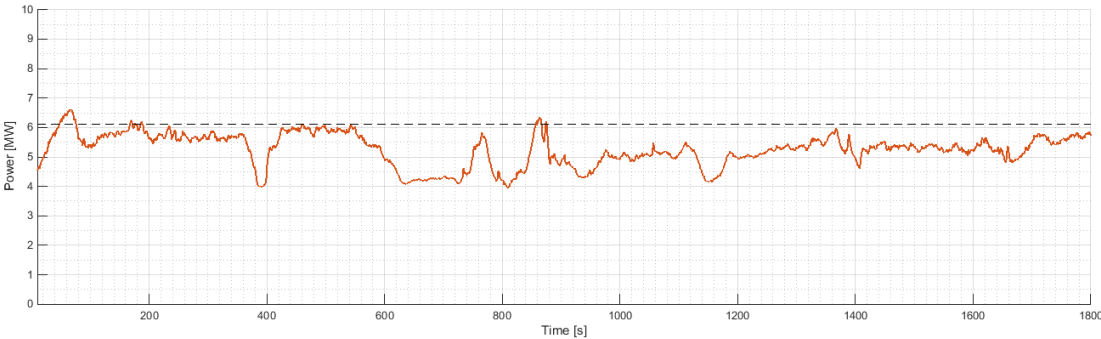


Figure 6.14: Simulation 1.4 - Load on a single diesel engine and 85% MCR line

## 6.2 Simulation 2 - Dual fuel engines

For simulation 2 three separate simulations have been performed:

- Simulation 2.1 - Dual fuel engines
- Simulation 2.2 - Dual fuel engines with added flywheel energy storage
- Simulation 2.3 - Dual fuel engines with added supercapacitor energy storage

### 6.2.1 Load

The load input used for the simulation is the same as the input used for Simulation 1, 30 minutes of data from May 5th, 2016, 19:00 to 19:30. The data can be seen in Figure 6.1.

### 6.2.2 Maximum load increase

For the simulations with dual fuel engines maximum normal loading conditions for a preheated engine are assumed. This means that for the dual fuel engines the left ramp in Figure 3.5 is used as maximum increase in load, which corresponds to a maximum increase of  $93 \text{ kW/s}$  per dual fuel engine.

### 6.2.3 Power and energy requirements

Based on the maximum load increase defined above the methodology described in Section 4.1 is used. The resulting minimum power and energy are  $2.54 \text{ MW}$  and  $21.76 \text{ MJ}$ , respectively. The ESS configuration following from these requirements are shown in Table 6.3. It can be seen that for the supercapacitor ESS the amount of energy that can be stored determines the configuration, while for the flywheel ESS this is determined by the amount of required power.

Table 6.3: Energy storage sizing for diesel engine simulations

Energy storage system	Configuration	Peak power	Energy capacity
Supercapacitors + Dual fuel	8 parallel branches	$8.85 \text{ MW}$	$23.10 \text{ MJ}$
Flywheels + Dual fuel	9 modules	$2.7 \text{ MW}$	$129.6 \text{ MJ}$

### 6.2.4 ESS size and weight

Table 6.4: Energy storage system volume and weight

Energy storage system	ESS volume [ $m^3$ ]	ESS weight [ $kg$ ]
64 supercapacitor modules + 8 converters	2.96	2160
9 Flywheels modules	2.47	3375

### 6.2.5 Results

#### Simulation 2.1 - Dual fuel engines

For Simulation 2.1 the main diesel engines have been replaced by dual fuel engines. Exceeding of the maximum allowed load increase or decrease results in switching to combustion of diesel fuel. The resulting load

change of Simulation 2.1 will be used to evaluate the performance of the ESS in Simulation 2.2 and Simulation 2.3.

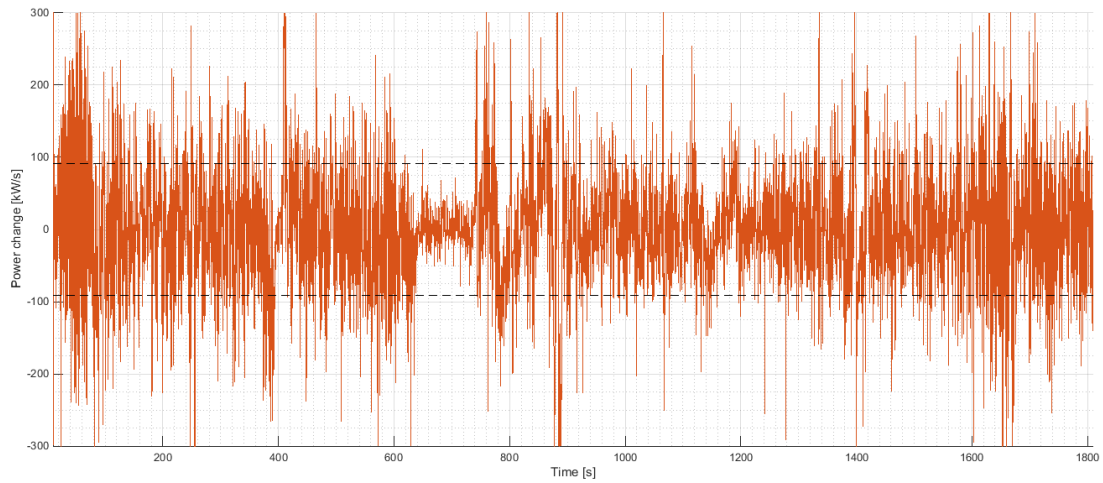


Figure 6.15: Simulation 2.1 - Load variation on the dual fuel engines and the maximum load change

Figure 6.15 shows the variation of power experienced by each of the dual fuel engines. The dashed lines indicate the maximum allowed load increase or decrease before switching from combustion of LNG to diesel. Figure 6.16 shows the cumulative distribution function of the load variation on the dual fuel engines. In the figure it can be seen that around 30% of the data exceeds the limit. The amount of fuel consumed during the 30 minute simulation equals 861.68 *kg* LNG.

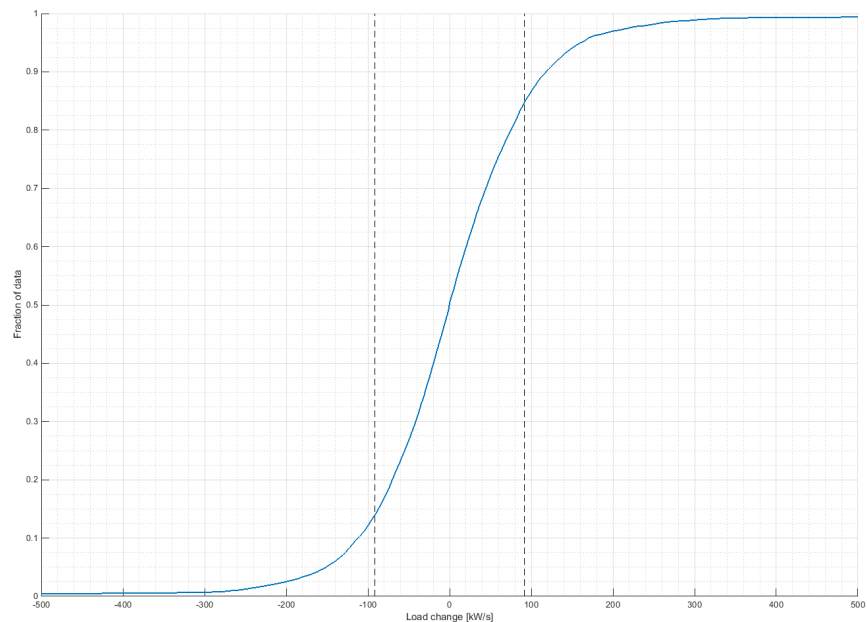


Figure 6.16: Simulation 2.1 - Cumulative distribution function of load variation and maximum allowed change

### Simulation 2.2 - Dual fuel engines with flywheel ESS

For Simulation 2.2 a flywheel ESS has been added to the driveline with dual fuel engines. The specifications of the flywheel ESS can be seen in Table 6.3. The flywheel ESS has an initial state of charge of 0.9. Figure

6.17 shows the active power demand, generator active power, and flywheel ESS power. Figure 6.20 shows an enlarged section to give a better picture of the effect of the flywheel ESS.

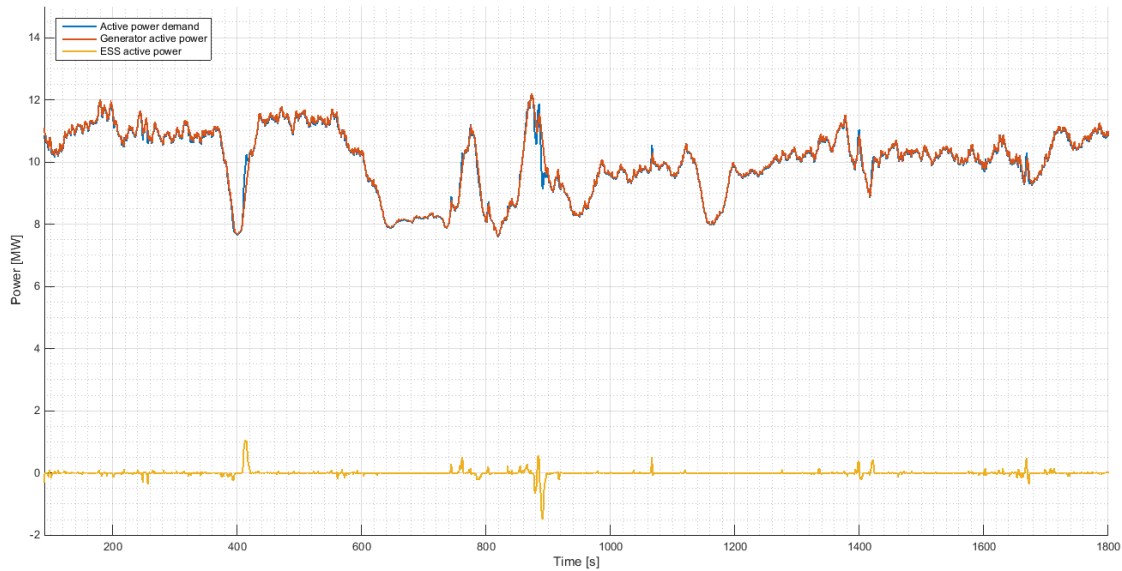


Figure 6.17: Simulation 2.2 - Active power demand, generator active power, and ESS active power

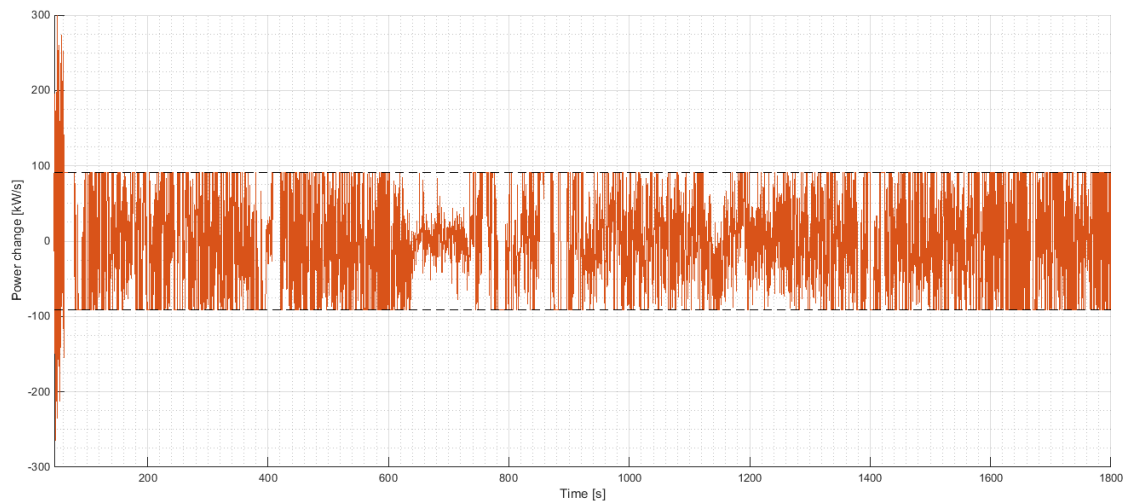


Figure 6.18: Simulation 2.2 - Load variation on the dual fuel engines and the maximum load change

The load variation experienced by the dual fuel engines is shown in Figure 6.18. The dashed line indicates the maximum allowed load change. The load increase that exceeds the limit at the start of the simulation results from inactivity of the ESS model. The stored energy and the rotational speed of the flywheel ESS are displayed in Figure 6.19. The state of charge at the end of the simulation equals 0.798 and does not change significantly during the simulation. A close-up of the ESS power is shown in Figure 6.21. The maximum charge and discharge power are around 1.5 MW and 1.1 MW, respectively. In contrast to Simulation 1.2, around half the maximum power that can be delivered by the flywheel ESS is necessary to prevent switching to combustion of diesel. The amount of fuel consumed during the 30 minute simulation equals 861.74 kg LNG. Furthermore, 10.8 kg of pilot fuel is consumed. The amount of pilot fuel consumed is the same for all dual fuel simulations described here.

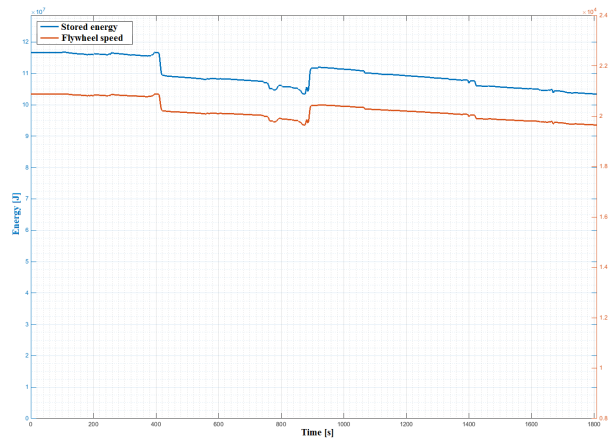


Figure 6.19: Simulation 2.2 - Flywheel ESS stored energy and flywheel rotational speed

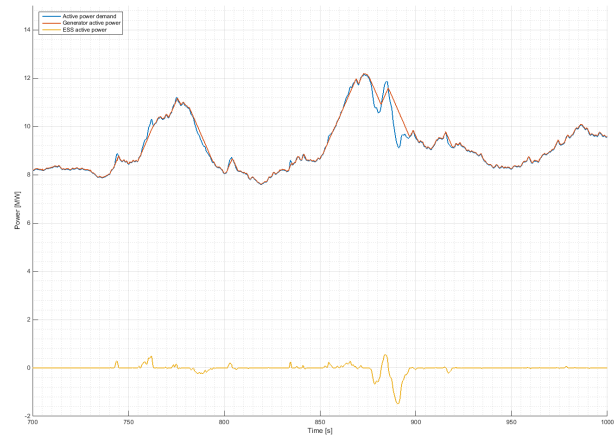


Figure 6.20: Simulation 2.2 - Close-up of Figure 6.17

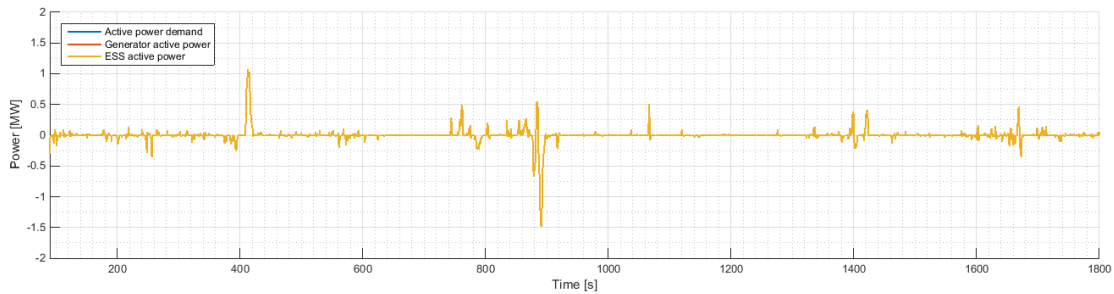


Figure 6.21: Simulation 2.2 - Close-up of ESS power from Figure 6.17

### Simulation 2.3 - Dual fuel engines with supercapacitor ESS

For Simulation 2.3 a supercapacitor ESS has been added to the driveline with dual fuel engines. The specifications of the supercapacitor ESS can be seen in Table 6.3. The supercapacitor ESS has an initial state of charge of 0.9. Figure 6.22 shows the active power demand, generator active power, and the supercapacitor ESS power. The load variation is experienced by the dual fuel engines is shown in Figure 6.23. The dashed lines indicate the maximum allowed load change. As can be seen in the figure, the load variation stays within the limit.

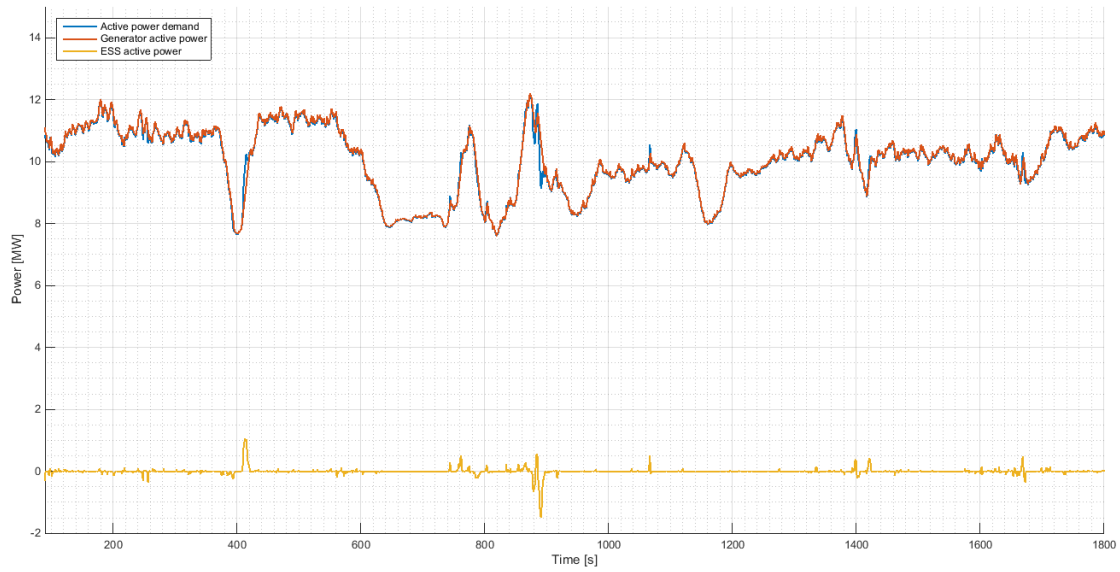


Figure 6.22: Simulation 2.3 - Active power demand, generator active power, and ESS active power

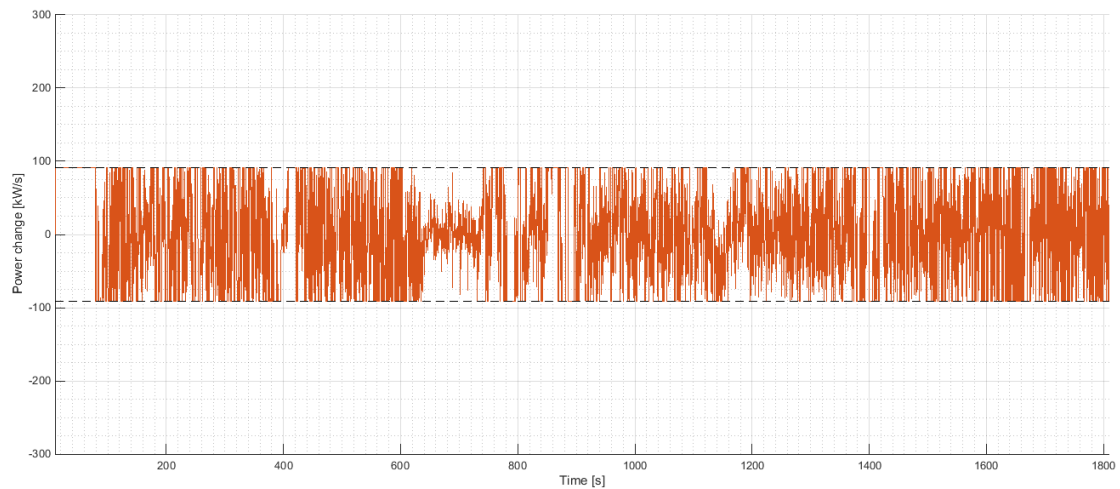


Figure 6.23: Simulation 2.3 - Load variation on the dual fuel engine and maximum load change

Figure 6.24 shows the supercapacitor ESS voltage and state of charge. The lowest state of charge during the simulation is 0.645. The current during charging and discharging is shown in Figure 6.25. As can be seen in the figure, the current stays below the limit given in Table 5.2. The amount of fuel consumed during the 30 minute simulation equals 861.68 *kg* LNG.

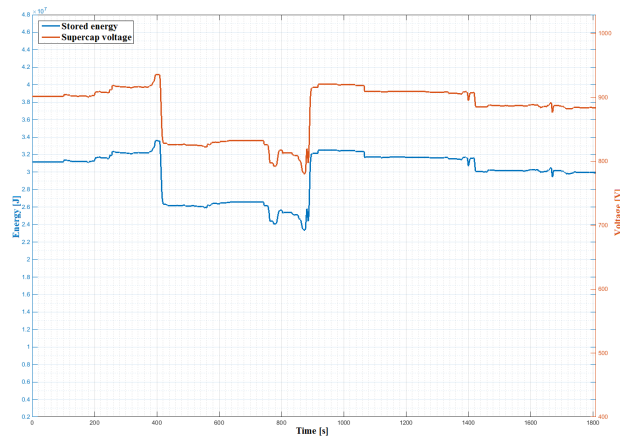


Figure 6.24: Simulation 2.3 - Supercapacitor ESS stored energy and voltage

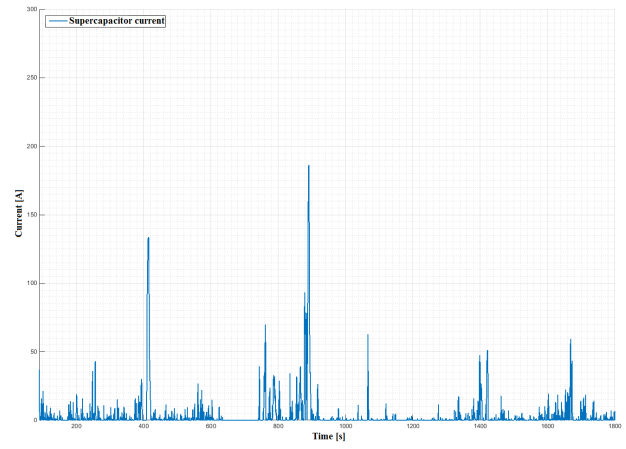


Figure 6.25: Simulation 2.3 - Supercapacitor (dis)charge current

# Chapter 7

## Conclusions and recommendations

In Chapter 6 the simulations and simulation results are described. A benchmark model of the original CSD driveline is created to which the proposed alternate driveline configurations are compared. In this chapter the conclusions that are drawn from the results are described followed by recommendations that follow from these conclusions.

### 7.1 Conclusions

With the conclusions drawn in this chapter an answer is given to the research question stated in Chapter 1. The research question will be answered separately for driveline configurations with diesel engines and dual fuel engines. The research question is used as a summary of the research objective and is states as:

*Is it beneficial to add an energy storage system to the power generation system of a cutter suction dredger to reduce the load fluctuations on the main engines in order to smoothen power demand on the power generation system?*

#### 7.1.1 Diesel engines

##### Load variation

For the CSD driveline with two main diesel engines a minimum power of 1.91 *MW* and a minimum energy storage capacity of 7.53 *MJ* is determined to avoid exceeding of normal maximum loading limit. Analysis of the load on the CSD driveline during a period of one month showed that 98% of the load fluctuation is within the maximum loading limit. It should be noted here this percentage includes moments where no dredging took place so the actual percentage during dredging operation is expected to be lower. This can also be seen in the simulation results, where the percentage of load variation that are within the loading limit ranges from 73.5 % to 95.9%. In all simulations the addition of an ESS increased this percentage to over 99%, with the exception of Simulation 7.3. In this simulation the amount of energy stored in the supercapacitor ESS was insufficient to be able to reduce the load fluctuation during the full simulation. The maximum amount of power supplied by the ESS is far below the maximum available power in all simulations, except for Simulation 7.2 where up to 80% of the maximum ESS power is used. Comparing the load input for Simulation 7 and Simulation 8 to other load inputs shows that the load variation exceeding the limit in this dataset is far greater than the average of the other data, suggesting that in average conditions an ESS with lower power and energy would suffice.

## Fuel consumption

The addition of an ESS shows no reduction in the amount of fuel that is consumed. In fact, in most simulations the fuel consumption is slightly higher with an increase of less than 1% with the addition of an ESS due to the losses in the ESS and the initial energy stored in the ESS. It is therefore concluded that reduction of the load fluctuations on the diesel engines has no beneficial effect on fuel consumption. For the simulation where the two main diesel engines are replaced by three smaller engines a reduction in fuel consumption of 1 to 4% is found. This reduction is smaller than expected and results from the minor difference in SFC at an MCR above 60%. It is therefore concluded that in terms of fuel consumption it is beneficial to have several smaller engines driving the power generation system so that the average load on the main engines can be better adapted to the power demand.

## Cost analysis

A summary of the cost related to the diesel engine simulations is shown in Table 7.1. The range of fuel and cost indicate the minimum and maximum values found in the simulation results.

Table 7.1: Diesel engine simulation cost analysis

Simulation	Fuel cons'd [ <i>kg/hour</i> ]	Fuel cons'd [€/hour]	ESS cost [€]
Diesel engines only	1134 - 1832	549.24 - 842.72	-
Flywheels + Diesel engines	1134 - 1832	549.24 - 842.72	217,000
Supercapacitors + Diesel engines	1134 - 1832	549.24 - 842.72	139,800

## ESS cycle life

Based on the maximum amount of lifetime cycles stated in Section 4.5 it is concluded that the ESS cycle life is not an issue. When considering the highest number of charge and discharge cycles found during simulations and assuming that number for the amount of average cycles per half hour, an expected lifetime of over 7 years is found for the supercapacitor ESS and over 19 years for the flywheel ESS. This estimation is based on continuous dredging operation and is therefore unrealistic. However, even with this conservative and unrealistic use of the ESS, the estimation results in high values for the expected ESS lifetime.

### 7.1.2 Dual fuel engines

#### Load variation

For the CSD driveline with dual fuel engines running on LNG a minimum power of 2.54 MW and a minimum engine storage capacity of 21.76 MJ is determined to avoid exceeding of the maximum loading capacity in gas mode. Above this limit the dual fuel engine switches from combustion of LNG to diesel, which is to be prevented. From the analysis of the load on the CSD driveline over a period of one month it is found that 88% of the load fluctuation is within the maximum loading limit. Again, it should be noted that this percentage includes moments where no dredging took place. For the CSD driveline with dual fuel engines and no ESS all simulations show that undesired switching to combustion of diesel fuel is inevitable. In the simulations where a flywheel ESS is added to the CSD driveline the percentage of load fluctuation within the engine limit is increased to at least 99%. However, the maximum amount of power delivered by the ESS is again far below the maximum available ESS power. Furthermore, the state of charge never drops below roughly 0.60, meaning an ESS with lower power and energy would suffice. For the supercapacitor ESS the percentage of load variations exceeding the limit was increased to at least 98% at worst.

Due to the limited energy storage capacity the supercapacitor ESS is unable to reduce load fluctuation during all simulations, both when increasing or decreasing of the engine load. For the exceeding of ramp-down limit no problem is expected. This limit was chosen to be equal to the ramp-up limit to ensure a balanced charging and discharging of the ESS. Furthermore, installation of a waste-gate on the dual fuel engines will reduce the air excess ratio to avoid misfires when the loading is decreased. Figure 7.1 shows a part of the load variation from Simulation 4.3. This simulation showed the highest percentage of load variation exceeding the limit.

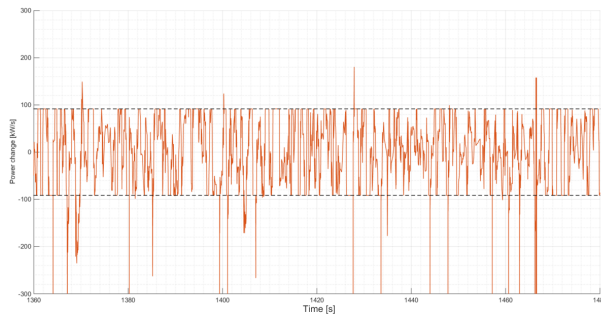


Figure 7.1: Part of load variation from Simulation 4.3 where exceeding of the loading limit occurred

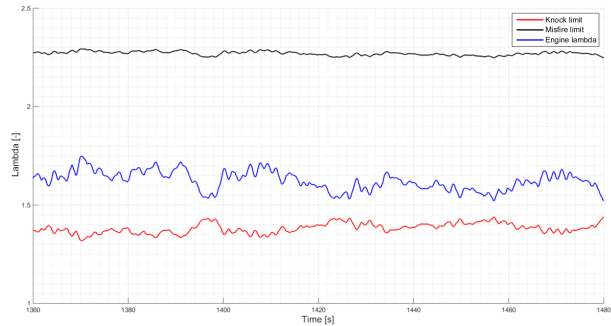


Figure 7.2: Air excess ratio, knock limit and misfire limit for Simulation 4.3

Figure 7.2 shows the air excess ratio corresponding to the load variation shown in Figure 7.1. The knock limit and misfire limit are indicated by the red and black line, respectively. In the figure it can be seen that during exceeding of the loading limit the air excess ratio, indicated by the blue line in Figure 7.2, stays between the knock and misfire limits. Therefore, it is concluded that no switching to combustion of diesel in dual fuel engines will occur during dredging operation.

## Fuel consumption

Similar to the simulations with diesel engines, there is very little difference between the fuel consumption of dual fuel engines power-generation system with and without ESS. However, since the addition of an ESS allows continuous combustion of LNG there is a significant reduction in the cost related to the fuel consumption compared to the original CSD driveline with diesel engines. Based on the fuel consumed during simulation a cost reduction of 17 to 33 percent is realized when LNG is used as fuel during dredging operation instead of MDO.

## Cost analysis

Table 7.2: Dual fuel engine simulation cost analysis

Simulation	Fuel cons'd [kg/hour]	Fuel cons'd [€/hour]	ESS cost [€]
Dual fuel only	1378 - 1672	453.66 - 565.06	-
Flywheels + Dual fuel	1378 - 1672	453.66 - 565.06	279,000
Supercapacitors + Dual fuel	1378 - 1672	453.66 - 565.06	419,400

## ESS cycle life

Based on the maximum amount of lifetime cycles stated in Section 4.5 it is concluded that the ESS cycle life is not an issue. When considering the highest number of charge and discharge cycles found during simulations and assuming that number for the amount of average cycles per half hour, an expected lifetime of

over 4 years is found for the supercapacitor ESS and over 9 years for the flywheel ESS. This estimation is based on continuous dredging operation and is therefore unrealistic. However, even with this conservative and unrealistic use of the ESS, the estimation results in high values for the expected ESS lifetime.

### 7.1.3 Final conclusion

From the conclusions that are drawn for the proposed configurations in this chapter an overall conclusion is formulated to answer the research question. The conclusions stated above are summarized as:

- For the power generation system with diesel engines without energy storage an average value of 91% is found for the percentage of load variations within the loading limit. The addition of an ESS increased this percentage to at least 99%.
- For the power generation system with dual fuel engines without energy storage an average value of 75% is found for the percentage of load variations within the loading limit. The addition of an ESS increased this percentage to at least 98%.
- From Figure 7.2 it is concluded that the lowest percentage of load variation within the engine limit still did not result in switching to combustion of diesel fuel.
- By continuously running on LNG instead of MDO, a reduction up to 33% in fuel cost is achieved.

Considering the research question and the summary given above, it is concluded that it is beneficial to add an ESS to the power generation system to reduce the load fluctuations on the main engines in order to smoothen power demand on the power generation system. Both the flywheel ESS and supercapacitor ESS proved capable of reducing the load variation to a similar extend.

## 7.2 Discussion and Recommendations

### 7.2.1 Discussion

For this research part of the electrical network of a CSD has been modeled. The way in which the electrical network is modeled requires a specific network interface (e.g. current vectors and admittance matrices) for all components connected to the AC network model so that the components can not be properly used as standalone models. As a result a very detailed model is created using existing component models including network voltages, currents and electrical frequencies. Consequently, the energy storage models have to be modeled in a similar way. While the currents allowed for validation of the benchmark model by comparison with measured current data, similar results may have been achieved using a simpler model.

Secondly, in the final conclusion it is stated that both the flywheel ESS and supercapacitor ESS are capable of reducing the load to a similar extend. Objectively, the percentage of load fluctuations within the engine limit is found to be 1% higher for the flywheel ESS than for the supercapacitor ESS, meaning the flywheel ESS would be better suited for this application. When considering the weight and size of the modules, however, the supercapacitor ESS is assumed to be convenient for fitting into the CSD due to the number of small modules. Also, considering the fact that cost of the flywheel ESS modules is based on assumptions and not based on actual estimates provided by manufacturers like for the supercapacitor ESS, the price of the flywheel modules might be significantly higher. The choice between the two types of energy storage considered in this research is therefore thought to be fully dependent on the preferences of the ship's owner

regarding investment cost, weight and size.

Furthermore, even though a lot of data from dredging operation was available, the data that is used came from a single dredging project. Difference was seen in the conditions with respect to total power demand and the rate of change of the power demand, but a different dredging project may have led to different results.

## 7.2.2 Recommendations

### Power management system

For the PMS a maximum ramp-up and maximum ramp-down is used to determine the loading limit of the main engines. While this allows for a relatively simple PMS, load steps are not taken into account. As a result, a more conservative loading limit is assumed for the PMS than the load the engines are capable of handling in reality. Therefore, the inlet receiver pressure  $p_1$  should be included in the PMS. With  $p_1$  the amount of air inside the cylinders can be determined and consequently the right amount of fuel can be injected. Control of the air excess ratio  $\lambda$  allows precise control of the maximum change in load to avoid knock and misfire.

### Engine wear

From this research it is concluded that transient loads can be reduced using an ESS. However, during this research it proved to be difficult to quantify the effect of transient loads on engine wear. Although it is suspected that transient loads cause an increased wear on diesel engines no conclusive research is found in available literature. Further research into the effects of transient loads on diesel engine wear is thought to be valuable.

### ESS size

The sizing methodology of the ESS used in this research is based on the maximum occurring peak power and energy used over a certain period of time. During simulations it is found that the amount of available ESS power and energy is often far too great. It is therefore recommended that it might be better to determine ESS power and energy in such a way that a predetermined percentage of loads do not exceed the engine limit instead of sizing the ESS based on the maximum load.

Alternatively, it might more convenient to reverse the ESS sizing process by starting with the selection of a typical amount of ESS power and energy storage capacity. For instance, for dual fuel engines it can then be determined under what conditions combustion of LNG is possible or when switching to combustion of diesel is inevitable.

### Supercapacitor aging effects

For the supercapacitors the  $R_{ESR}$  and  $C$  are assumed to be constant. For this research this is thought to be a fair assumption since relative short simulations are conducted. To get a more accurate prediction of the ESS lifetime aging effects need to be taken into account.

### Switching of power electronics

The data that is used during simulations has a frequency of 5 Hz. This means that the time step during simulations is larger than the response time of the power electronics of the ESS. The response of the ESS is therefore taken as instantaneous so the actual switching is not taken into account. For higher frequencies it would be useful to model the switching of power electronic converters to get a more accurate behavior of the ESS.

# Bibliography

- [1] AEP Hybrid Power. *Datasheet - Bidirectional DC/DC & AC/DC converter*. AEP Hybrid Power, Alblasserdam, Netherlands, 2015.
- [2] AEP Hybrid Power. *Datasheet - Cell Pack Version 2.0*. AEP Hybrid Power, Alblasserdam, Netherlands, 2015.
- [3] T.P. Bartstra. *Development of a cutter ladder vibration model*. Faculty of Civil Engineering and Geosciences, Delft University of Technology, Delft, Netherlands, July 2016.
- [4] B. Bolund et al. *Flywheel energy and power storage systems*. Ångström Laboratory, Department of Engineering Sciences, Uppsala University, Uppsala, Sweden, 2005.
- [5] Bureau Veritas. *Rules for the Classification of Steel Ships, PART C - Machinery, Electricity, Automation and Fire Protection*. Bureau Veritas Marine & Offshore Division, Neuilly-sur-Seine, France, 2016.
- [6] M. Carlier. *LNG Bunkering*. Platts Mediterranean Bunker Fuel Conference, Barcelona, December 2012.
- [7] T. Christen, M.W. Carlen. *Theory of Ragone plots*. ABB Corporate Research Ltd., Baden-Dattwil, Switzerland, 2000.
- [8] Corvus Energy. *Edda Ferd - Platform Supply Vessel, Major Fuel Savings for Dynamics Positioning*. Retrieved April 10th, 2017 from <http://corvusenergy.com/marine-project/edda-ferd-platform-supply-vessel-psv/>
- [9] N. Devillers et al. *Review of characterization methods of supercapacitor modelling*. Journal of Power Sources vol. 246, pages 596-608, 2014.
- [10] DNV GL Maritime. *LNG as ship fuel - Current price development oil and gas*. Retrieved June 7, 2017 from <https://www.dnvgl.com/maritime/lng/current-price-development-oil-and-gas.html>
- [11] M. Donea, D. Gerling. *Design and Calculation of a 300 kW High-Speed PM Motor for Aircraft Application*. Chair of Electrical Drives and Actuators, Universität der Bundeswehr München, Neubiberg, Germany, 2016.
- [12] EERA JP Energy Storage - Mechanical Storage Sub-program. *Kinetic Energy Storage Based on Flywheels: Basic Concepts, State of the Art and Analysis of Applications*. Centro de Investigaciones Energéticas, Medioambientales y Tecnológicas, Madrid, Spain, March 2013.
- [13] B. Espinar, D. Mayer. *The role of energy storage for mini-grid stabilization*. International Energy Agency Photovoltaic Power Systems Program, Paris, France, 2011.
- [14] M. Farhadi. *Energy Storage Technologies for High-Power Applications*. IEEE Transactions on Industry Applications, Vol. 52, No. 3, May/June, 2016.
- [15] A.M. Gee, R.W. Dunn. *Analysis of Trackside Flywheel Energy Storage in Light Rail Systems*. IEEE Transactions on Vehicular Technology, Vol. 64, No. 9, September, 2015.
- [16] I. Georgescu et al. *Dynamic Behaviour of Gas and Dual-Fuel Engines: Using Models and Simulations to Aid System Integration*. CIMAC Congress, Helsinki, June 6-10, 2016.
- [17] I. Georgescu et al. *Characterisation of Large Gas and Dual-fuel Engines*. MTZ Industrial, Issue 3/2016, August 2016.

- [18] J.L.S. Gerritsen. *The Hybrid Cutter Dredger - A study on technical and economical feasibility*. Faculty of Mechanical, Maritime and Materials Engineering, Delft University of Technology, Delft, Netherlands, October 2016.
- [19] J.J. Grainer, W.D. Stevenson, Jr. *Power System Analysis*. McGraw-Hill Education, New York, United States, 1994.
- [20] C.A. Gross, S.P. Meliopoulos. *Per-Unit Scaling in Electric Power Systems*. IEEE Transactions on Power Systems, Vol. 7, No. 2, May, 1992.
- [21] M.S. Halper, J.C. Ellenbogen. *Supercapacitors: A Brief Overview*. MITRE Nanosystems Group, McLean, Virginia, United States, March, 2006.
- [22] J.G.R. Hansen, D.U. O’Kain. *An Assessment of Flywheel High Power Energy Storage Technology for Hybrid Vehicles*. Oak Ridge National Laboratory, Oak Ridge, Tennessee, United States, 2011.
- [23] S. Hayman, J. Stratton. *Hybrid-powered Marine Vessels*. Proceedings of the 2nd AS-ME/USCG Workshop on Marine Technology and Standards, Washington DC, United States, July, 2010.
- [24] M. Hedlund et al. *Flywheel Energy Storage for Automotive Applications*. Energies, Vol.8, No.10, 2015, pages 10636-10663.
- [25] IEC62391-1. *Fixed Electric Double-layer Capacitors for Use in Electronic Equipment Part 1: Generic Specification*. International Electrotechnical Commission, Geneva, Switzerland, 2005.
- [26] IEC62391-2. *Fixed Electric Double-layer Capacitors for Use in Electronic Equipment Part 2: Sectional specification: Electric double layer capacitors for power application*. International Electrotechnical Commission, Geneva, Switzerland, 2006.
- [27] International Council on Combustion Engines. *Transient Response Behaviour of Gas Engines - Position Paper*. CIMAC Working Group Gas Engines, Frankfurt, Germany, 2011.
- [28] International Council on Combustion Engines. *Impact of Gas Quality on Gas Engine - Position Paper*. CIMAC Working Group Gas Engines, July 2015.
- [29] International Council on Combustion Engines. *Future Fuel Scenarios and their Impact on Lubrication*. CIMAC Working Group Marine Lubricants, May 2014.
- [30] International Council on Combustion Engines. *Information Concerning the Application of Gas Engines in the Marine Industry*. CIMAC Working Group Gas Engines, December 2013.
- [31] International Electrotechnical Commission. *White Paper - Electrical Energy Storage*. Retrieved March 17, 2017 from <http://www.iec.ch/whitepaper/pdf/iecWP-energystorage-LR-en.pdf>.
- [32] J.K. Kaldellis. *Stand-Alone and Hybrid Wind Energy Systems, 1st Edition - Technology, Energy Storage and Applications*. Woodhead Publishing Ltd., Cambridge, United Kingdom, 2010.
- [33] H. Klein Woud, D. Stapersma. *Design of Propulsion and Electric Power Generation Systems*. IMarEST, Institute of Marine Engineering, Science and Technology, London, 2002.
- [34] G. Kron. *Tensors for circuits*. Dover Publications Inc., New York, United States, 1959.
- [35] P. Kundur. *Power System Stability and Control*. McGraw-Hill Education, 1st Edition, 1994.
- [36] X. Luo et al. *Overview of current development in electrical energy storage technologies and the application potential in power system operation*. Applied Energy, Volume 137, 1 January 2015, pages 511-536.
- [37] Z. Lyu. *Concept Design of Hybrid Crane Vessel - Feasibility study of utilizing electric energy storage technology*. Faculty of Mechanical, Maritime and Materials Engineering, Delft University of Technology, Delft, Netherlands, April, 2016.
- [38] MAN Diesel & Turbo. *MAN 48/60CR Project Guide - Marine Four-stroke Diesel Engines Compliant with IMO Tier II*. MAN Diesel & Turbo SE, Augsburg, Germany, 2016.
- [39] Maritime Journal. *Foss Unveils ‘Carolyn Dorothy’ (February 1, 2009)*. Retrieved August 26, 2016 from [http://www.maritimejournal.com/news101/tugs,-towing-and-salvage/foss\\_unveils\\_carolyn\\_dorothy](http://www.maritimejournal.com/news101/tugs,-towing-and-salvage/foss_unveils_carolyn_dorothy).

- [40] Maxwell Technologies. *K2 Ultracapacitor - 2.7V Series Datasheet*. Document number: 1015370.4, Maxwell Technologies Inc., San Diego, California, United States, 2013.
- [41] B.T.W. Mestemaker. *Diesel & dual fuel engine model (Diesel A5.0) - Modelling of a combined diesel & gas engine model based on the Diesel A4.2 model*. MTI Holland B.V., Delft, Netherlands, 2014.
- [42] B.T.W. Mestemaker. *Dual fuel engine application on trailing suction hopper dredger - Simulation results with a new power management system*. MTI Holland B.V., Delft, Netherlands, 2016.
- [43] S.A. Miedema, Z. Lu. *The Dynamical Behaviour of a Diesel Engine*. Proc. WEDA XII Technical Conference & Texas A&M Dredging Seminar, June 12-15, Denver, Colorado, United States, 2002.
- [44] D.B. Murray, J.G. Hayes. *Cycle Testing of Supercapacitors for Long-Life Robust Applications*. IEEE Transactions on Power Electronics, Vol. 30, No. 5, May, 2015.
- [45] National Institute of Statistics and Economic Studies. *International prices of imported raw materials - Domestic diesel heating oil (Rotterdam) - Prices in euros per tonne - CIF - 1% of sulfur*. Retrieved June 7, 2017, from <https://www.bdm.insee.fr/bdm2/affichageSeries?idbank=001565199&page=tableau&request.locale=en>
- [46] H. Pestana et al. *Future trends of electrical propulsion and implications to ship design*. ABB Marine, Billingstad, Norway, 2014.
- [47] J. Pollevliet. *Elektronische Vermogencontrole, Vol.1: Vermogenelektronica 7th Edition*. Academia Press, Gent, Belgium, 2011.
- [48] C.D. Rakopoulos, E.G. Giakoumis. *Diesel Engine Transient Operation - Principles of Operation and Simulation Analysis*. Springer-Verlag London Ltd., London, United Kingdom, 2009.
- [49] B.M. Rekelhof. *Optimisation of the power generation system of a DP2 class pipelay vessel*. Faculty of Mechanical, Maritime and Materials Engineering, Delft University of Technology, Delft, Netherlands, December 2016.
- [50] Royal IHC. *Royal IHC Launches DEME's LNG-powered TSHD Scheldt River*. Press release. Retrieved 1 May, 2017, from <https://www.royalihc.com/en/news/royal-ihc-launches-demes-lng-powered-tshd-scheldt-river>
- [51] Royal IHC. *World's First LNG-powered Hopper Dredger Launched*. Press release. Retrieved 1 May, 2017, from <https://www.royalihc.com/en/news/worlds-first-lng-powered-hopper-dredger-launched>
- [52] Royal IHC. *Royal IHC To Build World's Largest Cutter Suction Dredger For DEME*. Press release. Retrieved 1 May, 2017, from <https://www.royalihc.com/en/news/royal-ihc-to-build-worlds-largest-cutter-suction-dredger-for-deme>
- [53] S. Schoenung. *Energy Storage Systems Cost Update - A Study for the DOE Energy Storage System Program*. Sandia National Laboratories, Albuquerque, New Mexico, United States, 2011.
- [54] D. Stapersma. *Lecture notes WB4408A and WB4408B - Diesel Engines*. NLDA and Delft TU, 8th Edition, 2010.
- [55] P.A. Stott et al. *DC Link Voltage Stabilisation in Hybrid Renewable Diesel Systems*. Institute for Energy Systems, University of Edinburgh, Edinburgh, United Kingdom, 2007.
- [56] Technical and commercial cost estimate. *Energy Storage System for Marine Application, Royal IHC*. AEP International B.V., Alblasterdam, Netherlands, 2016.
- [57] A.G. Ter-Gazarian. *Energy Storage for Power Systems, 2nd Edition*. Institution of Engineering and Technology, London, United Kingdom, 2011.
- [58] E.D. Tuft. *Impacts of Low Load Operation of Modern Four-stroke Diesel Engines in Generator Configuration*. Norwegian University of Science and Technology, Trondheim, Norway, 2014.
- [59] M. Uno, K. Tanaka. *Accelerated Charge-Discharge Cycling Test and Cycle Life Prediction Model for Supercapacitors in Alternative Battery Applications*. IEEE Transactions on Industrial Electronics, Vol. 59, No. 12, December, 2012.

- 
- [60] W.J. Vlasblom. *Design of Dredging Equipment, lecture notes 3 - The Cutter Suction Dredger*. Delft University of Technology, Delft, Netherlands, May 2005.
- [61] P.G.E. Vos. *De invloed van vermogenselektronica in de scheepsbouw - Presentation at Vermogenselektronica 2014*. IHC Drives & Automation B.V., Sliedrecht, Netherlands, 2014.
- [62] J.W. de Vriend. *Electrical network modeling - Interconnection for electrical machines*. Internal report, MTI Holland B.V., Delft, The Netherlands, 2014.
- [63] Wärtsilä Finland. *Wärtsilä 34DF Product Guide*. Wärtsilä Marine Solutions, Vaasa, Finland, 2016.
- [64] World Maritime News. *OSV Viking Lady to Get First Hybrid System (March 14, 2012)*. Retrieved May 1, 2017, from <http://worldmaritimeneews.com/archives/49599/uk-osv-viking-lady-to-get-first-hybrid-system/>.
- [65] X. Xu. *Application of singular perturbation models to long term dynamic stability studies*. Doctoral dissertation, Department of Electrical and Computer Engineering, University of Western Ontario, London, Ontario, Canada, 1999.

## Appendix A

# Direct-quadrature-zero ( $dq0$ ) transformation

The  $dq0$  transformation is a transformation from a three-phase stationary coordinate system to a  $dq0$  rotating coordinate system. The transformation is made in two steps:

- Transformation from three-phase stationary coordinates ( $abc$ ) to two-phase ( $\alpha\beta$ ) coordinates:

$$[\alpha_u \quad \beta_u \quad o_u] = [a_u \quad b_u \quad c_u] \frac{2}{3} \begin{bmatrix} 1 & 0 & 1 \\ -\frac{1}{2} & \frac{\sqrt{3}}{2} & \frac{1}{2} \\ -\frac{1}{2} & -\frac{\sqrt{3}}{2} & \frac{1}{2} \end{bmatrix} \quad (\text{A.1})$$

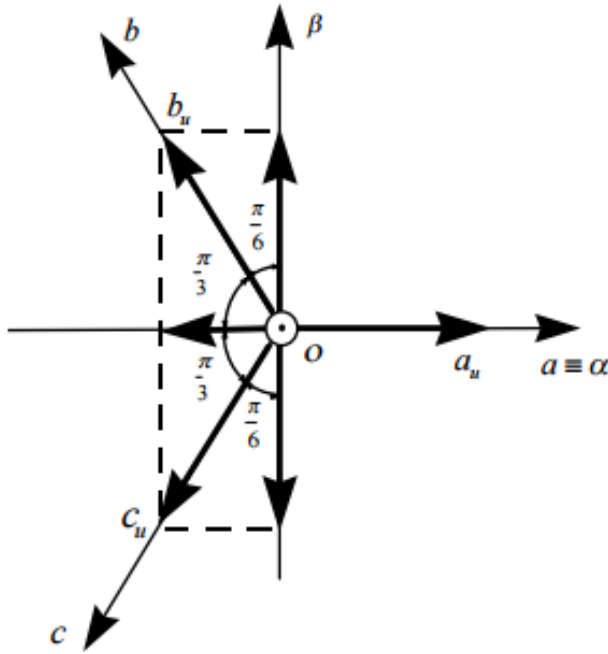


Figure A.1: Transformation from three-phase to two-phase coordinates

- Transformation from  $(\alpha\beta)$  stationary coordinates to  $dq0$  rotating coordinates:

$$[d_u \quad q_u \quad o_u] = [\alpha_u \quad \beta_u \quad o_u] \frac{2}{3} \begin{bmatrix} \cos \theta & -\sin \theta & 0 \\ \sin \theta & \cos \theta & 0 \\ 0 & 0 & 1 \end{bmatrix} \quad (\text{A.2})$$

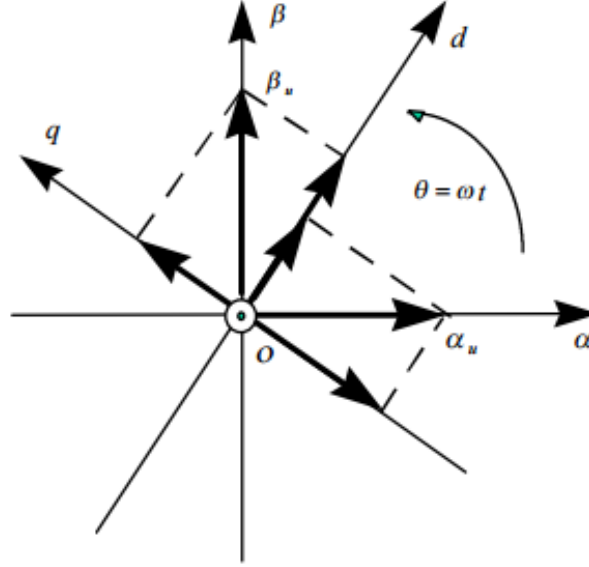


Figure A.2: Transformation from  $\alpha\beta$  to  $dq0$  coordinates

So that:

$$[d_u \quad q_u \quad o_u] = [a_u \quad b_u \quad c_u] \frac{2}{3} \begin{bmatrix} \cos \theta & -\sin \theta & \frac{1}{2} \\ \cos(\theta - \frac{2\pi}{3}) & -\sin(\theta - \frac{2\pi}{3}) & \frac{1}{2} \\ \cos(\theta + \frac{2\pi}{3}) & -\sin(\theta + \frac{2\pi}{3}) & \frac{1}{2} \end{bmatrix} \quad (\text{A.3})$$

Representation of a vector in any n-dimensional space is accomplished through the product of a transpose n-dimensional vector of coordinate units and a vector representation of the vector, whose elements are corresponding projections on each coordinate axis, normalized by their unit values. In three-phase space this looks like:

$$X_{abc} = [a_u \quad b_u \quad c_u] \begin{bmatrix} x_a \\ x_b \\ x_c \end{bmatrix} \quad (\text{A.4})$$

Assuming the three-phase system is balanced ( $x_0 = 0$ ), a three-phase representation vector  $X_{abc} = \begin{bmatrix} X_a \\ X_b \\ X_c \end{bmatrix}$  transforms to *dq0* representation vector  $X_{dq} = \begin{bmatrix} X_d \\ X_q \end{bmatrix}$  using transformation matrix  $T$ , defined as:

$$T = \frac{2}{3} \begin{bmatrix} \cos(\omega t) & \cos(\omega t - \frac{2}{3}\pi) & \cos(\omega t + \frac{2}{3}\pi) \\ -\sin(\omega t) & -\sin(\omega t - \frac{2}{3}\pi) & -\sin(\omega t + \frac{2}{3}\pi) \end{bmatrix} \quad (\text{A.5})$$

*dq0* rotating coordinates are now obtained by multiplication with  $T$ :

$$X_{dq} = TX_{abc} \quad (\text{A.6})$$

The inverserve transformation is given by:

$$X_{abc} = T'X_{dq} \quad (\text{A.7})$$

Where  $T'$  is defined as:

$$T' = \frac{2}{3} \begin{bmatrix} \cos(\omega t) & -\sin(\omega t) \\ \cos(\omega t - \frac{2}{3}\pi) & -\sin(\omega t - \frac{2}{3}\pi) \\ \cos(\omega t + \frac{2}{3}\pi) & -\sin(\omega t + \frac{2}{3}\pi) \end{bmatrix} \quad (\text{A.8})$$

## Appendix B

# Kron reduction

The Kron reduction is a method used to eliminate buses from a network that are not connected to a source or consumer. Consider a network with four impedances, as shown in Figure B.1.

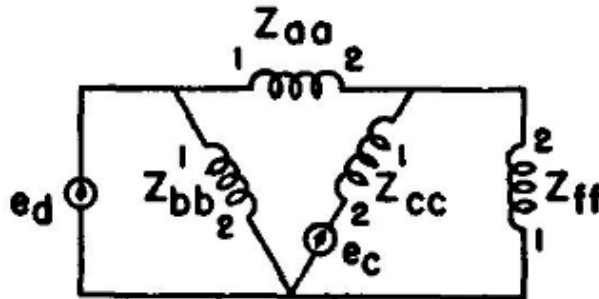


Figure B.1: Example network[34]

In order to establish equations in the form of  $\bar{e} = Z \cdot \bar{i}$  for this network all interconnections between impedances are removed and all are shortcircuited, which results in the network shown in Figure B.2. A voltage  $e_d$  is assumed in a branch with zero impedance. Similarly,  $Z_{bb}$  is assumed to have a voltage  $e_b$  in series with it whose value is zero. The arrows in the figure indicate mutual impedances, which are both zero.

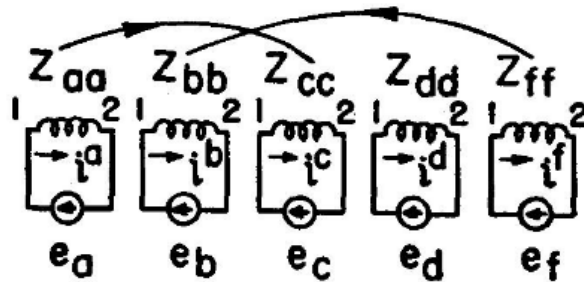


Figure B.2: Primitive network of Figure B.1[34]



# Appendix C

## Energy storage sizing Matlab script

```
%%%%%%%%%%%%%%%%%%%%%%%%%%%%%%%%%%%%%%%%%%%%%%%%%%%%%%%%%%%%%%%%%%%%%%%%%%%%%%  
%%          Sizing file for energy storage system          %%  
%          M.J.W. van Leeuwen          %  
%          Last modified: 17-03-2017          %  
%%%%%%%%%%%%%%%%%%%%%%%%%%%%%%%%%%%%%%%%%%%%%%%%%%%%%%%%%%%%%%%%%%%%%%%%%%%%%%  
  
% This file is used to determine the power and energy requirements of an  
% ESS based on cutter data. The number of cycles and maximum (dis)charge  
% time is also determined.  
  
%% Inputs  
  
file_location = 'F:\Data\Processed\';  
file_name     = '201601';           % Year and month  
d             = 1;                 % 0 for 1-9 days, 1 for more etc.  
nos          = 2;                 % Number of sets  
nof          = 24;                % Number of files  
  
Peng         = 10.8e6;            % Engine maximum power [W]  
Neng         = 2;                 % Number of engines  
t_ramp       = 300;              % 1.) 300s 2.) 60s 3.) 30s  
  
Max_step_up  = Neng*Peng/t_ramp; % Ramp up [W/s]  
Max_step_down = inf;            % Ramp down [W/s]  
Initial_energy = 0;             % Initial stored energy [J]  
  
%% Load data and merge powers  
  
current_directory = cd;  
P = [];           % Initial empty vector  
E = [];           % Initial empty vector  
t_d = [];        % Initial empty vector  
cyc = [];        % Initial empty vector  
  
for j = 1-d:nos-d  
  
    date = ['201601' int2str(d)];  
    file_name = [date num2str(j)];
```

```

for k = 1:nof;

cd(file_location)
cd(file_name)
file = [file_name '_' num2str(k) '.mat'];
load(file)

SDP.PWR = struct.SDP.PWR;
ID1.PWR = struct.ID1.PWR;
ID2.PWR = struct.ID2.PWR;
CMLPWR = struct.CMLPWR;
CMRPWR = struct.CMRPWR;
SWLPWR = struct.SWLPWR;

TOT.PWR = (SDP.PWR + ID1.PWR + ID2.PWR + CMLPWR + CMRPWR + SWLPWR)*1e3;

%% Select load
P.DE = TOT.PWR;
P_init = P.DE;

%%
t = (0:0.2:(length(P.DE)-1)/5);           % Time vector [s], dt = 0.2
dt = t(2)-t(1);                           % Time step [s]
n = length(P.DE);                          % Length of vectors

dP1 = diff(P.DE)./diff(t)';                % Loadstep [W/s]

for i = 1:n-1;

    if (P.DE(i+1) - P.DE(i))/dt > Max_step_up

        P.DE(i+1) = P.DE(i) + Max_step_up*dt;
    end

    if (P.DE(i) - P.DE(i+1))/dt > Max_step_down

        P.DE(i+1) = P.DE(i) - Max_step_down*dt;
    end
end

P.ESS = P_init - P.DE;                      % Power delivered by ESS [W]

% Energy storage minimum required power:
ESS_P = max(abs(P.ESS));
% Energy storage minimum storage capacity:
E_cum = cumtrapz(t,P.ESS);

%% Energy used during longest discharge peak and longest peak duration

indx = find(P.ESS==0)/5;                    % Find zero locations
indxstep = zeros(1,length(indx)-1);

for q = 1:length(indx)-1
    indxstep(q) = indx(q+1)-indx(q);        % Steps between peaks
    Peak_energy(q) = E_cum(indx(q)*5) - ...

```

```

        E_cum(indx(q+1)*5);           % Energy used during peaks
end

maxpeakdur(k) = max(indxstep);       % Maximum peak duration

peak_index = find(indxstep==maxpeakdur(k));
Energy_used(k) = -min(Peak_energy); % Required ESS Energy [J]
ESS_Power(k)   = ESS_P;             % Required ESS power [W]

Min_power = max(ESS_Power);
Min_energy = max(Energy_used);

%% Cycles
% Counts the number of times (dis)charge starts and ends. The number
% is divided by two because cycle is defined as charge+discharge.

cycl = length(find(indxstep > 0.21));
cycles(k) = cycl/2;

end

%% Save energy storage requirements

cd(file_location)
cd(file_name)
saved_name = ['ESS_requirements' '_' file_name '_' ...
             num2str(Max_step_up/1e3) 'u' '_' num2str(Max_step_down/1e3) 'd' '.mat'];
save(saved_name, 'ESS_Power', 'Energy_used', ...
      'Max_step_up', 'Max_step_down', 'Min_power', 'Min_energy')

% Concatenate vectors
P = [ P ; ESS_Power ];
E = [ E ; Energy_used ];
t_d = [ t_d ; maxpeakdur ];
cyc = [ cyc ; cycles ];

% Clear loop vectors
ESS_Power = [];
Energy_used = [];
maxpeakdur = [];
cycles = [];

end

%% Script output

Pmin = max(max(P))           % Required power based on used data
Emin = max(max(E))           % Required capacity based on used data
Max_discharge_time = max(max(t_d)) % Maximum discharge time [s]
Avg_cyc = sum(cyc)/length(cyc); % Average number of cycles per hour
Avg_cyc = round(sum(Avg_cyc)/length(Avg_cyc))

```

# Appendix D

## Simulink models

### D.1 Power threshold model

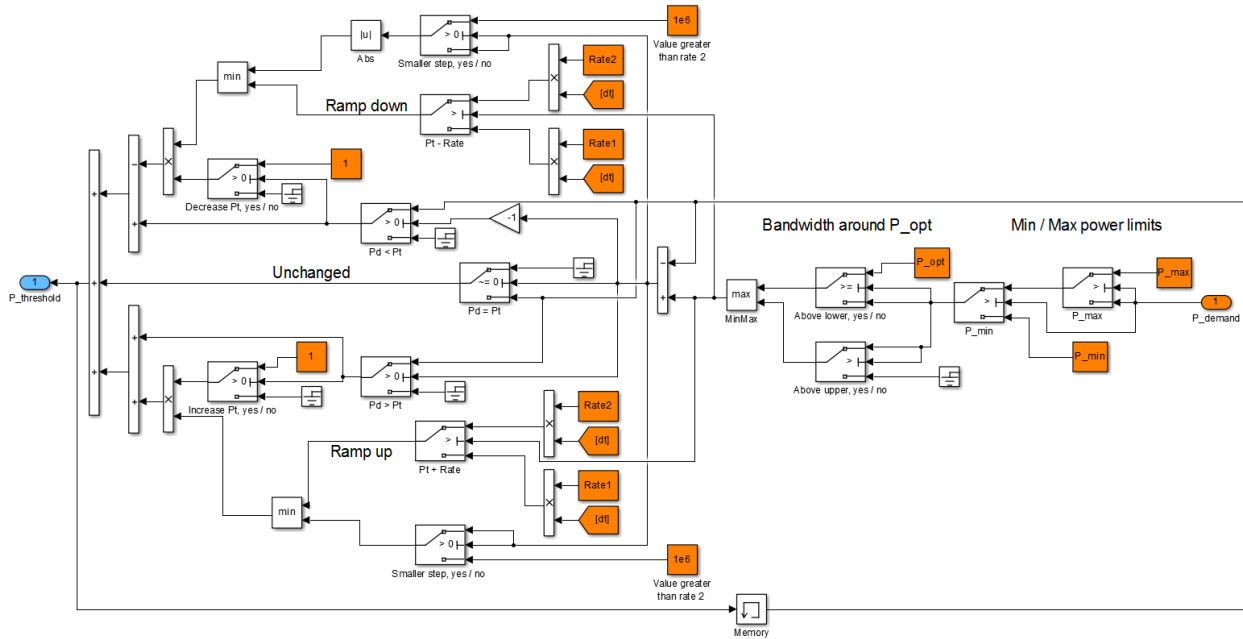


Figure D.1: Power threshold submodel

## D.2 Supercapacitor model

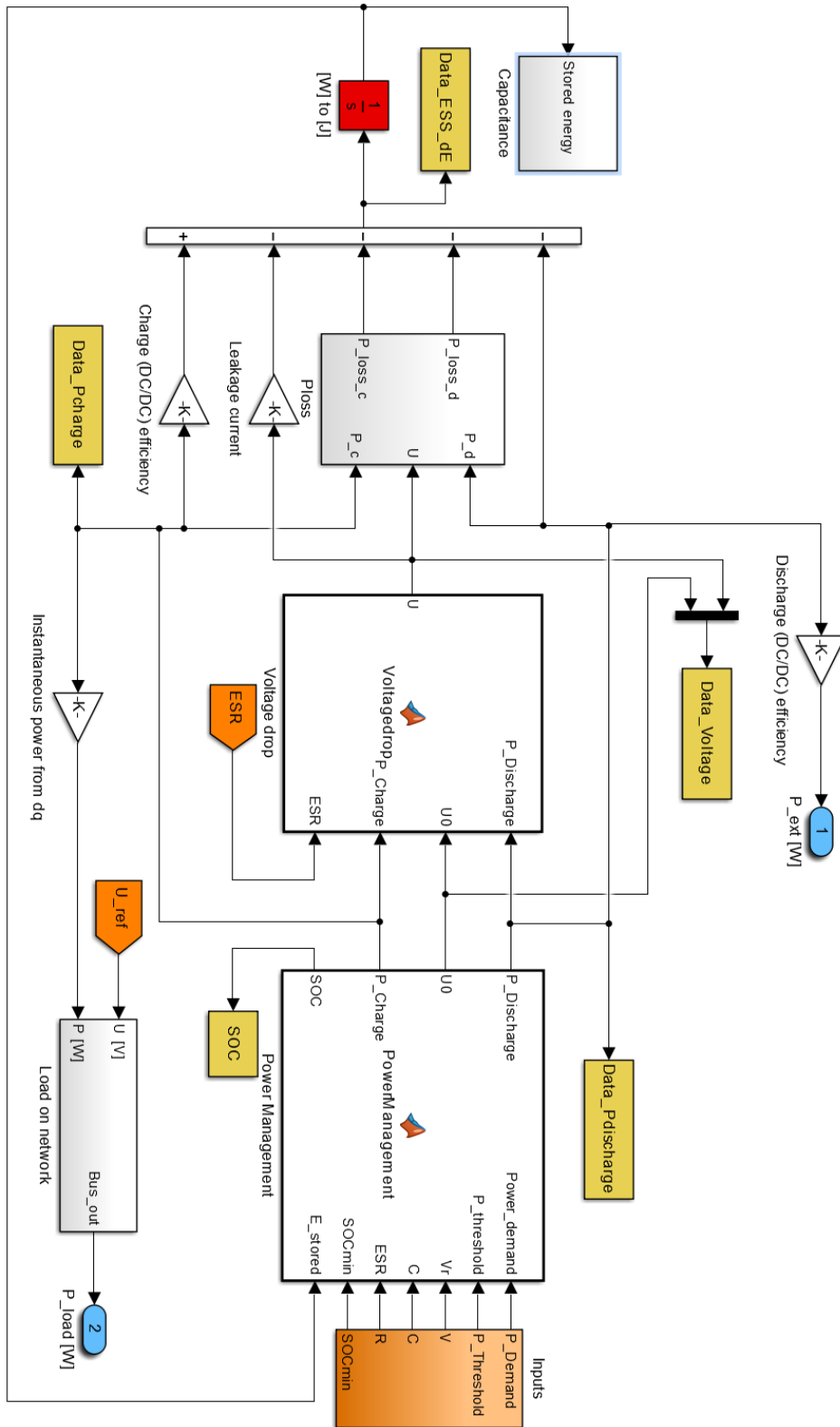


Figure D.2: Supercapacitor Simulink model



## D.2.1 Power management and voltage drop

```
function [P_Discharge,U0,P_Charge,SOC] = PowerManagement(Power_demand,...
    P_threshold,Vr,C,ESR,SOCmin,E_stored)

%% Maximum/minimum amount of stored energy

E_stored_max = 0.5*C*Vr^2;
E_stored_min = SOCmin*E_stored_max;

%% State of charge

SOC = E_stored/E_stored_max;

%% Supercapacitor voltage

U0 = sqrt((2*SOC*E_stored_max)/C);

%% Discharge power

if Power_demand > P_threshold
    P_Discharge = Power_demand - P_threshold;
else P_Discharge = 0;
end

%% Charge power

if Power_demand < P_threshold
    P_Charge = P_threshold - Power_demand;
else P_Charge = 0;
end

%% Maximum values for (dis)charging

P_ch_max    = U0^2/(8*ESR);
P_dch_max   = P_ch_max;

if P_Charge > P_ch_max
    P_Charge = P_ch_max;
end

if P_Discharge > P_dch_max
    P_Discharge = P_dch_max;
end
```

```
%% Depth of (dis)charge  
if E_stored <= E_stored_min  
    P_Discharge = 0;  
end  
if E_stored >= E_stored_max  
    P_Charge = 0;  
end  
end
```

```
function U = Voltagedrop(P_Discharge,U0,P_Charge,ESR)  
% Initial charge/Discharge currents  
I_d = P_Discharge/U0;  
I_c = P_Charge/U0;  
if P_Discharge > 0  
    dU = I_d*ESR;  
elseif P_Charge > 0  
    dU = -I_c*ESR;  
else  
    dU = 0;  
end  
U = U0 - dU;  
end
```

### D.3 Flywheel model

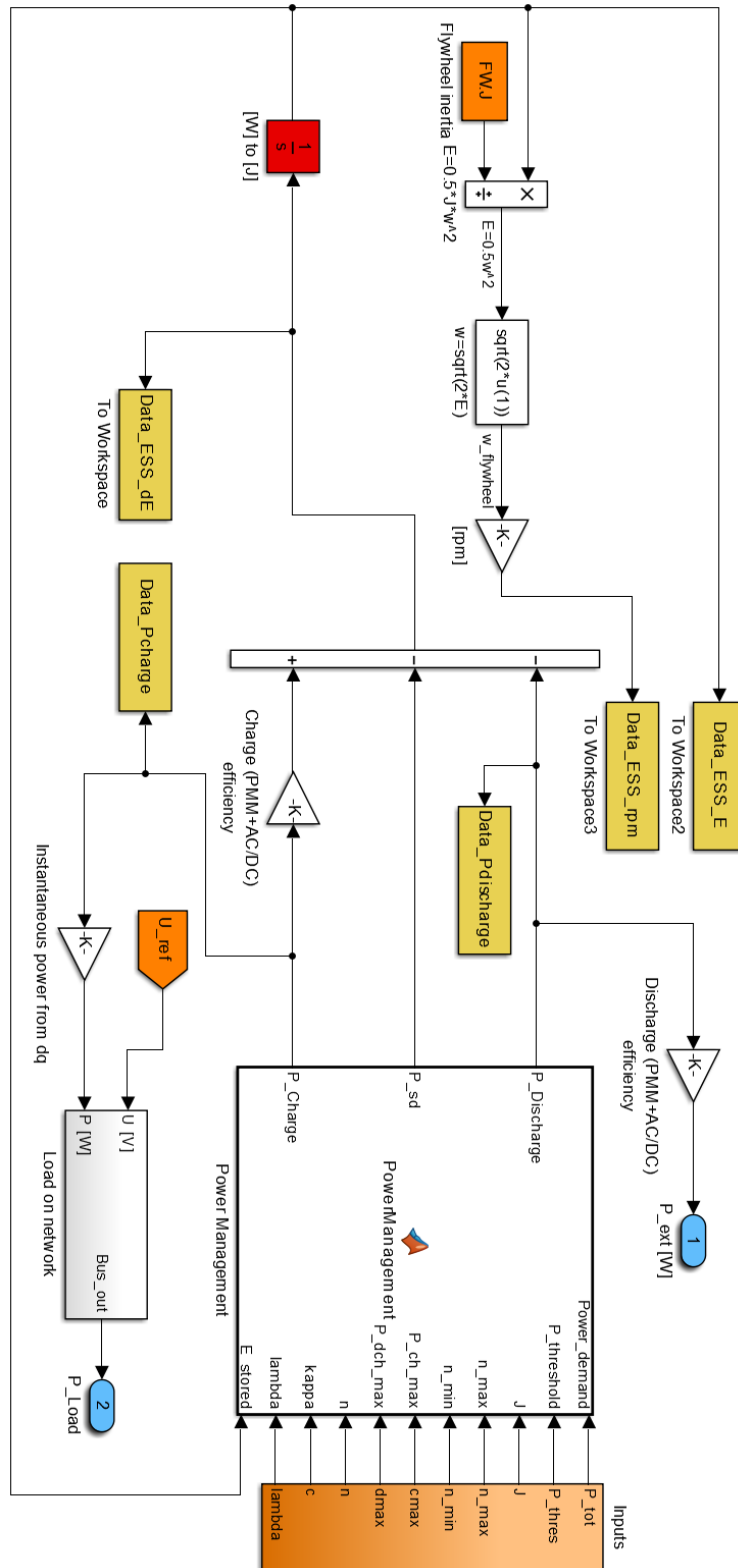


Figure D.6: Flywheel Simulink model

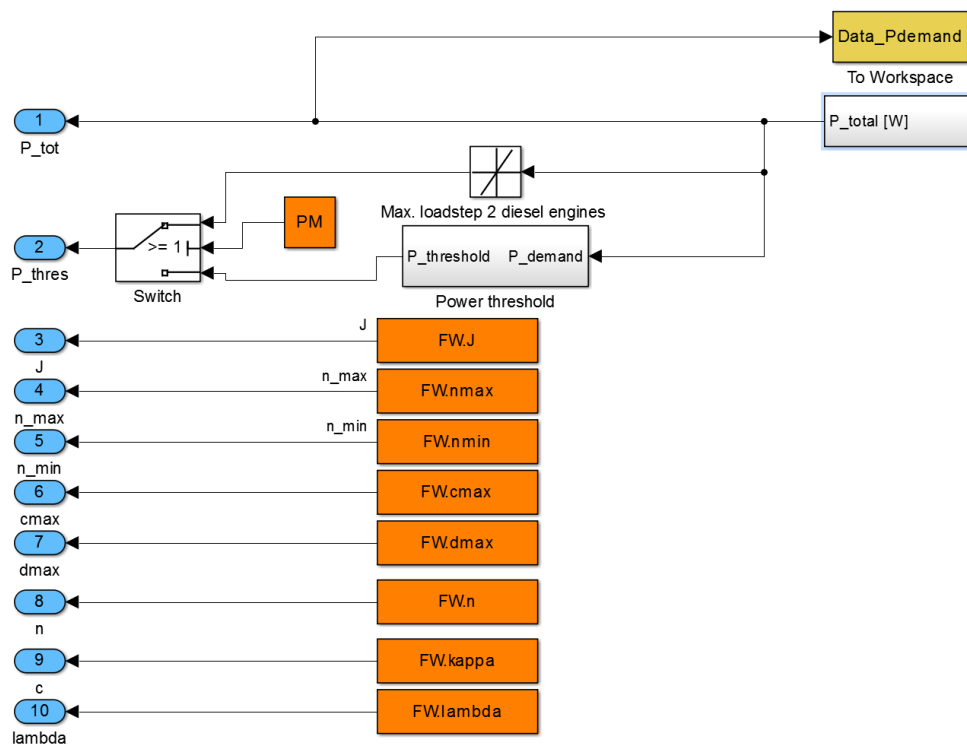


Figure D.7: Flywheel inputs subsystem

### D.3.1 Power management

```
function [P_Discharge , P_sd , P_Charge] = PowerManagement (Power_demand , ...
    P_threshold , J , n_max , n_min , P_ch_max , P_dch_max , n , kappa , lambda , E_stored)
```

```
%% Maximum/minimum amount of stored energy
```

```
E_stored_max = n*0.5*J*(n_max/60*2*pi)^2;
E_stored_min = n*0.5*J*(n_min/60*2*pi)^2;
```

```
SOC = E_stored/E_stored_max;
```

```
%% Discharge power
```

```
if Power_demand > P_threshold
```

```
    P_Discharge = Power_demand - P_threshold;
```

```
else P_Discharge = 0;
```

```
end
```

```
%% Charge power
```

```
if Power_demand < P_threshold
```

```
    P_Charge = P_threshold - Power_demand;
```

```
else P_Charge = 0;
```

```
end

%% Maximum values for (dis)charging

if P_Charge >= n*P_ch_max
    P_Charge = n*P_ch_max;
end

if P_Discharge >= n*P_dch_max
    P_Discharge = n*P_dch_max;
end

%% Depth of (dis)charge

if E_stored <= E_stored_min
    P_Discharge = 0;
end

if E_stored >= E_stored_max
    P_Charge = 0;
end

%% Self-discharge
% Exponential decay of energy, based on 20% loss in one hour

P_sd = -lambda*E_stored_max*exp(lambda*((SOC-1)/kappa));

if SOC < .26          % Removes instability at low state of charge
    P_sd = 0;
end

end
```

# Appendix E

## Cutter inertia calculation

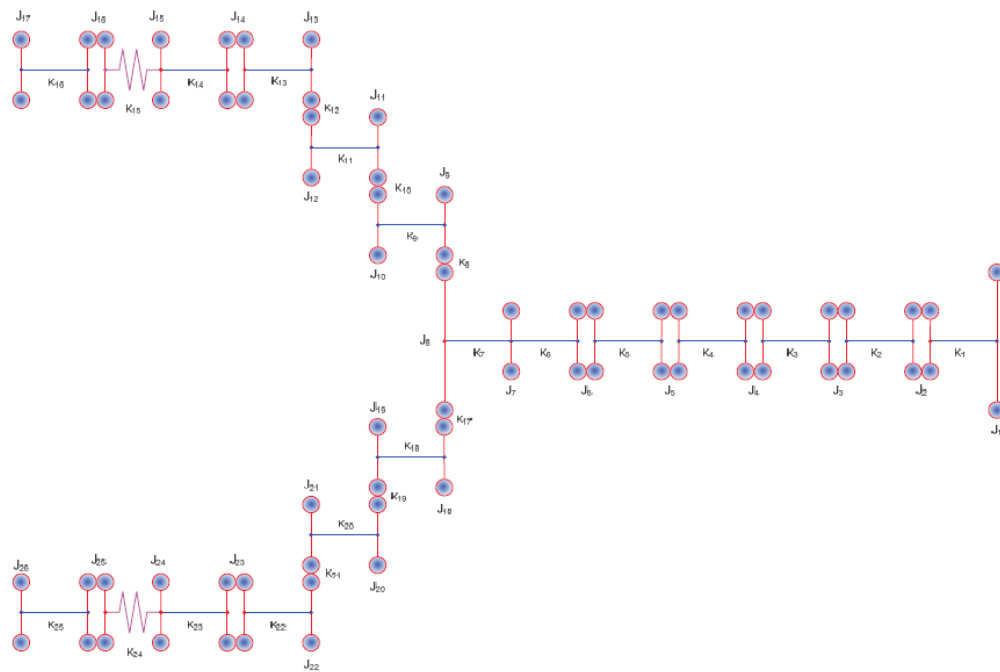


Figure E.1: Cutter mass-spring system

Nr.	Branch	Element	Mass moment of inertia [kgm <sup>2</sup> ]	Stiffness connection [Nm/rad]	Reduction i [related to E-motor speed]
J <sub>1</sub>	-	Cutter Type sand/clay/rock - 6 arm	17791		39,913
K <sub>1</sub>	-	Cutter shaft		3,368 E8	39,913
J <sub>2</sub>	-	Cutter shaft coupling	1091		39,913
K <sub>2</sub>	-	Intermediate shaft 1		1,592 E8	39,913
J <sub>3</sub>	-	Intermediate shaft coupling 1	772		39,913
K <sub>3</sub>	-	Intermediate shaft 2		1,592 E8	39,913
J <sub>4</sub>	-	Intermediate shaft coupling 2	772		39,913
K <sub>4</sub>	-	Intermediate shaft 3		1,592 E8	39,913
J <sub>5</sub>	-	Intermediate shaft coupling 3	772		39,913
K <sub>5</sub>	-	Intermediate shaft 4		1,592 E8	39,913
J <sub>6</sub>	-	Gearbox flange	553		39,913
K <sub>6</sub>	-	Gearbox shaft out 1		9,905 E8	39,913
J <sub>7</sub>	-	Gearbox trust bearing	1376		39,913

Figure E.2: Element inertia part one

K <sub>7</sub>	-	Gearbox shaft out 2		1,014 E9	39,913
J <sub>8</sub>	-	End wheel	3829		39,913
K <sub>8</sub>	1	Gear reduction 1		1 E10	-
J <sub>9</sub>	1	Pinion 1	67		14,216
K <sub>9</sub>	1	Gear reduction shaft 1		1,824 E9	14,216
J <sub>10</sub>	1	Wheel 1	532		14,216
K <sub>10</sub>	1	Gear reduction 2		1 E10	-
J <sub>11</sub>	1	Pinion 2	7		4,087
K <sub>11</sub>	1	Gear reduction shaft 2		1,387 E8	4,087
J <sub>12</sub>	1	Wheel 2	87		4,087
K <sub>12</sub>	1	Gear reduction 3		1 E10	-
J <sub>13</sub>	1	Pinion 3	0,8		1
K <sub>13</sub>	1	Gearbox shaft in		1,58 E7	1
J <sub>14</sub>	1	Clutch flange	19		1
K <sub>14</sub>	1	Clutch		7,88 E7	1
J <sub>15</sub>	1	Flex coupling flange 1	43		1
K <sub>15</sub>	1	Flex. Coupling SM80		2,813 E6	1
J <sub>16</sub>	1	Flex coupling flange 2	14		1
K <sub>16</sub>	1	Rotor shaft		1,49 E7	1
J <sub>17</sub>	1	Rotor	88		1
K <sub>17</sub>	2	Gear reduction 1		1 E10	-
J <sub>18</sub>	2	Pinion 1	67		14,216
K <sub>18</sub>	2	Gear reduction shaft 1		1,824 E9	14,216
J <sub>19</sub>	2	Wheel 1	532		14,216
K <sub>19</sub>	2	Gear reduction 2		1 E10	-
J <sub>20</sub>	2	Pinion 2	7		4,087
K <sub>20</sub>	2	Gear reduction shaft 2		1,387 E8	4,087
J <sub>21</sub>	2	Wheel 2	87		4,087
K <sub>21</sub>	2	Gear reduction 3		1 E10	-
J <sub>22</sub>	2	Pinion 3	0,8		1
K <sub>22</sub>	2	Gearbox shaft in		1,58 E7	1
J <sub>23</sub>	2	Clutch flange	19		1
K <sub>23</sub>	2	Clutch		7,88 E7	1
J <sub>24</sub>	2	Flex coupling flange 1	43		1
K <sub>24</sub>	2	Flex. Coupling SM80		2,813 E6	1
J <sub>25</sub>	2	Flex coupling flange 2	14		1
K <sub>25</sub>	2	Rotor shaft		1,49 E7	1
J <sub>26</sub>	2	Rotor	88		1

Figure E.3: Element inertia part two

# Appendix F

## Simulation results

All simulations that have been performed for this research are summarized in this appendix. For the simulation input a random 30 minute sample is taken from dredging operation of May 2016. A random sample is taken because the data used for simulation is fairly constant, as can be seen at the end of this appendix. A new sample is only chosen if a sample is chosen where no dredging is taking place. For each load input a total of seven simulations is performed. Odd numbered simulations contain diesel engines and even numbered simulations contain dual fuel engines. For the diesel engines, the simulation numbers denote the following:

- x.1 - Original driveline with two main diesel engines
- x.2 - Original driveline with flywheel ESS
- x.3 - Original driveline with supercapacitor ESS
- x.4 - Two main diesel engines replaced by three smaller engines, one switched off

For the dual fuel engines, the simulation numbers denote the following:

- x.1 - Diesel engines replaced by dual fuel engines running on LNG
- x.2 - Dual fuel engines with flywheel ESS
- x.3 - Dual fuel engines with supercapacitor ESS

For every simulation the relevant results are displayed here. The values in the tables denote the following:

- **MDO/LNG cons'd**, this is the amount of fuel consumed during simulation
- **Peak power**, this is the maximum charge and discharge power during simulation
- **SOC**, this is the maximum and minimum state of charge during simulation
- **Within limit**, this is the percentage of load fluctuations within the defined limit
- **Cycles**, this is the number of full charge/discharge cycles for the ESS

## F.1 Simulation 1-2

### F.1.1 Load input

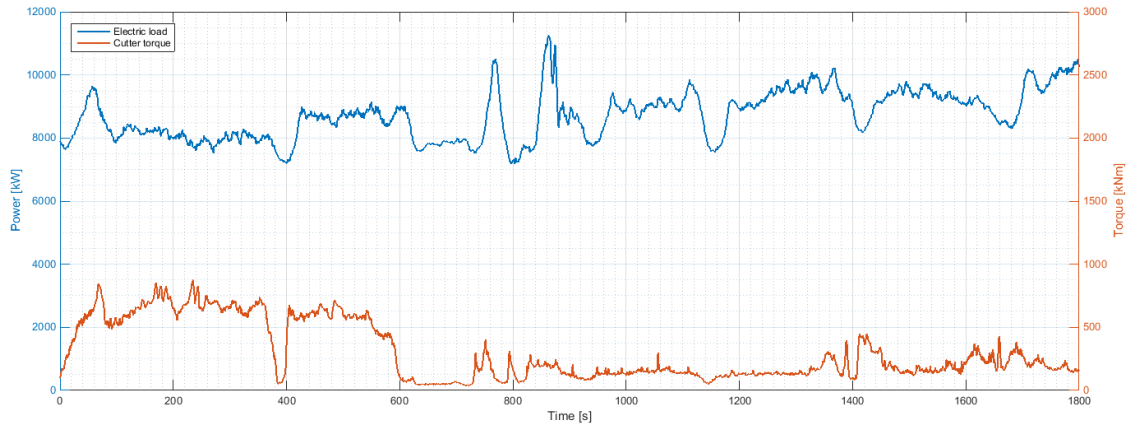


Figure F.1: Input for Simulations 1 and 2 - Data from May 5th 2016, 19:00 - 19:30

### F.1.2 Results

Table F.1: Simulation 1 results

Simulation	MDO cons'd [kg]	Peak power [MW]	SOC [-]	Within limit [%]	Cycles [-]
Sim 1.1	916.29	-	-	86.3	-
Sim 1.2	916.41	-0.819, +0.412	0.823-0.90	>99	<1
Sim 1.3	916.36	-0.815, 0.417	0.788-1.0	>99	1
Sim 1.4	904.96	-	-	79.3	-

Table F.2: Simulation 2 results

Simulation	LNG cons'd [kg]	Peak power [MW]	SOC [-]	Within limit [%]	Cycles [-]
Sim 2.1	861.68	-	-	70.8	-
Sim 2.2	861.74	-1.488, +1.1068	0.798-0.901	99.0	1
Sim 2.3	861.68	-1.479, +1.061	0.645-0.970	>99	2

## F.2 Simulation 3-4

### F.2.1 Load input

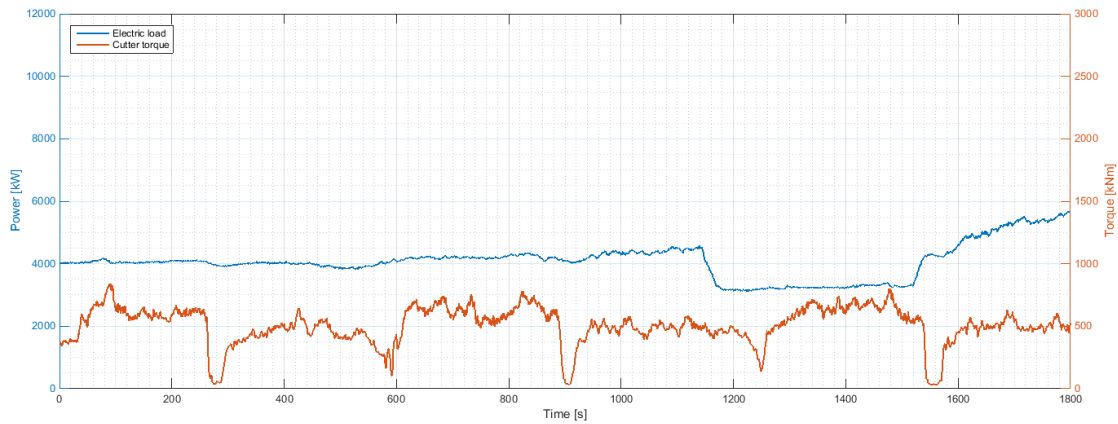


Figure F.2: Input for Simulations 3 and 4 - Data from May 1st 2016, 00:00 - 00:30

### F.2.2 Results

Table F.3: Simulation 3 results

Simulation	MDO cons'd [kg]	Peak power [MW]	SOC [-]	Within limit [%]	Cycles [-]
Sim 3.1	600.60	-	-	95.9	-
Sim 3.2	600.72	-0.545, +0.223	0.823-0.905	>99	<1
Sim 3.3	600.67	-0.546, +0.222	0.90 - 1.0	>99	3
Sim 3.4	578.12	-	-	86.4	-

Table F.4: Simulation 4 results

Simulation	LNG cons'd [kg]	Peak power [MW]	SOC [-]	Within limit [%]	Cycles [-]
Sim 4.1	692.64	-	-	73.9	-
Sim 4.2	693.06	-1.165, +0.593	0.894-0.951	>99	1
Sim 4.3	692.67	-1.165, +0.590	0.90-1.0	97.6	2

## F.3 Simulation 5-6

### F.3.1 Load input

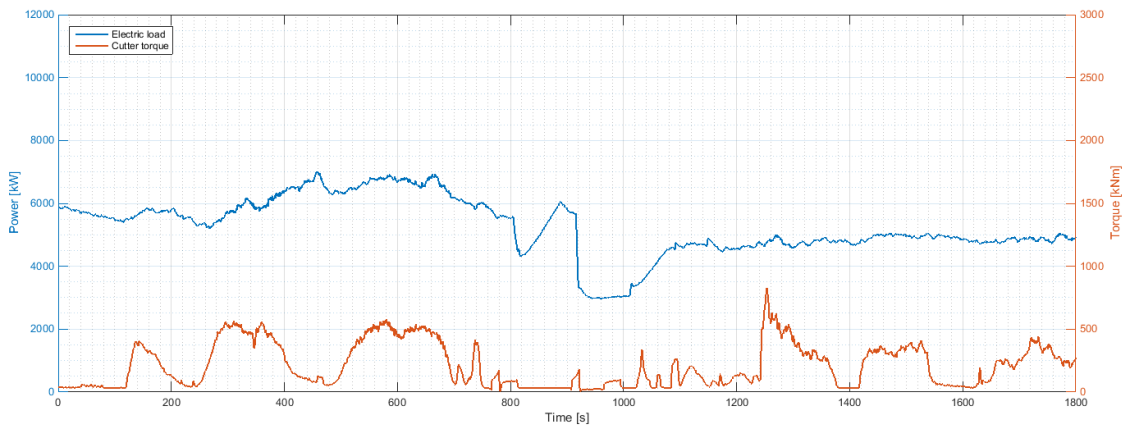


Figure F.3: Input for Simulations 5 and 6 - Data from May 22nd 2016, 22:00 - 22:30

### F.3.2 Results

Table F.5: Simulation 5 results

Simulation	MDO cons'd [kg]	Peak power [MW]	SOC [-]	Within limit [%]	Cycles [-]
Sim 5.1	596.93	-	-	93.8	-
Sim 5.2	597.04	-0.620, + 0.866	0.812-0.90	>99	<1
Sim 5.3	596.94	-0.619, + 0.866	0.801-1.0	>99	3
Sim 5.4	574.45	-	-	90.2	-

Table F.6: Simulation 6 results

Simulation	LNG cons'd [kg]	Peak power [MW]	SOC [-]	Within limit [%]	Cycles [-]
Sim 6.1	689.22	-	-	87.3	-
Sim 6.2	689.29	-1.466, +1.193	0.818-0.962	>99	2
Sim 6.3	688.95	-1.193, +1.217	0.622-1.0	>99	4

## F.4 Simulation 7-8

### F.4.1 Load input

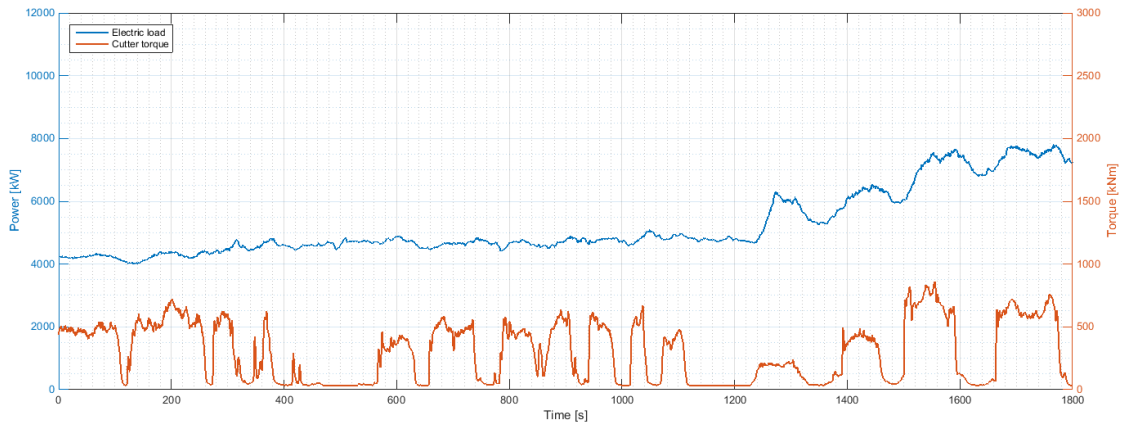


Figure F.4: Input for Simulations 7 and 8 - Data from May 2nd 2016, 06:00 - 06:30

### F.4.2 Results

Table F.7: Simulation 7 results

Simulation	MDO cons'd [kg]	Peak power [MW]	SOC [-]	Within limit [%]	Cycles [-]
Sim 7.1	625.93	-	-	84.7	-
Sim 7.2	624.93	-0.556, +1.714	0.592-0.90	>99	3
Sim 7.3	625.67	-0.557, +1.192	0.25-0.90	95.6	8
Sim 7.4	604.40	-	-	81.2	-

Table F.8: Simulation 8 results

Simulation	LNG cons'd [kg]	Peak power [MW]	SOC [-]	Within limit [%]	Cycles [-]
Sim 8.1	706.29	-	-	73.4	-
Sim 8.2	705.39	-1.280, +2.075	0.427-0.905	>99	6
Sim 8.3	706.05	-1.280, +2.076	0.25-0.925	98.6	14

## F.5 Simulation 9-10

### F.5.1 Load input

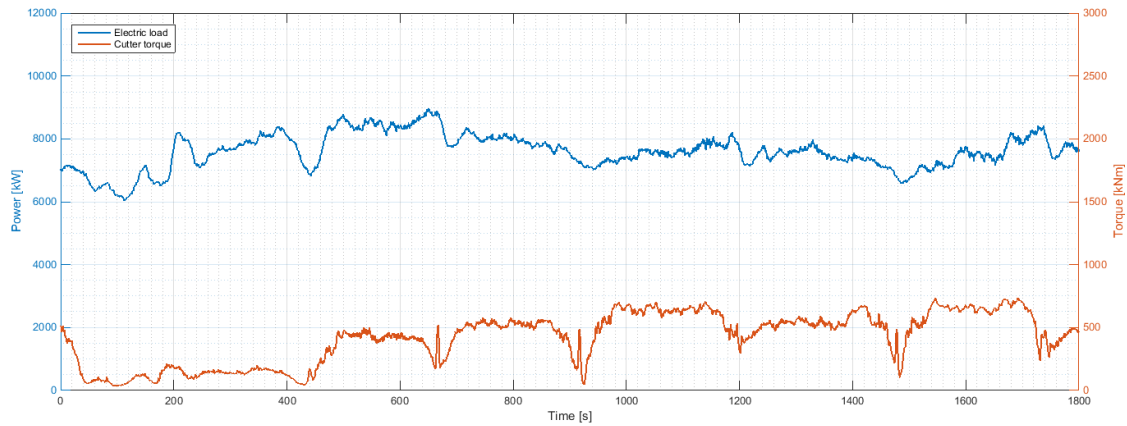


Figure F.5: Input for Simulations 9 and 10 - Data from May 11th 2016, 18:00 - 18:30

### F.5.2 Results

Table F.9: Simulation 9 results

Simulation	MDO cons'd [kg]	Peak power [MW]	SOC [-]	Within limit [%]	Cycles [-]
Sim 9.1	873.67	-	-	94.6	-
Sim 9.2	873.82	-0.594, +0.376	0.824-0.90	>99	<1
Sim 9.3	873.81	-0.591, +0.369	0.837-0.90	98.8	2
Sim 9.4	860.64	-	-	79.56	-

Table F.10: Simulation 10 results

Simulation	LNG cons'd [kg]	Peak power [MW]	SOC [-]	Within limit [%]	Cycles [-]
Sim 10.1	835.69	-	-	69.5	-
Sim 10.2	835.89	-0.840, +0.730	0.847-0.90	>99	<1
Sim 10.3	835.76	-0.827, +0.736	0.819-1.0	98.9	2

## F.6 Data overview

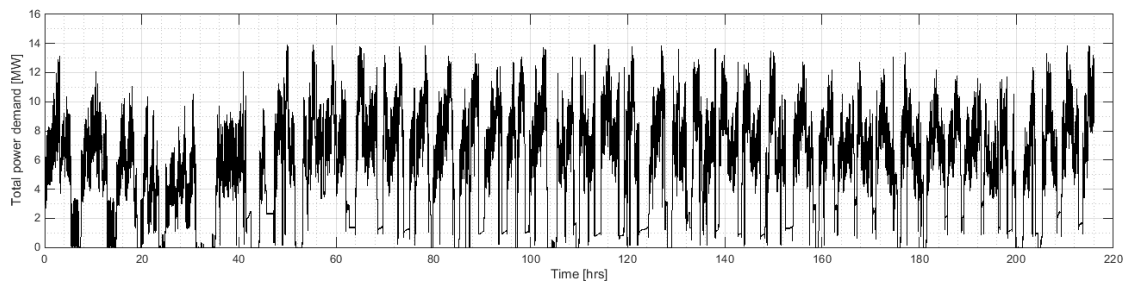


Figure F.6: Data from dredging operation, May 1st - May 9th

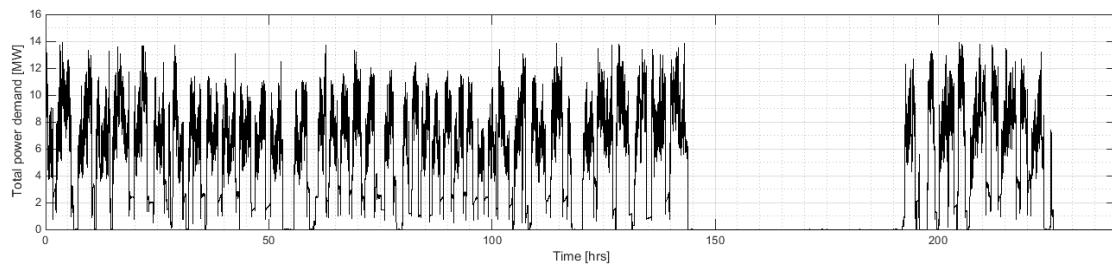


Figure F.7: Data from dredging operation, May 10th - May 19th

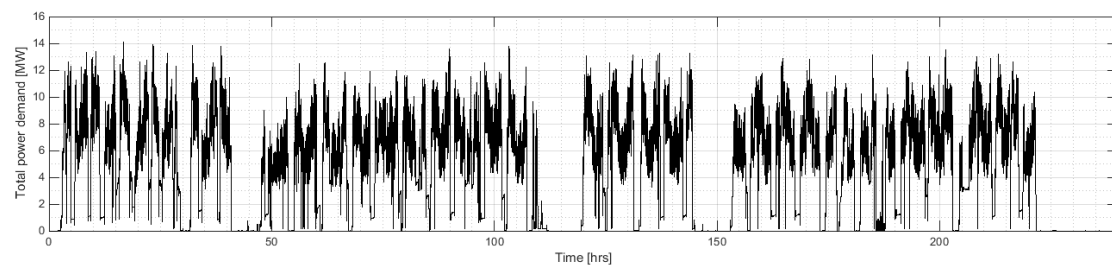


Figure F.8: Data from dredging operation, May 20th - May 30th